Electrostatic Oscillations of Spheroidal Single-Component Plasmas

Mark David Tinkle

Ph.D. Thesis

Department of Physics
University of California, San Diego

1994

UNIVERSITY OF CALIFORNIA, SAN DIEGO

Electrostatic Oscillations of Spheroidal Single-Component Plasmas

A dissertation submitted in partial satisfaction of the requirements for the degree
Doctor of Philosophy in Physics

by

Mark David Tinkle

Committee in Charge:

Clifford M. Surko, Chairman
C. Fred Driscoll
Daniel H. E. Dubin
Thomas M. O'Neil
Barnaby J. Rickett
Charles W. Vanatta

1994

The dissertation of Mark David Tinkle is approved, and it is acceptable in quality and form for publication on microfilm:

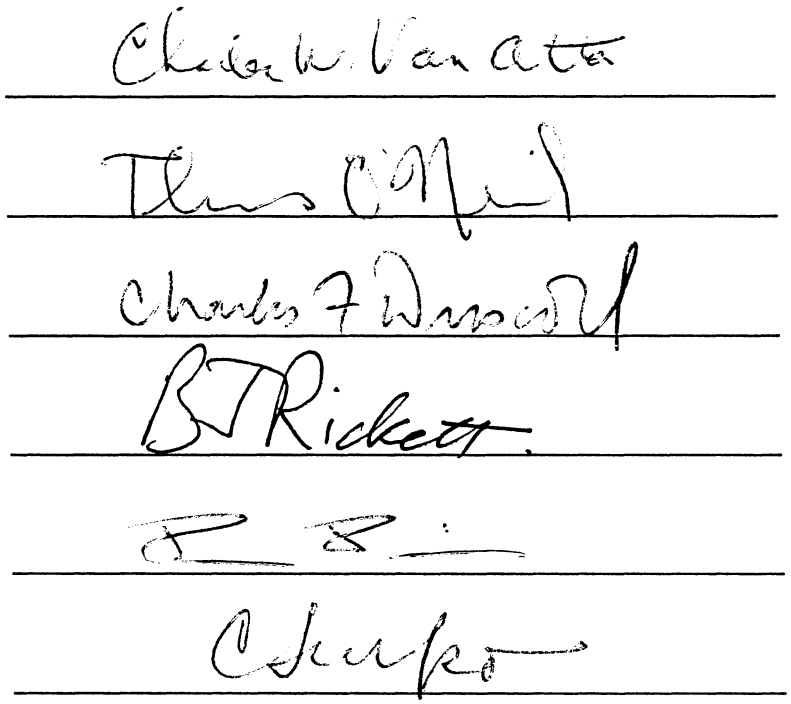

Chairman

University of California, San Diego

1994

This thesis is dedicated to my wife, Lily.

Contents

Symbols and Notation

Cgs units are used throughout the thesis, except for a few practical formulae employing units convenient to the experimentalist. Cylindrical coordinates (ρ, z, ϕ) appear most frequently, with occasional references to Cartesian coordinates (x, y, z), to spherical coordinates (r, θ, ϕ) and to two different sets of spheroidal coordinates, (ξ_1, ξ_2, ϕ) and $(\bar{\xi}_1, \bar{\xi}_2, \phi)$, which are defined in Sec. 2.2. The ϕ coordinate is the same in all four cases.

$A_3(\alpha)$	function used in spheroidal equilibrium, Eq. (2.10)
A_l^m	coefficients in expansion of $\delta\Phi^{\mathrm{o}}_{l,m}$
B_l^m	coefficients in expansion of $\delta\Phi^{\mathrm{i}}_{l,m}$
B_l	coefficients in expansion of image charge potential
B	magnetic field
B_0	magnetic field in center of trap
B_c	magnetic field at charge collectors
B_g	magnetic field at the cathode of the electron gun
c	speed of light
$C(\rho, T)$	normalization of Boltzmann factor used in Poisson solution program
C_l	coefficients in expansion of trap potential
C_4	quartic coeff. in trap potential, a measure of anharmonicity
d	parameter involved in definition of (ξ_1, ξ_2, ϕ) coordinates
$\bar{d}$	parameter involved in definition of $(\bar{\xi}_1, \bar{\xi}_2, \phi)$ coordinates
e	charge of the proton
E	electric field
E_ρ	radial component of electric field

$E_{\|\|}$	particle kinetic energy along the magnetic field
$E_\perp$	particle kinetic energy perpendicular to the magnetic field
E_{I}	minimum energy required to ionize a neutral atom or molecule
E_{II}	minimum energy required for double ionization of a neutral
$g(\alpha)$	function defined in Eq. (4.7)
$G_m(\alpha)$	geometrical factor in theory of azimuthal modes of a spheroid
$G_m(r_p)$	geometrical factor in theory of azimuthal modes of a cylinder
I_{beam}	electron beam current
$k_1(\alpha,\omega)$	argument of P_l^m in general mode dispersion relation
$k_2(\alpha)$	argument of Q_l^m in general mode dispersion relation
k_{B}	Boltzmann constant
k_z	axial wavenumber of a mode
K_m	coefficient of fit to ion mode frequency data for $V < V_t$
l	mode index
L	plasma length, along the axis of the trap
m	particle mass, or azimuthal dependence of mode ($\delta\Phi \sim e^{im\phi}$)
n	number density of plasma particles
n_{B}	density at the Brillouin limit
n_n	number density of neutral gas atoms or molecules
N	total number of plasma particles
N_{ion}	total number of ions in the trap
$N_{\mathrm{Ar+}}$	total number of Ar^+ ions in the trap
p	neutral gas pressure
P_l	Legendre functions of the first kind
P_l^m	associated Legendre functions of the first kind
$P_l^{m\,\prime}$	derivative of P_l^m with respect to its argument

Q_l^m	associated Legendre functions of the second kind (see App. A)
$Q_l^{m\,\prime}$	derivative of Q_l^m with respect to its argument
q	charge of a plasma particle
$q_z(\rho)$	z-integrated particle density
q_0	$q_z(\rho = 0)$
Q	total plasma charge
r	spherical radius coordinate
r_{beam}	radius of electron beam
r_g	radius of cathode of electron gun
r_p	maximum extent of the plasma in ρ
$\hat{r}_p$	estimate of r_p
r_w	radius of cylindrical electrode wall
R	magnetic mirror ratio at charge collectors
t	time
T	plasma temperature
V	confinement voltage, applied with opposite sign to ring and endcaps
V_0	potential in center of trap, nominally zero
V_c	critical potential above which single particles are not confined
V_{min}	minimum V to achieve $n = n_{\mathrm{B}}$ for ion plasma
V_t	value of V for which plasma has $\alpha = 1/\sqrt{2}$
z	coordinate along the direction of the magnetic field
z_0	trap scale coordinate, nominally the distance from center to endcap
z_{cm}	axial position of the plasma center of mass
α	plasma aspect ratio, $L/2r_p$
γ	ratio of specific heats ($\gamma = 3$ for 1D expansions)
ϵ	dielectric tensor for a single-component plasma

$\epsilon_1, \epsilon_2, \epsilon_3$	elements of ϵ
θ	polar angle of spherical coordinates
λ	wavelength of a mode
λ_{D}	plasma Debye length
$\lambda_{\mathrm{threshold}}$	minimum λ_{D} for undamped C. M. motion in cylindrical trap
ξ_1, ξ_2	spheroidal coordinates outside the plasma
$\bar{\xi}_1, \bar{\xi}_2$	frequency-dependent spheroidal coordinates used inside the plasma
ρ	cylindrical radius coordinate
ρ_0	minimum radius of ring electrode, $\rho_0 = \sqrt{2} z_0$
ρ_c	radius of cyclotron orbit
ρ_d	radius of magnetron drift orbit
σ_i	ionization cross-section
σ_{max}	maximum value of σ_i
τ_a	exponential loss time of positrons due to annihilation
τ_c	time-constant for cooling of electron or positron plasmas
ϕ	azimuthal angle coordinate
Φ	electrostatic potential
Φ_{I}	potential produced by plasma image charge
Φ_{m}	potential produced by plasma monopole moment (Q)
$\delta\Phi$	perturbation in Φ caused by plasma mode
$\delta\Phi^{\mathrm{i}}$	perturbation inside the plasma
$\delta\Phi^{\mathrm{o}}$	perturbation outside the plasma
$\delta\Phi^{\mathrm{i}}_{l,m}$	(l,m) component of $\delta\Phi^{\mathrm{i}}$
$\delta\Phi^{\mathrm{o}}_{l,m}$	(l,m) component of $\delta\Phi^{\mathrm{o}}$
ω	angular frequency
ω_2	quadrupole mode frequency

ω_2^c	quadrupole mode frequency predicted by cold fluid theory
ω_{CM}	frequency of axial oscillation of plasma center of mass
ω_m	frequency of purely azimuthal mode with mode number m
ω_p	plasma frequency
ω_r	plasma rotation frequency
ω_z	harmonic axial frequency of quadrupole trap
ω_z^*	value of ω_z altered by image charge effects
Ω_c	cyclotron frequency, qB/mc
Ω_c'	cyclotron frequency down-shifted by quadrupole electric field
Ω_M	magnetron frequency
Ω_v	vortex frequency, $\Omega_c - 2\omega_r$

List of Figures

Acknowledgments

The work described in this thesis was directed by Professor Cliff Surko, who has managed to graft useful practical lab skills and some physical intuition onto a closet theorist. The process was at first painful, and he showed remarkable patience with my early resistance to it. As Cliff has remarked, he is interested in the basic physics, whereas I am always trying to figure out why data and theory disagree in the third decimal place. I think the contrast has been beneficial; I learned not to short-change the dominant phenomena of an experiment, and we eventually produced some plasma data lying right on a theory curve.

Rod Greaves has been a close collaborator on the majority of this work. Without his contributions, I would have taken a longer time and produced a much poorer thesis. From Rod, I have gained a wider view of the world of experimental plasma research, some experimental judgement, and a lot of practical knowledge of laboratory hardware. Rod and Cliff together have taught me how to write a physics paper and showed me that scathing referee reports need not be the death of a manuscript. I have always enjoyed Rod's refreshing perspectives on the relative merits of tokamak experiments vs. basic plasma physics and of experiment vs. theory in general.

One of the great assets of Dr. Surko's research group is our senior technician, Gene Jerzewski, whose nearly universal knowledge of laboratory equipment keeps the lab running. Always willing to interrupt his own work to help a confused student, Gene has been a great help to me and a good friend.

I am very grateful to the members of the UCSD electron plasma group led by Fred Driscoll and Tom O'Neil for adopting me. At their often contentious group

meetings, I was exposed to the current state of the art of single-component plasma theory and experiment. I also learned a bit about crowd control and viewgraph preparation, after getting through only one of twenty slides of an informal talk. I have enjoyed conversations, technical and otherwise, with almost everyone in the group. I particularly want to thank Kevin Fine for various straightforward explanations of confusing physics, for occasional technical advice, and for raising the level of craftsmanship of my construction projects by the example of his own exquisite plasma machines. Tom O'Neil has generously contributed to my education through many beautifully clear and calm discussions of plasma theory, extending back to the first-year mechanics class that subtly warped my path toward plasma physics. Most of all, I am grateful to Dan Dubin, for deriving the theory of the modes of a spheroidal single-component plasma, and then spending large blocks of time helping me to understand it. In addition, Dan helped me estimate the importance of the effects of image charge and anharmonicity on the electron plasma modes, provided an approximate theory of their temperature dependence, and served as a sounding-board and theory advisor for various ideas about plasmas.

Early collaborators in this work include Tom Murphy, who helped me learn my way around a plasma lab, and Tom Bernat, a visiting physicist who taught me about low-noise measurements during the dark days when remote sensing of positrons in the trap seemed like a forlorn dream. More recently, Ross Spencer and Grant Mason of Brigham Young University performed numerical simulations of some of our electron plasmas, resulting in remarkably good agreement with the mode frequency data. In the process, they uncovered an error in our temperature measurement and reaffirmed my faith in plasma theory.

At a more fundamental level, I am indebted to my parents, Stan and Barbara, talented educators who gave me an early love of math and a skeptical attitude, along

with a variety of interests of less direct use to a scientist (such as a tendency toward playful abuse of the English language, which I have tried to suppress while writing this thesis).

My wife, Lily, has been a constant source of emotional support. For years, she has cheerfully listened to many confused explanations of research in progress, and she also helped a great deal with the production of figures for the thesis.

Financial support for the work reported here was provided by the Office of Naval Research.

Vita

March 20, 1962	Born, Anaheim, California
1984	B.S., Physics, California Institute of Technology
1984-1987	Member of Technical Staff, Rockwell International
1987	M.S., Engineering, California State University, Fullerton
1989	M.S., Physics, University of California, San Diego
1994	Ph.D., Physics, University of California, San Diego

Publications

S. Tang, M. D. Tinkle, R. G. Greaves, and C. M. Surko, "Annihilation gamma-ray spectra from positron-molecule interactions", *Physical Review Letters* **68**, 3793 (1992).

M. D. Tinkle, R. G. Greaves, C. M. Surko, R. Spencer, and G. W. Mason, "Low-order modes as diagnostics of spheroidal nonneutral plasmas", *Physical Review Letters* **72**, 352 (1994).

R. G. Greaves, M. D. Tinkle, and C. M. Surko, "Creation and uses of positron plasmas", *Physics of Plasmas* **1**, 1439 (1994).

K. Iwata, R. G. Greaves, T. J. Murphy, M. D. Tinkle, and C. M. Surko, "Measurements of positron annihilation rates on molecules", submitted to *Physical Review A*.

R. G. Greaves, M. D. Tinkle, and C. M. Surko, "Modes of a pure ion plasma at the Brillouin limit", submitted to *Physical Review Letters*.

Fields of Study

Major Field: Physics

Studies in Plasma Physics.
Professor Clifford M. Surko

ABSTRACT OF THE DISSERTATION

Electrostatic Oscillations of Spheroidal Single-Component Plasmas

by

Mark David Tinkle

Doctor of Philosophy in Physics

University of California, San Diego, 1994

Professor Clifford M. Surko, Chair

A quadrupole Penning trap designed to accumulate positron plasmas has been used to study the global plasma modes of electron plasmas, positron plasmas, and ion plasmas. The continuously generated ion plasmas reach the Brillouin density limit and are thus effectively unmagnetized, whereas the electron and positron plasmas are highly magnetized and well confined. The spheroidal equilibrium expected in a quadrupole trap applies to both cases, permitting the use of a new cold fluid theory of the normal modes of the plasmas. The two classes of modes studied experimentally, axial modes of electron plasmas and azimuthal modes of ion plasmas, have frequencies in good agreement with the theory. Anomalous damping of the axial center-of-mass oscillation is observed in a cylindrical trap, but not in the

quadrupole trap. For the axial quadrupole mode of electron plasmas, the plasma temperature causes an increase in the frequency which is accurately reproduced by numerical plasma simulations, and which appears to be adequately described by recent work on a warm fluid theory. The use of the electron plasma modes to monitor the size, shape, and temperature of the plasmas is described. This technique is expected to be an important nondestructive tool for the study of positron plasmas.

Chapter 1

Introduction

Since the discovery by Penning [1936] that a magnetic field could enhance the current of an electrical discharge in a low-pressure gas, a wide variety of related devices has been developed and studied. A minor modification of the electrode geometry used by Penning yields a device, called a Penning trap, capable of storing charged particles in a high vacuum for long periods. In most Penning traps, a uniform magnetic field is aligned with the axis of a set of cylindrically symmetric electrodes, which supply an electric potential to prevent particles from streaming out of the trap along the magnetic field lines. Motions perpendicular to the magnetic field are restricted to circular orbits at the cyclotron frequency.

The early development of the Penning trap concentrated on the confinement of small numbers of charged particles to be used for precision measurements. For this purpose, electrodes were designed to produce precise electric quadrupole potentials, in which single particles execute simple harmonic oscillations at frequencies dependent on their charge and mass. The technology of precision quadrupole traps [*Brown and Gabrielse*, 1986] eventually advanced to the point that measurements made with these techniques of the charge-to-mass ratios of electrons, positrons [*Dehmelt*, 1990], protons, and antiprotons [*Gabrielse et al.*, 1990] are among the most precise phys-

ical measurements ever made. Single particles have been confined for months, and their motions observed by the tiny signals produced on the confining electrodes. Atomic physicists have used quadrupole Penning traps to measure the masses and energy levels of various ions. Ion mass resolutions of 1 part in 10^6 are achieved by commercial mass spectrometers using similar techniques [*Wilkins et al.*, 1989], and atomic spectroscopy in an isolated trap environment is of potential use for the next generation of atomic clocks [*Bollinger et al.*, 1985]. In all of these applications, the number of trapped particles is kept low to avoid particle interactions.

In 1975, Penning traps began to be used to study pure electron plasmas [*Malmberg and de Grassie*, 1975]. It had been understood previously that electron beams have some of the properties of neutral plasmas, including Debye shielding and plasma oscillations. In contrast to neutral plasmas, however, it was realized [*Malmberg and O'Neil*, 1977; *O'Neil and Driscoll*, 1979] that a confined single-component plasma could be in thermal equilibrium, and that the confinement should be very good [*O'Neil*, 1980]. The presence of only a single charge species eliminates some of the waves and instabilities present in neutral plasmas (e.g., whistler waves and ion-acoustic waves), but makes only minor alterations in others. As a result of this and of the quiescent equilibrium states achievable with pure electron plasmas, Landau damping of plasma waves has been most convincingly demonstrated in pure electron plasmas [*Malmberg and de Grassie*, 1975].

The pure electron plasmas studied have typically been long cylinders, to increase the total number of trapped particles and to reduce the importance of end effects, which are difficult to treat theoretically. Experimental techniques have been refined to the point that electron columns are routinely created, cut into pieces axially, moved off axis, and allowed to interact with other columns [*Driscoll and Fine*, 1990; *Fine et al.*, 1991; *Mitchell et al.*, 1993]. Images of the plasma density,

obtained either from multiple shots or more recently from a single shot, using a phosphor screen and CCD camera [*Fine et al.*, 1993; *Peurrung and Fajans*, 1993], show quiescent plasmas with nearly uniform density. If the plasma is made unstable [*Fine et al.*, 1993; *Huang and Driscoll*, 1994] or allowed to interact with another column [*Mitchell et al.*, 1993], spiral filaments form and lead to turbulence. Unlike neutral plasmas, which must be kept hot to avoid recombination, single-component plasmas can be cooled to cryogenic temperatures. Measurements of the rate of equilibration between the temperatures parallel to and perpendicular to the magnetic field over several orders of magnitude in temperature [*Beck et al.*, 1992] and their excellent agreement with theoretical calculations [*Glinsky and O'Neil*, 1991] show some of the interesting physics that may be explored as a result.

Experiments at the National Institute of Standards and Technology (NIST) with pure ion plasmas in precision quadrupole traps have begun to combine the two different fields of Penning trap research. Though the number of particles trapped in these experiments is still small ($\simeq 10^5$), laser cooling lowers their temperature sufficiently to make them plasmas. In some experiments [*Bollinger et al.*, 1994], the temperature is so low ($T < 10$ mK) that the plasmas become strongly coupled, forming concentric shells. Because a quadrupole trap is used, the plasmas are spheroidal [*Turner*, 1987], rather than cylindrical. Remarkably, an exact theory exists [*Dubin*, 1991] of the normal modes of these plasmas, in the limit of very low temperatures. Some of the predicted modes have been observed [*Heinzen et al.*, 1991; *Bollinger et al.*, 1993] at frequencies in very good agreement with the theory.

The experiments described in this thesis were performed with large numbers of particles (10^7 to 10^9) in an approximately quadrupole trap. Single-component plasmas of various charge species have been studied in the same trap, including pure electron, pure ion, and pure positron plasmas. Although the ion plasmas are

qualitatively quite different from the electron and positron plasmas, and a different set of normal modes is studied, the same theory [*Dubin*, 1991] has been successfully applied to both.

The trap was designed to accumulate and store positrons [*Wysocki et al.*, 1988; *Surko et al.*, 1989; *Surko and Murphy*, 1990], with the goal of forming and studying electron-positron plasmas, an effort which is just now beginning [*Greaves et al.*, 1994]. Another motivation was the proposed use of trapped positrons as "tagged electrons" for tokamak transport studies [*Surko et al.*, 1986; *Murphy*, 1987]. Other applications for trapped positrons include the production of high-emittance positron beams for high-energy physics experiments and the efforts currently under way to form antihydrogen [*Gabrielse et al.*, 1988]. An early discovery made with this trap [*Surko et al.*, 1988] was that the cross-sections for annihilation of room-temperature positrons with some molecules are very high, implying the existence of previously unsuspected positron-molecule bound states. This phenomenon may be of importance to astrophysics [*Surko et al.*, 1993] and mass spectrometry [*Passner et al.*, 1989; *Glish et al.*, 1994] as well as to molecular physics, and its study [*Murphy and Surko*, 1991; *Tang et al.*, 1992; *Iwata et al.*, 1993; *Iwata et al.*, 1994] has made an interesting addition to the plasma physics work done with the trap.

The plasma mode studies reported here were begun with the intention of developing a nonperturbative diagnostic of the properties of a positron plasma, for which neither the probes used for neutral plasmas nor the destructive diagnostics used for electron plasmas are desirable. The same techniques could also be used to monitor antiproton plasmas [*Gabrielse et al.*, 1986; *Holzscheiter*, 1993] or as an adjunct to the usual techniques for electron plasma experiments. The properties of positron plasmas are the same as those of electron plasmas, except for their confinement, which is dominated by annihilation on neutral gas molecules in our

trap. Because electrons are more convenient to work with, positrons have not been used for most of these mode studies.

The electron plasmas (and the positron plasmas) are formed by trapping particles from a weak beam, using collisions with neutral gas molecules to remove the required energy. As a result, the plasmas cool to room temperature, but they may be heated to about 0.5 eV by the application of rf noise. The temperature and the radial density profile can be measured using standard techniques [*Hsu and Hirshfield*, 1976; *de Grassie and Malmberg*, 1977]. The electron plasmas have confinement times on the order of 10^4 s, and may eventually be lost by attachment to neutrals, rather than by radial transport. Several of the normal modes predicted by Dubin [1991] are observed, though not always at exactly the frequencies predicted by the cold fluid theory. The discrepancies are mostly the result of the plasma temperature, and the data are in excellent agreement with numerical simulations of the plasmas [*Tinkle et al.*, 1994].

To study ion plasmas in the same trap, an electron beam is passed along the trap axis in the presence of a low-pressure gas. Ions created inside the potential well of the trap by ionization are confined for times on the order of 1 s. For the experiments described in this thesis, the beam is left on continuously, producing large steady-state plasmas at densities near the Brillouin density limit. The standard diagnostic techniques are difficult to apply to these poorly magnetized plasmas, but observations of image charges, steady-state ion currents to the electrodes, and azimuthal plasma modes are all consistent with a simple model of the steady state. The plasmas are approximately spheroidal, with shapes determined by the strength of the quadrupole trap potential, and in some cases appear to be surrounded by a low-density "halo" plasma. The frequencies of the azimuthal modes agree very well with the cold fluid theory and the steady state model, except when a halo is

believed to be present.

This thesis is organized in the following manner. Chapter 2 describes the theory of single-component plasmas in quadrupole traps. The experimental equipment and techniques used are explained in Ch. 3, except for details specific to the ion experiments. The results obtained with electron plasmas are presented in Ch. 4 and compared with the cold fluid theory and with numerical simulations. The use of these results as diagnostics is also described, and data obtained with positron plasmas is shown. The experiments with ion plasmas are described in Ch. 5. Chapter 6, which concludes the thesis, is a brief summary of the present state of knowledge in this area.

Chapter 2

Theory of Spheroidal Nonneutral Plasmas

This chapter describes the theory of the equilibrium and normal modes of a plasma in a quadrupole Penning trap, beginning with a discussion of the motions of individual particles.

2.1 Equilibrium

The electrodes of an ideal quadrupole Penning trap, shown in Fig. 2.1, are hyperboloids of revolution with their axis of symmetry (defined as the z axis) aligned with a uniform magnetic field, B, and sharing the asymptotes $\rho = \pm\sqrt{2}z$, where $\rho = \sqrt{x^2 + y^2}$ is the cylindrical radius coordinate. Various choices for the hyperboloids are possible. The standard one is the asymptotically symmetric Penning trap, in which the electrode surfaces satisfy the equation

$$z^2 - \frac{1}{2}\rho^2 = \pm z_0^2. \tag{2.1}$$

The minimum distance from the trap center to either of the two "endcap" electrodes (described by the plus sign in the above equation) is thus z_0, and the distance to the "ring" electrode (described by the minus sign) is $\rho_0 = \sqrt{2}z_0$. If the endcaps and

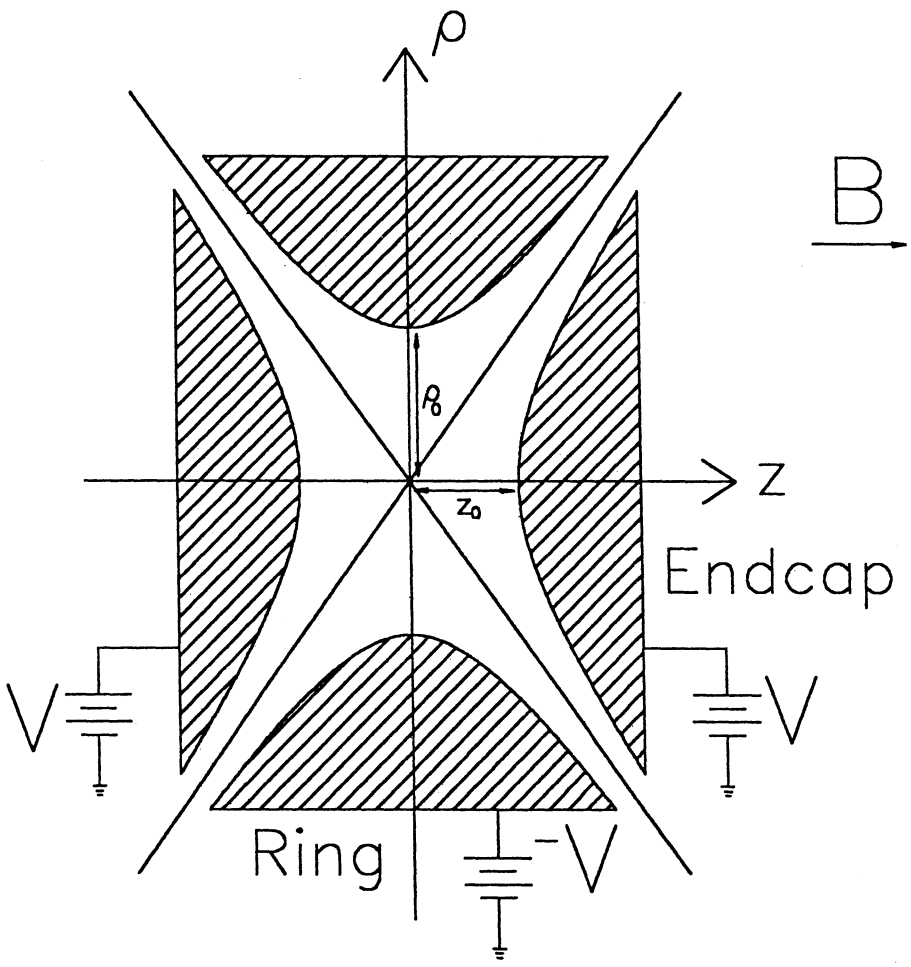

Figure 2.1: Cross-section of an ideal quadrupole Penning trap, truncated for convenience.

the ring are set to potentials V and $-V$, respectively, the electric potential has the form

$$\Phi(\rho, z) = V(z^2 - \frac{1}{2}\rho^2)/z_0^2. \tag{2.2}$$

The choice of ρ_0/z_0 affects the precise anharmonicity tuning required for accurate particle mass measurements (see Sec. 2.5), but is not very important otherwise.

In the absence of the electric field of the trap, a charged particle would move freely in the z direction, while executing circular motions in x and y at the cyclotron frequency, $\Omega_c = qB/mc$, where c is the speed of light, and q and m are the charge and mass of the particle, respectively. A charged particle confined in the trap electric field follows a more complicated path that is the superposition of three independent harmonic oscillations. In the z direction, it oscillates about the origin at a frequency $\omega_z = \sqrt{2qV/mz_0^2}$. Its motion in the x and y coordinates consists of a rapid circular cyclotron motion at a frequency

$$\Omega_c' = \frac{\Omega_c}{2} + \frac{1}{2}\sqrt{\Omega_c^2 - 2\omega_z^2}, \tag{2.3}$$

accompanied by a slower circular drift around the z axis at the magnetron frequency,

$$\Omega_M = \frac{\Omega_c}{2} - \frac{1}{2}\sqrt{\Omega_c^2 - 2\omega_z^2}. \tag{2.4}$$

These two frequencies are the roots of the equation

$$\omega_z^2 = 2\omega(\Omega_c - \omega). \tag{2.5}$$

When $\Omega_c' \gg \Omega_M$ and the electric field varies slowly over the radius of the cyclotron orbits, conditions that are well satisfied in most electron plasma experiments, the magnetron motion may be thought of as the $E \times B$ drift of the guiding center of the particle. The amplitudes and phases of the three independent oscillations may be determined from the initial conditions. Typically, the amplitudes are of more

interest than the phases, since they are constants of the motion. In particular, the radius of the cyclotron motion is

$$\rho_c = \left[\frac{\dot{\rho}^2 + \rho^2(\dot{\phi} + \Omega_M)^2}{\Omega_c^2 - 2\omega_z^2} \right]^{1/2}, \tag{2.6}$$

where ρ is the radial position and $\dot{\rho}$ and $\rho\dot{\phi}$ are the radial and azimuthal components of the particle velocity. The radius, ρ_d, of the magnetron drift motion is found from the same formula by replacing Ω_M with Ω_c'.

The confined particle orbits described above are only possible when $\omega_z^2 < \Omega_c^2/2$; for higher values of ω_z, the particle trajectories in x and y are combinations of hyperbolic sine and cosine functions, and the particle will strike the ring electrode quickly. As a result, V must be kept below a critical value,

$$V_c = B^2 z_0^2 q/4mc^2, \tag{2.7}$$

for the trap to work. Conversely, for a particular choice of V and B, only particles with $m/q < B^2 z_0^2/Vc^2$ will be confined.

The thermal equilibrium of a large number of particles confined in a cylindrical Penning trap at a low temperature is a uniform-density cylindrical plasma, rotating rigidly [*O'Neil and Driscoll*, 1979]. The rotation frequency, ω_r, may be either of the two roots of the equation

$$\omega_p^2 = 2\omega_r(\Omega_c - \omega_r), \tag{2.8}$$

where $\omega_p = (4\pi q^2 n/m)^{1/2}$ is the plasma frequency, and n is the number density of the plasma. Surprisingly, this equation also applies to the low-temperature equilibria of plasmas in quadrupole traps, which are uniform-density, rigidly rotating spheroids [*Turner*, 1987]. The spheroids are biaxial ellipsoids with rotational symmetry about the z axis, so they are completely specified by their length, L, along the z axis and

their radius, r_p, at $z = 0$. The ratio of length to diameter,

$$\alpha = L/2r_p, \tag{2.9}$$

is referred to as the aspect ratio. In equilibrium, α is related to the plasma density by the equation [*Dubin*, 1993]

$$\omega_p^2 = \omega_z^2 \frac{2}{A_3(\alpha)}, \tag{2.10}$$

where

$$A_3(\alpha) = \frac{2Q_1^0\left[\alpha(\alpha^2-1)^{-1/2}\right]}{\alpha^2-1}, \tag{2.11}$$

and Q_1^0 is a Legendre function of the second kind (see App. A). As shown in Fig. 2.2, ω_p is a monotonically increasing function of α which approaches its minimum value, $\omega_p = \omega_z$, as $\alpha \to 0$. This implies that $\omega_r \geq \Omega_{\mathrm{M}}$, as may be seen from a comparison of Eq. (2.5) and Eq. (2.8).

As in the cylindrical plasma equilibrium, the radial electric field inside the plasma is proportional to ρ, having the form $E_\rho = m\omega_p^2\rho/2qz_0^2$. Comparing this with the radial electric field of the trap, $E_\rho = m\omega_z^2\rho/2qz_0^2$, which led to the condition $\omega_z^2 < \Omega_c^2/2$, it is clear that a similar condition applies to the plasma frequency. Just as the trap field prevents confinement for $V \geq V_c$, plasma self-fields limit the density of trapped particles to the Brillouin density [*Brillouin*, 1945],

$$n_{\mathrm{B}} = \frac{B^2}{8\pi mc^2}, \tag{2.12}$$

at which $\omega_p^2 = \Omega_c^2/2$. At this limiting density, the plasma rotation frequency is $\omega_r = \Omega_c/2$, and the plasma has the highest aspect ratio available for the specified values of ω_z and Ω_c.

In a plasma, particles move at nearly constant velocities in the z direction and reflect from the plasma boundary, rather than undergoing simple harmonic

oscillation. There is a distribution of axial bounce periods determined from the plasma temperature, as in cylindrical plasmas, and from the particle radius. The motions in x and y are similar to those described above for single trapped particles, with the simple change $\omega_z \rightarrow \omega_p$ in Eq. (2.3), Eq. (2.4), and Eq. (2.6), except that motions in the plasma boundary are more complicated. As the Brillouin limit is approached ($\omega_p \rightarrow \Omega_c/\sqrt{2}$), the orbit size of the plasma particles diverges, just as the orbit size of single trapped particles diverges when the confinement limit is approached ($\omega_z \rightarrow \Omega_c/\sqrt{2}$). In this case, however, particles may remain confined in the trap as long as the plasma boundary is well separated from the electrode surfaces, because their orbit radius becomes finite once they leave the plasma. In the limit of high magnetic field or low temperature, the particle motions in a plasma at the Brillouin density limit are straight-line trajectories followed by specular reflections from the plasma boundary, when viewed in a frame rotating with the plasma.

2.2 Plasma Oscillations

The dispersion relation for the normal modes of these nonneutral plasma spheroids has been derived in the cold fluid limit by D. H. E. Dubin [1991], using spheroidal coordinates and a clever frequency-dependent coordinate transformation to match solutions for the potential perturbation, $\delta\Phi$, at the plasma surface. This is the first analytical theory to treat the boundary conditions of a finite plasma exactly.

To understand the structure of the normal modes described by the theory requires some discussion of the coordinate systems used. Outside the plasma, spheroidal coordinates (ξ_1, ξ_2, ϕ) are used. The azimuthal angle, ϕ, is the same as in cylindrical coordinates, and ξ_1 and ξ_2 are related to cylindrical coordinates by the

equations

$$\rho = [(\xi_1^2 - d^2)(1 - \xi_2^2)]^{1/2}, \tag{2.13}$$

$$z = \xi_1 \xi_2. \tag{2.14}$$

With the parameter d chosen as $d^2 = (L/2)^2 - r_p^2$, the plasma surface is described by $\xi_1 = L/2$. The solutions to Laplace's equation can be expanded in terms of the associated Legendre functions as

$$\delta\Phi^o(\xi_1, \xi_2, \phi, t) = \sum_{l=1}^{\infty} \sum_{m=-l}^{l} \delta\Phi^o_{l,m}(\xi_1, \xi_2, \phi, t), \tag{2.15}$$

$$\delta\Phi^o_{l,m}(\xi_1, \xi_2, \phi, t) = A_{l,m} Q_l^m(\xi_1/d) P_l^m(\xi_2) e^{i(m\phi - \omega t)}, \tag{2.16}$$

where the $A_{l,m}$ are constant coefficients.

Inside the plasma, a different set of spheroidal coordinates, $(\bar{\xi}_1, \bar{\xi}_2, \phi)$, is used in which the relation to the z coordinate is altered:

$$\rho = [(\bar{\xi}_1^2 - \bar{d}^2)(1 - \bar{\xi}_2^2)]^{1/2}, \tag{2.17}$$

$$z = (\epsilon_3/\epsilon_1)^{1/2} \bar{\xi}_1 \bar{\xi}_2, \tag{2.18}$$

where

$$\bar{d}^2 = \left(\frac{L}{2}\right)^2 \frac{\epsilon_1}{\epsilon_3} - r_p^2. \tag{2.19}$$

The quantities ϵ_1 and ϵ_3 are elements of the dielectric tensor appropriate to a single-component plasma in a uniform magnetic field,

$$\boldsymbol{\epsilon} = \begin{bmatrix} \epsilon_1 & -i\epsilon_2 & 0 \\ i\epsilon_2 & \epsilon_1 & 0 \\ 0 & 0 & \epsilon_3 \end{bmatrix}, \tag{2.20}$$

and are related to the plasma parameters as follows:

$$\epsilon_1 = 1 - \omega_p^2/(\omega^2 - \Omega_v^2), \tag{2.21}$$

$$\epsilon_2 = \Omega_v \omega_p^2 / \omega(\omega^2 - \Omega_v^2), \tag{2.22}$$

$$\epsilon_3 = 1 - \omega_p^2/\omega^2, \tag{2.23}$$

where $\Omega_v = \Omega_c - 2\omega_r$. In this coordinate system, the surface of the plasma is described by $\bar{\xi}_1 = (\epsilon_1/\epsilon_3)^{1/2} L/2$, and Poisson's equation is transformed into Laplace's equation. As a result, the perturbed potential inside the plasma may be written as

$$\delta\Phi^{\mathrm{i}}(\bar{\xi}_1, \bar{\xi}_2, \phi, t) = \sum_{l=1}^{\infty} \sum_{m=-l}^{l} \delta\Phi^{\mathrm{i}}_{l,m}(\bar{\xi}_1, \bar{\xi}_2, \phi, t), \tag{2.24}$$

$$\delta\Phi^{\mathrm{i}}_{l,m}(\bar{\xi}_1, \bar{\xi}_2, \phi, t) = B_{l,m} P_l^m(\bar{\xi}_1/\bar{d}) P_l^m(\bar{\xi}_2) e^{i(m\phi - \omega t)}. \tag{2.25}$$

Matching $\delta\Phi^{\mathrm{i}}_{l,m}$ and $\delta\Phi^{\mathrm{o}}_{l,m}$ at the surface leads to the dispersion relation

$$\epsilon_3 + m\alpha \left(\alpha^2 - \frac{\epsilon_3}{\epsilon_1}\right)^{1/2} \frac{P_l^m(k_1)}{P_l^{m\,\prime}(k_1)} = \left(\frac{\alpha^2 - \epsilon_3/\epsilon_1}{\alpha^2 - 1}\right)^{1/2} \frac{P_l^m(k_1) Q_l^{m\,\prime}(k_2)}{P_l^{m\,\prime}(k_1) Q_l^m(k_2)}, \tag{2.26}$$

where $k_1 = \alpha/(\alpha^2 - \epsilon_3/\epsilon_1)^{1/2}$, $k_2 = \alpha(\alpha^2 - 1)^{-1/2}$, and the primes indicate derivatives taken with respect to the entire argument.

For strongly magnetized plasmas, in which $\Omega_c \gg \omega_p$ and $\Omega_c \gg \omega_z$, the dispersion relation for low-frequency eigenmodes with azimuthal symmetry (i.e., $m = 0$) reduces to

$$1 - \frac{\omega_p^2}{\omega^2} = \left(\frac{\alpha^2 - 1 + \omega_p^2/\omega^2}{\alpha^2 - 1}\right)^{1/2} \frac{P_l(k_1) Q_l^{0\,\prime}(k_2)}{P_l'(k_1) Q_l^0(k_2)}, \tag{2.27}$$

and k_1 simplifies to $k_1 = \alpha(\alpha^2 - 1 + \omega_p^2/\omega^2)^{-1/2}$. The normal mode frequencies are functions of α only, as shown in Fig. 2.2 for several of the lowest-order modes. The spatial structure of the modes is indicated in Fig. 2.3. Appendix B includes a discussion of the solution of Eq. (2.27). Explicit formulae for the Q_l^m functions are given in Appendix A. Chapter 4 presents a study of this class of modes in electron plasmas.

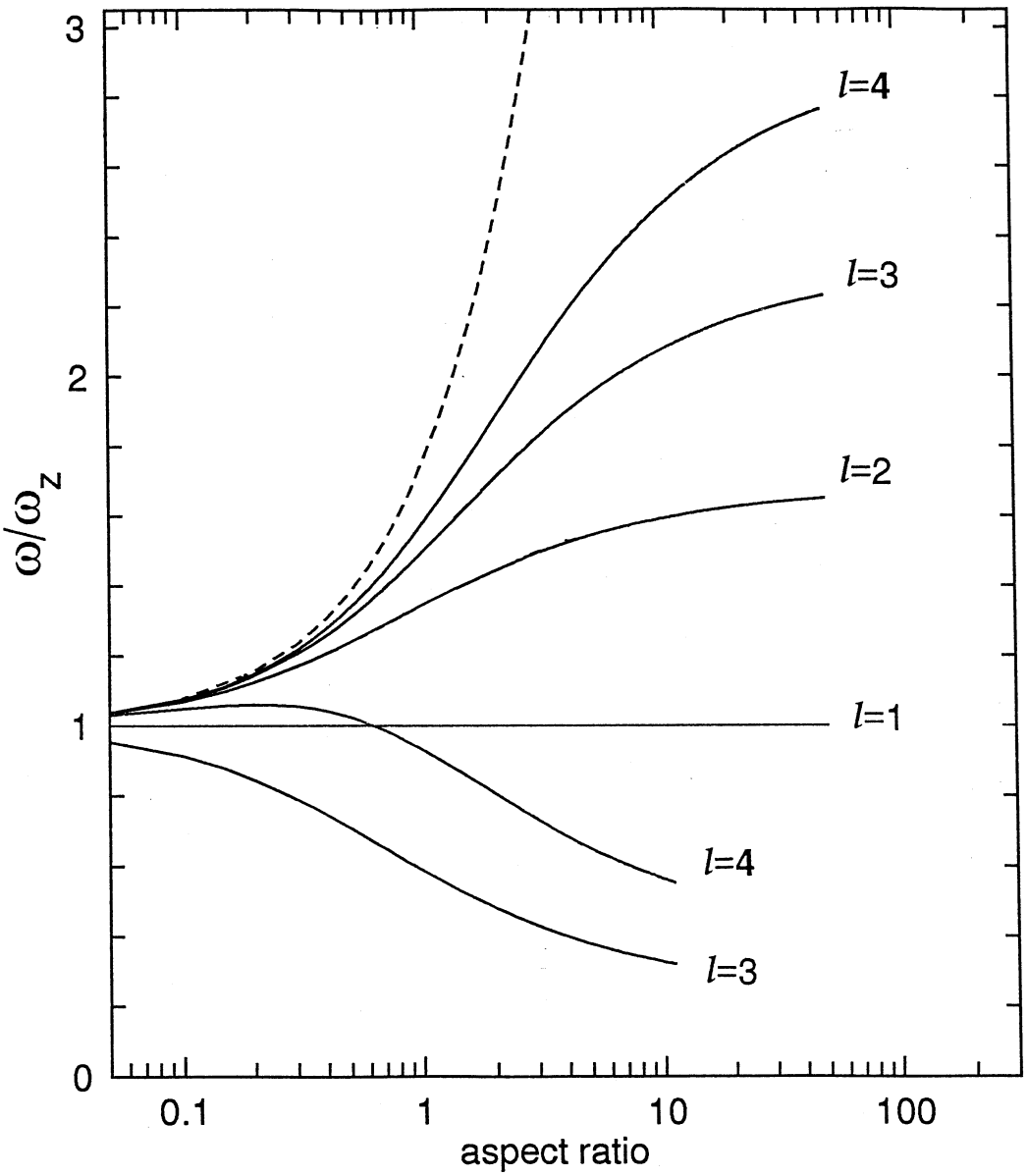

Figure 2.2: Axisymmetric modes ($m = 0$) of highly magnetized, cold, spheroidal plasmas: frequency as a function of aspect ratio for several low-order modes, scaled by ω_z. Multiple modes exist for each $l \geq 3$. The dashed line is the plasma frequency.

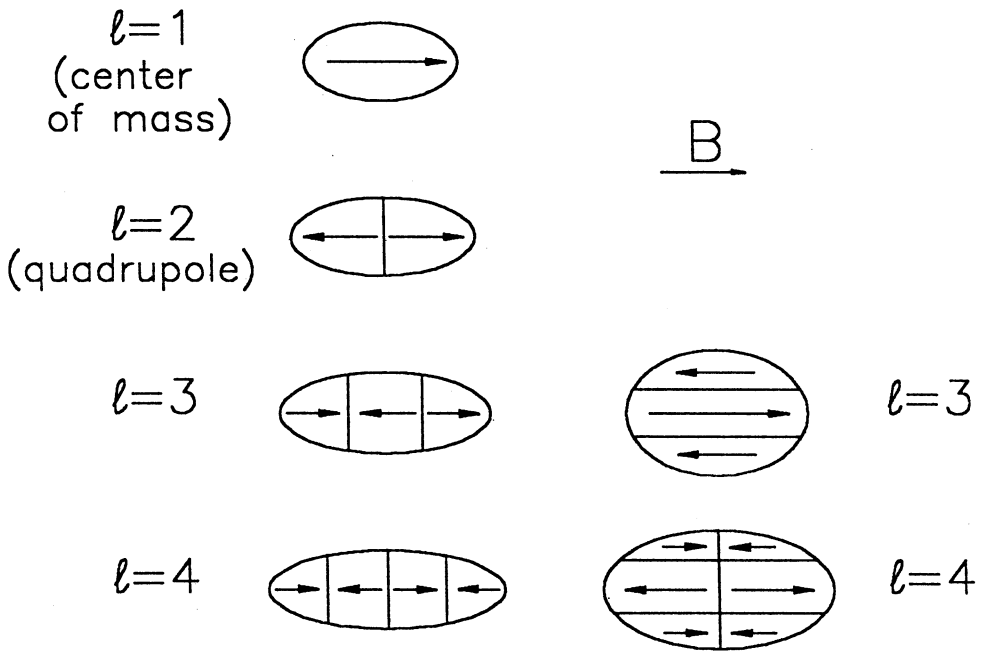

Figure 2.3: Structure of azimuthally symmetric ($m = 0$) normal modes of a highly magnetized plasma. Arrows indicate fluid motion during one phase of oscillation of the mode. For $l \geq 3$, multiple roots exist to Eq. (2.27), corresponding to modes with different radial structure, as shown. Purely axial modes have the highest frequencies.

Another set of modes of particular interest are the purely azimuthal modes, for which $l = |m|$. For positive m, they have frequencies

$$\omega_m = (m-1)\omega_r + \frac{\Omega_c}{2} \pm \frac{1}{2}\left[(\Omega_c - 2\omega_r)^2 + 2\omega_p^2 G_m(\alpha)\right]^{1/2}. \tag{2.28}$$

The geometrical factors,

$$G_m(\alpha) = 2\left[m - \frac{Q_m^{m\,\prime}(k_2)}{\alpha(\alpha^2-1)^{1/2}Q_m^m(k_2)}\right]^{-1}, \tag{2.29}$$

are plotted in Fig. 2.4 for $m = 1-5$. The plus and minus signs in Eq. (2.28) give solutions ω_m^+ and ω_m^- corresponding to the cyclotron and diocotron branches of the dispersion relation, respectively. The plasma rotation frequency may be found from ω_m^+ and ω_m^- for any $m > 1$:

$$\omega_r = \frac{\omega_m^+ + \omega_m^- - \Omega_c}{2m-2}. \tag{2.30}$$

These azimuthal "flute" modes are very similar to the analogous modes in a cylindrical single-component plasma. In the cylindrical case [*Davidson*, 1990], it is possible to include the effects of the image charge of the plasma. The mode frequencies again satisfy Eq. (2.28), with geometrical factors now depending on the ratio of the plasma radius, r_p, to r_w, the radius of the cylindrical wall, according to the relation $G_m(r_p) = 1-(r_p/r_w)^{2m}$. If image charges are neglected in the cylindrical case by letting $r_w \to \infty$, the geometrical factors reduce to $G_m(r_p) = 1$, and the mode frequencies match those of the $\alpha \to \infty$ limit of the spheroidal case, which did not include image charge effects.

2.3 Thermal Effects

The cold fluid equilibrium described above is valid if the Debye shielding length, $\lambda_D = (k_B T/4\pi n q^2)^{1/2}$, is much smaller than the size of the plasma, i.e., $\lambda_D \ll L, r_p$. Here T is the plasma temperature and k_B is the Boltzmann constant. In this

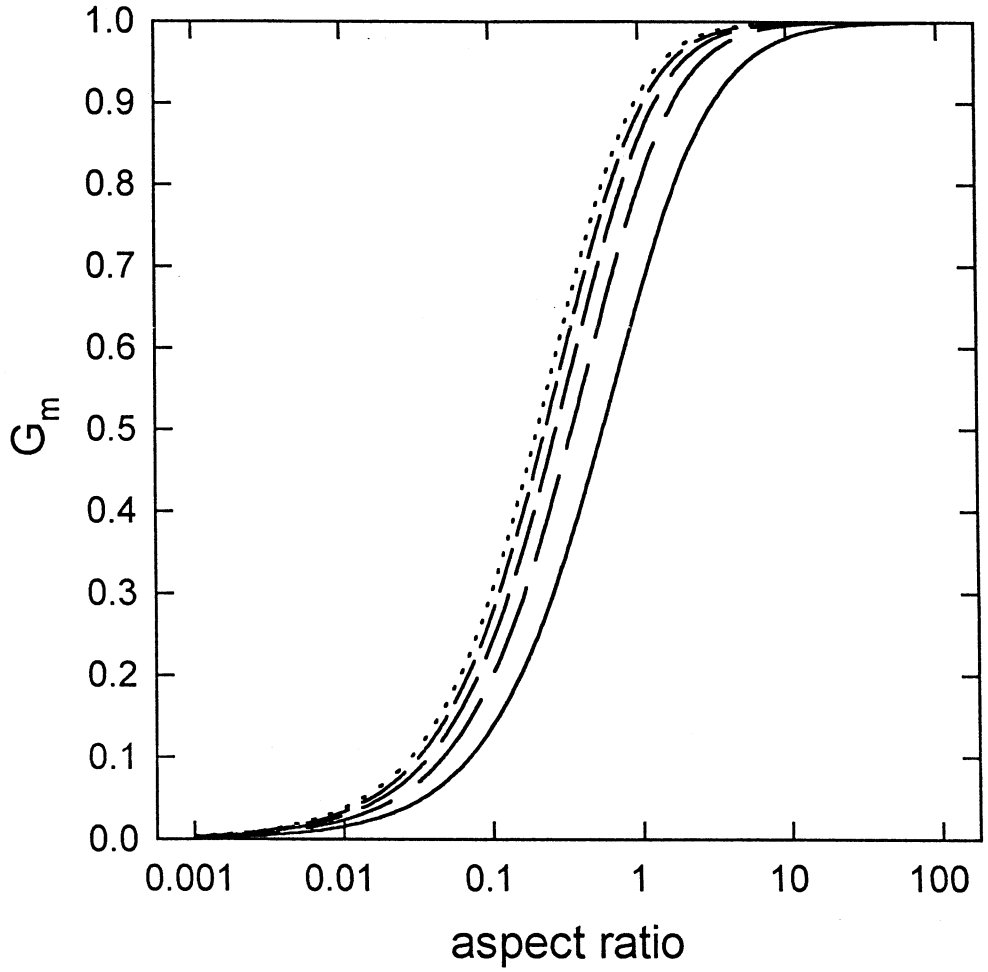

Figure 2.4: The functions $G_m(\alpha)$ from the azimuthal mode theory [Eq. (2.29)]. Solid line: $m = 1$; dotted line: $m = 5$.

case, the thermal equilibrium deviates from a uniform-density spheroid only at the edge, where the density falls to zero in a distance of a few Debye lengths. The plasma pressure causes the equilibrium spheroid to elongate slightly along the magnetic field. In the opposite limit, $\lambda_D \gg L, r_p$, the particle interactions are negligible compared to their thermal energy and the trap potential, and their distribution in z is a Gaussian, with $< z^2 >= k_B T/m\omega_z^2$.

The cold fluid mode theory also requires $\lambda_D \ll L, r_p$, but in addition, λ_D must be much smaller than the wavelength, λ, of the mode being considered. If this is not the case, the frequency of compressional plasma modes would be expected to increase due to the plasma pressure, and Landau damping will become important. As a result, even "cool" plasmas will show only a finite number of modes, and the most robust will be the lowest-order modes, which have the longest wavelengths. It is possible to estimate the effects of plasma temperature on the mode frequencies to first order in T [*Dubin*, 1993; *Dubin and Schiffer*, 1994], as described in Sec. 4.3. A warm fluid theory in which a pressure term is added to the fluid equation of motion is quite successful for low enough T, but is confounded by the occurrence of nonphysical acoustic modes for higher temperatures [*Spencer*, 1994].

Three of the global modes in the cold fluid theory are not truly plasma modes, but merely motions of the plasma center of mass. These motions, the axial bounce, cyclotron, and magnetron modes, should have frequencies independent of the plasma size, shape, and temperature in a perfect quadrupole trap, as long as image charges may be neglected.

2.4 Image Charges

Because the plasmas studied are not always small in either total charge or spatial scale (the ion plasmas extend to touch the electrodes), the effects of the charges drawn onto the electrodes to maintain constant potentials in the presence of the plasma (referred to as the plasma "image charge") are not always negligible. The attractive interaction between the plasma and its image charge modifies the effective trap potential from that of a perfect quadrupole, making the equilibrium non-spheroidal and complicating the prediction of mode frequencies. For a small plasma, however, the dominant effect of the image charge is to change the strength of the quadrupole potential to an extent proportional to the plasma charge, with a constant of proportionality dependent on the geometry of the trap electrodes.

The following approximate treatment of these effects proceeds from a suggestion by D. H. E. Dubin. The electric potential produced near the electrodes by a small plasma (i.e., $L/2, r_p \ll z_0$) of total charge Q in the center of the trap should be well approximated by the first terms in its multipole expansion, and dominated by the monopole term, which has the simple form $\Phi_{\rm m} = Q/r$. The surface charge distribution drawn onto the electrodes to maintain their equipotentials must produce a potential $-Q/r$ at the electrode surface. If the electrodes formed a spherical shell, this would be accomplished by a charge distribution which itself had only a monopole term. For more complex electrodes, the potential produced inside the trap by the image charge may be expanded as

$$\Phi_{\rm I}(r,\theta) = \frac{Q}{z_0}\sum_{l=0}^{\infty} B_l \left(\frac{r}{z_0}\right)^l P_l(\cos\theta), \tag{2.31}$$

where azimuthal symmetry has been assumed. The unitless coefficients B_l are determined by the requirement $\Phi_{\rm I}(r(\theta),\theta) = -Q/r(\theta)$, where $r(\theta)$ is the equation of the electrode surfaces. Near the center of the trap, only the lowest-order terms are

important. The monopole term ($l = 0$) represents an unimportant shift in the zero of the potential. For electrodes that are symmetric about $z = 0$, the coefficients vanish for odd values of l, so there is no dipole term. The quadrupole term ($l = 2$) changes the trap quadrupole field from one described by the frequency ω_z to one described by ω_z^*, where

$$(\omega_z^*)^2 = \omega_z^2 - \frac{2qQ}{mz_0^3}B_2. \tag{2.32}$$

The spheroidal equilibrium and normal mode frequencies will be altered accordingly.

For the special case of the center-of-mass mode, the assumption that odd-l coefficients vanish is not valid, because the plasma has a time-varying dipole moment. A treatment similar to that just described for the quadrupole image charge field induced by the monopole moment of the plasma may be used to calculate B_1 and higher coefficients. When the force on the plasma due to this time-dependent induced dipole is calculated, it is found to have the same effect on the center-of-mass motion as is produced by the static quadrupole field induced by the plasma monopole moment, resulting in harmonic oscillation at a frequency $\omega_{\rm CM}$ given by

$$\omega_{\rm CM}^2 = \omega_z^2 - \frac{2qQ}{mz_0^3}(B_1 + B_2). \tag{2.33}$$

Plasmas that are not much smaller than the trap may still have only minor effects from image charge, but the coefficients (possibly even their sign) will depend on the plasma length and radius, as well as the total charge [*Turner*, 1987]. A numerical Poisson solution would be required to determine the image charge field for a particular plasma.

2.5 Anharmonicity

Deviations of the trap potential from a perfect quadrupole will affect the plasma equilibrium and the mode frequencies. The precision of a particular set of

electrodes is customarily [*Brown and Gabrielse*, 1986] described in terms of unitless coefficients in an expansion of the potential about the center of the trap:

$$\Phi(\rho, z) = V(z^2 - \frac{1}{2}\rho^2)/z_0^2 + V\sum_{l=0}^{\infty} C_l \left(\frac{r}{z_0}\right)^l P_l(\cos\theta). \tag{2.34}$$

In an ideal trap, all of the C_l coefficients are zero, and in practice, all of the odd-l coefficients are usually assumed to be negligible due to symmetry about $z = 0$ maintained during the construction of the electrodes. The coefficient C_0 represents an unintentional (and unimportant) DC offset to the potential, and C_2 describes a deviation of ω_z from its design value. C_4, the coefficient of the quartic term, is a measure of the trap imperfection, or anharmonicity. Precision traps have compensation electrodes in the asymptotic region of the trap which make it possible to approximately zero C_4. The optimum configuration for this purpose is one that produces no change in C_2 as C_4 is adjusted, which is obtained for $\rho_0 \simeq 1.16 z_0$ [*Brown and Gabrielse*, 1986]. The asymptotically symmetric design approximated by our trap ($\rho_0 = \sqrt{2} z_0$) is not the optimum, but has nevertheless been used for most precision trap experiments.

C_4 is a useful figure of merit for a trap, but does not sufficiently describe a trap if large plasmas are to be studied. A set of carefully chosen cylindrical electrodes can be made to null both C_4 and C_6 coefficients in the potential [*Gabrielse et al.*, 1989], but will nonetheless deviate greatly from a quadrupole field near the electrodes, which do not lie along equipotentials of such a field. For large plasmas, or when large-amplitude motions of single trapped particles are expected, the hyperboloidal geometry shown in Fig. 2.1 may be preferable.

It is possible [*Dubin*, 1994] to estimate the effect of a small trap anharmonicity on the mode frequencies. One important effect of a substantial anharmonicity is that the plasma center-of-mass mode frequency becomes dependent on the size and shape

of the plasma.

Chapter 3

Description of the Experiment

This chapter describes the experimental apparatus used to form and confine single-component plasmas of various species and explains the methods employed to measure the equilibrium properties and normal mode frequencies of the plasmas. Techniques specific to the ion plasmas are described in Ch. 5.

3.1 Plasma Formation

The equipment used for these experiments can form single-component plasmas of positrons, electrons, or ions, which may be confined in a cylindrical electrode structure or in a set of hyperboloidal electrodes.

3.1.1 Positron Source and Trapping

Because it was designed to trap positrons by gas scattering [*Wysocki et al.*, 1988; *Surko et al.*, 1989; *Murphy and Surko*, 1992], the Penning trap used for these experiments has a rather complicated electrode structure, as shown in Fig. 3.1. The cylindrical electrodes have inner diameters that increase by a factor of 23.8 from the front of the trap, where positrons enter, to the back, where they are eventually confined. Vacuum pumps at both ends and in the middle of the trap combine with

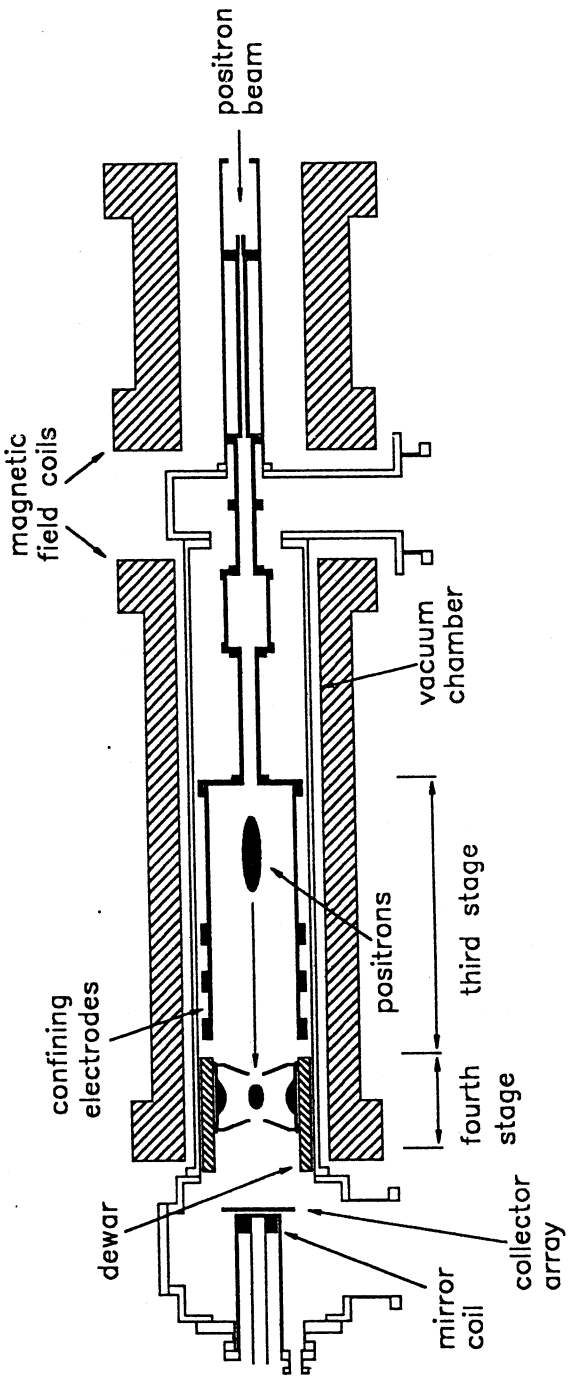

Figure 3.1: The positron trap.

this structure to provide differential pumping of a buffer gas, typically N_2, introduced into one of the narrow electrodes, producing the pressure variation indicated in Fig. 3.2. The electrodes are biased to provide the potential shown in Fig. 3.2 along the axis of the trap. Guided by the strong axial magnetic field, positrons enter the trap with an energy of about 32 eV and, if a collision with a gas molecule does not occur, they will reflect from the potential barrier at the far end of the trap and return to their source. Though elastic collisions could provide temporary confinement by scattering $E_{||}$ (kinetic energy parallel to B) into $E_{\perp}$ (kinetic energy perpendicular to B), energy lost in inelastic collisions provides the dominant trapping mechanism [*Murphy and Surko*, 1992]. The buffer gas pressure is such that, on average, a particle undergoes one such collision, most likely in Stage I, during a pass through the trap. The positron beam energy and the electrode potentials are adjusted to maximize the cross-section for the desired inelastic process (an electronic excitation), while minimizing the cross-section for the formation of positronium, which results in loss of the positron. After the initial collision resulting in confinement, the positron bounces back and forth in the trap, losing energy by additional collisions, until it is eventually restricted to Stage III, where vibrational and rotational collisions gradually reduce its energy to room temperature, the temperature of the buffer gas. Computer optimization of the electrode potentials has raised the efficiency of this trapping process to about 40%.

The positrons are produced by a radioactive source, a thin film 6 mm in diameter containing about 70 mCi of ^{22}Na, covered by a 0.1-μm-thick titanium window. ^{22}Na decays to ^{22}Ne with a radioactive half-life of 2.60 years, producing a 1.275 MeV γ-ray accompanied, 89.8% of the time, by a positron, which may have any energy up to 546 keV. To shield the γ-rays, the source is centered in a thick cylinder of HeavyMet (a machinable alloy of 90% tungsten and 10% copper) inside a

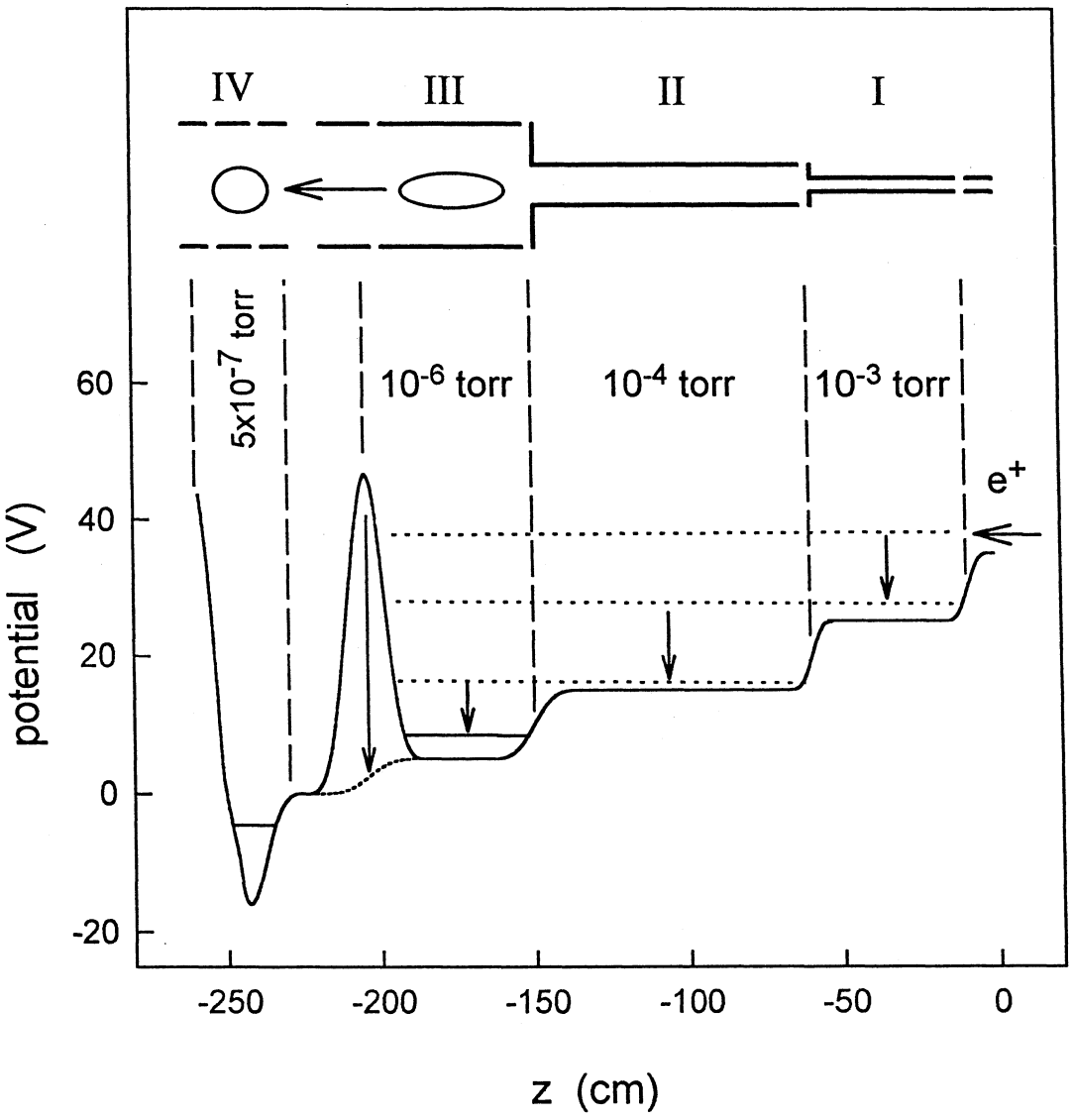

Figure 3.2: Potential along the axis of the positron trap, with a schematic of the electrodes. Roman numerals label the different "stages" of the trap, which have the neutral gas pressures indicated.

vacuum chamber which is surrounded by a 4-inch thickness of lead bricks. Because of the broad energy range of the positrons and the continuous and isotropic nature of their emission, no efficient technique of directly trapping the high-energy positrons is known. Instead, a 1-μm-thick single-crystal tungsten foil is placed in front of the source to act as a moderator [*Gramsch et al.*, 1987; *Zafar et al.*, 1988]. A small fraction of the positrons striking the moderator slow down and thermalize near enough to the front surface of the foil to have a chance of diffusing to the surface before annihilating. Because the work function for positrons in tungsten is about -2 eV, these positrons are emitted from the moderator with an energy about 2 eV higher than the moderator bias potential, which may be varied. The efficiency of the moderator, defined as the ratio of slow positrons produced per positron emitted by the source, is subject to a number of poorly understood effects, but with proper heat treatment in the presence of a low pressure of oxygen, it is typically 0.01 - 0.02%. About half the positrons produced strike the moderator, resulting in a beam strength of about 6×10^5 low-energy positrons per second, and a production of 3×10^5 trapped positrons per second. We have recently installed a new type of moderator consisting of a film of solid neon frozen onto the source window and a surrounding paraboloidal copper cone [*Mills and Gullikson*, 1986; *Khatri et al.*, 1990]. This is effected by mounting the source assembly onto the cold head of a 2-stage cryogenic refrigerator. The neon moderator has a considerably higher efficiency than the tungsten moderator, and has so far produced 2×10^6 trapped positrons per second [*Surko and Greaves*, 1994].

Trapped positrons are eventually lost due to annihilation with electrons in neutral gas molecules, resulting in a mean positron "lifetime", τ_a, and an annihilation rate of $1/\tau_a$ per positron. The maximum number of positrons that may be accumulated is the product of the trapping rate and the positron lifetime. During

the initial experiments with the positron trap [*Surko et al.*, 1988; *Wysocki et al.*, 1988], it was discovered that the positron lifetime was limited not by annihilation on the buffer gas molecules, but by annihilation on the traces of hydrocarbon molecules present at the base pressure of the vacuum system. The vacuum chamber is sealed in key places by rubber o-rings, which limit the temperature to which it may be safely baked and are also a potential source of hydrocarbons. Substantial improvements were obtained by replacing the original diffusion pumps by turbopumps and then by cryopumps, and by regreasing the accessible o-rings with a flourocarbon compound (Fomblin) with a very low vapor pressure. Still, the positron lifetime was dominated by constituents of the system base pressure (about 2×10^{-9} torr) and fluctuated from day to day, with a typical value of $\tau_a \simeq 20$ s. This problem was finally solved by positioning an annular dewar filled with liquid nitrogen near the confinement region to reduce the partial pressure of condensable gases. This is so effective that if the buffer gas flow is shut off after loading Stage IV of the trap with positrons, the positron lifetime increases to about 1500 s (see Fig. 3.3(b)). During normal operation, annihilation on the buffer gas results in a lifetime during trapping of $\tau_a = 60$ s, about what had originally been expected. Figure 3.3(a) shows the number of positrons stored as a function of time since the start of trapping, and then the exponential decay of the number stored after the beam is shut off at the time indicated. The self-field of the plasma is sufficient to change the trapping efficiency as the plasma accumulates, resulting in a filling timescale somewhat longer than the annihilation time, τ_a. This dataset is typical of results obtained with the new neon moderator, showing a maximum number of 10^8 positrons.

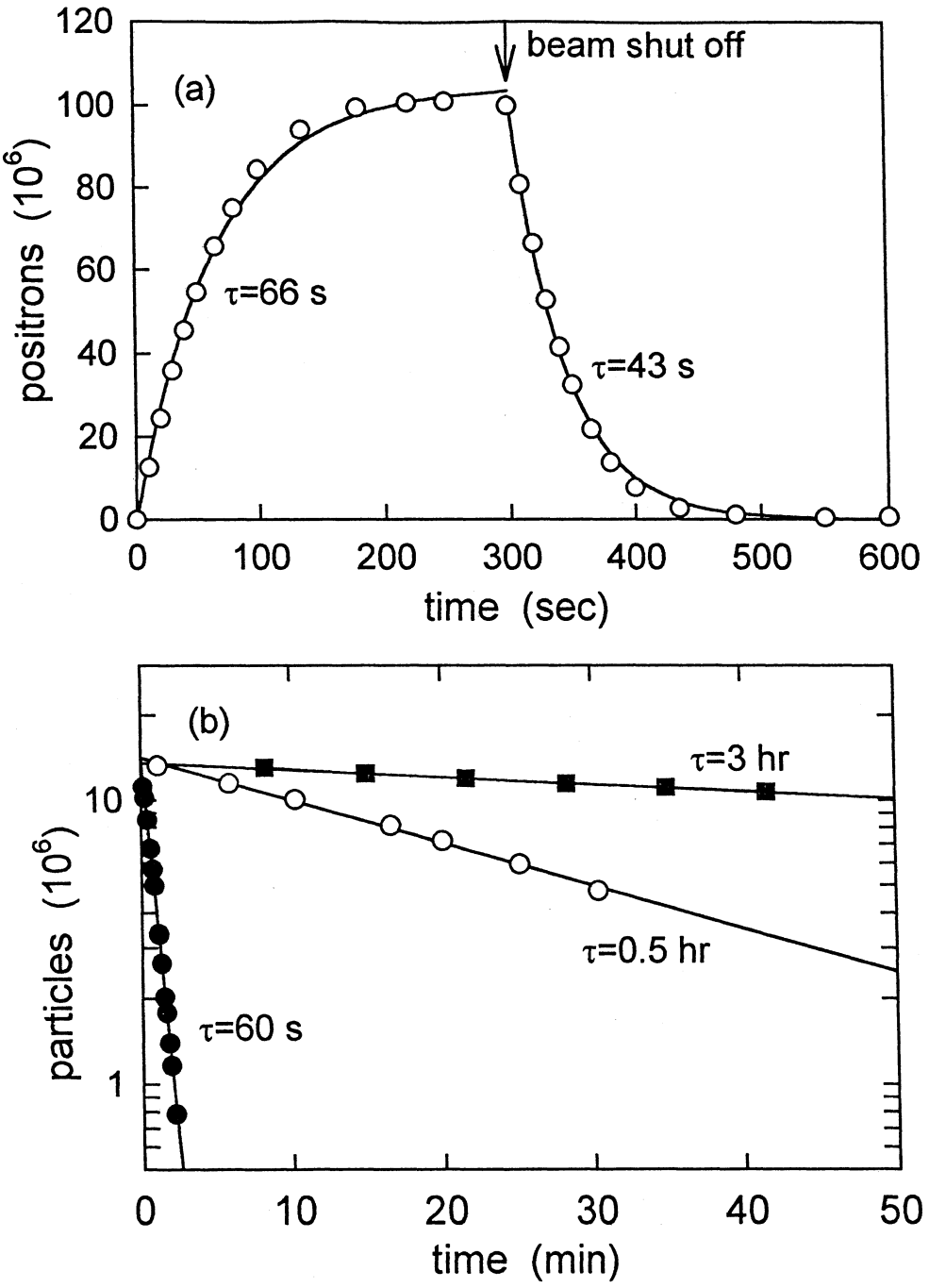

Figure 3.3: (a) Filling and storage of positrons in Stage III, with $B = 1.2$ kG. (b) Confinement of positrons and electrons in Stage IV, with $B = 1.5$ kG: (•): positrons, with buffer gas; (o): positrons, no buffer gas; (□): electrons, no buffer gas.

3.1.2 Electron Source

If the sign of all of the electrode potentials used for positron trapping is reversed, electrons can be trapped, though not at the highest possible efficiency. It was found that the positron moderator emits a substantial number of electrons, so that a separate source, such as the spiral filaments used in most electron plasma experiments [*Malmberg and de Grassie*, 1975; *Driscoll and Malmberg*, 1976], was not necessary. The electrons, which are probably secondary electrons produced by the high-energy positrons streaming through the moderator, have a broad energy range up to 60 eV or more, and for long-time confinement studies it is necessary to shut off the solenoid between the source and the trap, in addition to biasing the moderator, to completely shut off the beam. The trapping rate can be adjusted to be comparable to the positron filling rate, or increased to be about an order of magnitude higher. The confinement of electrons is very good, as indicated in Fig. 3.3(b), where an exponential loss time of 3 hours is seen when the buffer gas is pumped out. This time appears to depend on the condition of the vacuum, and does not appear to follow the B^2/L^2 scaling law observed by Driscoll [*Driscoll and Malmberg*, 1983], suggesting that the losses are dominated by a process other than field-error-driven transport. Because there are no annihilation losses, and the confinement time is high, the limit to the number of stored electrons appears to result from the plasma space charge, which can become comparable to the confinement potentials.

3.1.3 Ion Source

Although the electron plasmas studied in this work were formed using secondary electrons from the moderator, an electron gun has been built recently for use in electron beam - positron plasma experiments. This gun is used to create the

ion plasmas we have studied, by ionizing gas atoms. The trap potentials are set to confine ions, many of which are created in the confinement region and thus do not need to lose energy to become trapped. Further details on this technique are provided in Ch. 5.

3.2 Hyperboloidal Electrodes

The early electron plasma experiments in this machine were performed with plasmas confined in the original cylindrical electrode structure. The unitless anharmonicity parameter for this structure, defined by analogy to Eq. (2.34) but with the cylinder radius, r_w, replacing z_0 as the distance scale, is $C_4 \simeq 0.482$. Because of evidence, described in Sec. 4.1, that the anharmonicity was affecting the plasma mode frequencies and impeding the remote detection of positrons, a new electrode structure, shown in Fig. 3.4, was designed to approximate the truncated hyperboloidal electrodes of a precision quadrupole trap. There are no compensation electrodes in the asymptotic region, and the electrodes are truncated in the simple fashion shown. To reduce the effect on the differential pumping caused by an obstruction, most of the surface of the endcaps consists of a mesh with about 66% transmission. The holes required on the axis of the endcaps for particle entry have the same diameter (4.32 cm) as the inner diameter of the electrodes of Stage II of the trap, to avoid introducing a new positron loss mechanism. Numerical calculations with a Laplace solver indicated that with such large holes, there was no advantage in making the remainder of the endcaps precisely hyperboloidal, so a conical approximation was made to the desired surface. This made the task of forming and attaching the mesh to the machined frame of the endcaps much simpler. The ring electrode, a hyperboloid truncated by a cylinder, was machined using a computer-numerically-controlled (CNC) lathe. A CNC milling machine was used to machine tabs on the

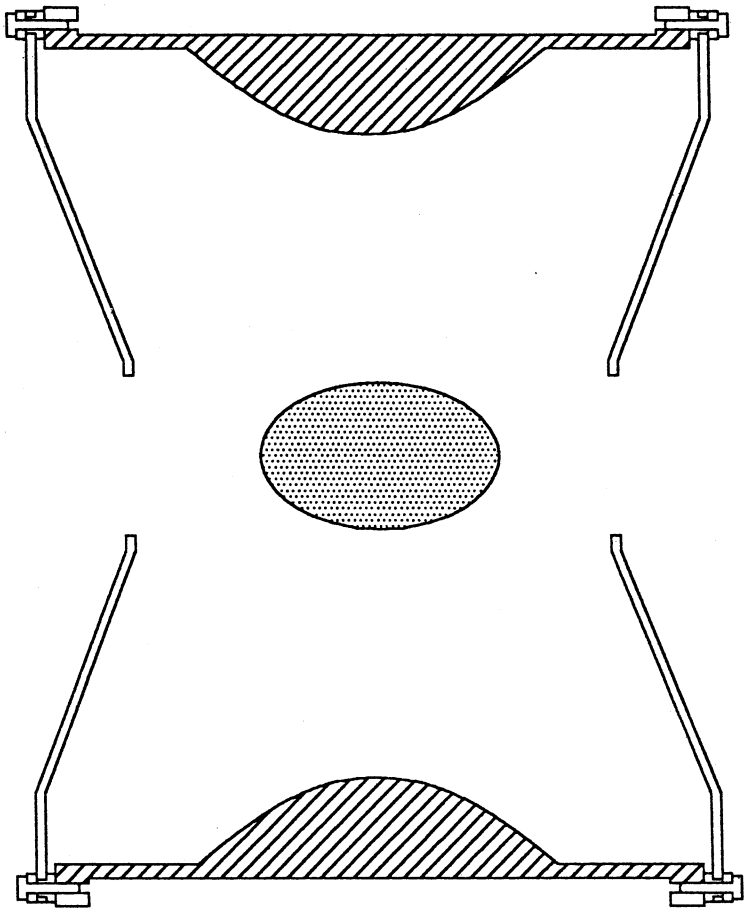

Figure 3.4: Approximate quadrupole trap electrodes, with a typical plasma shown.

endcaps and on the cylindrical portion of the ring electrode, for electrical connections and to attach them together.

The electrodes were made of aluminum for economy and ease of machining, then plated with gold on silver on copper. This plating cannot be safely baked to temperatures greater than 120°C, due to concerns about the strength of the copper-aluminum bond, but it is much less expensive than the gold on palladium plating and copper electrodes required for a high-temperature bake. The plating was not a limitation in our experiment, as we are not able to bake our o-ring sealed vacuum system to temperatures above 70°C. The same plating was applied to the aluminum mesh, which was attached to the endcap frame by gold-plated brass screws. Beryllium-copper screws were used to assemble the electrodes, with Macor washers providing electrical isolation between the parts. The cabling to the electrodes is 50Ω semi-rigid coaxial cable with a solid copper jacket and Teflon dielectric. While this cable is not designed for vacuum applications, it does not noticeably affect the system base pressure.

The electrodes are designed to approximate an asymptotically symmetric quadrupole trap [see Eq. (2.1)] with $z_0 = 6.3$ cm. The anharmonicity coefficient for this structure is nominally $C_4 \simeq 0.055$, but is influenced by external potentials because of the large holes in the endcaps. Figure 3.5(a) shows the calculated axial bounce frequency as a function of radius for a single particle in the trap, showing a substantial improvement over the cylindrical structure. Another result of anharmonicity is the variation of the bounce frequency with bounce amplitude, shown in Fig. 3.5(b). A better comparison of the two traps is obtained if both values of C_4 are defined by the same distance scale. Using z_0 as the scale, the results are $C_4 \simeq 0.24$ for the cylindrical trap, compared to 0.055 for the quadrupole trap. The relatively modest reduction in the anharmonicity resulted in large qualitative improvements in

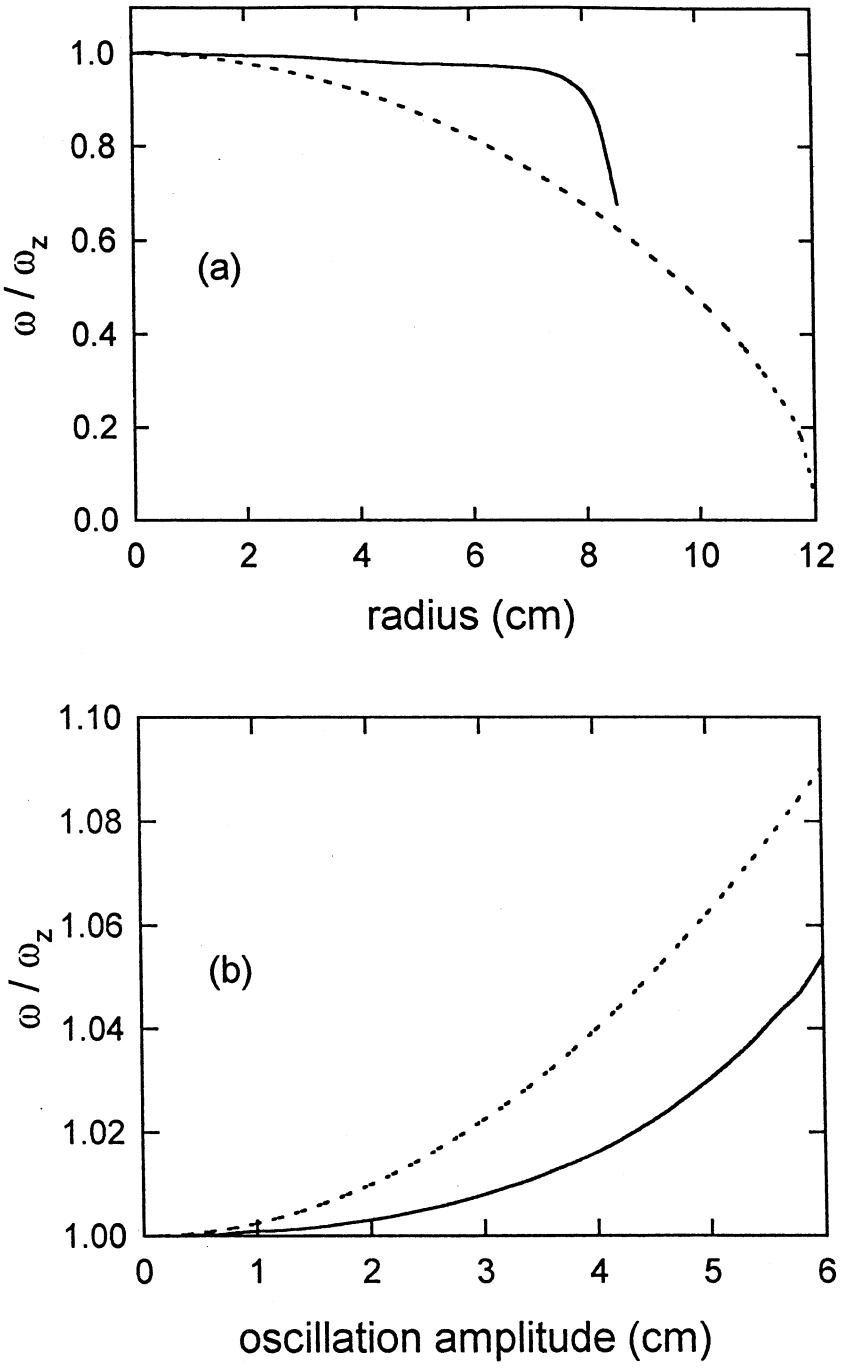

Figure 3.5: Comparison of anharmonicities of cylindrical electrodes (dotted curves) and approximate quadrupole electrodes (solid curves). (a): ω_z vs. ρ, and (b): ω_z vs. amplitude of oscillation.

the data, which will be described in Ch. 4. In addition, the new electrodes are considerably closer to the plasmas, resulting in a great improvement in signal coupling between them.

To allow the observation of plasma modes with azimuthal variation and to enable us to measure the mass of ions produced by positron annihilation [*Passner et al.*, 1989; *Glish et al.*, 1994] using ion cyclotron mass spectrometry, the ring electrode was recently replaced by an azimuthally sectored structure. The surfaces of the new structure are the same as before, but the cylindrical part of the electrode is now a separate piece, to which the original endcaps are attached, as before. The hyperboloidal surface was machined separately using a CNC lathe and cut into 8 azimuthal sectors by electrical discharge machining (EDM). Each sector is attached to the cylinder by a pair of titanium screws insulated from the cylinder by Macor washers. The sectors are isolated from the cylinder by a sheet of Teflon 0.005 inches thick, and separated from each other by about 0.020 inches, the amount of material removed by the cutting process. The sectors were aligned manually, since it was felt that the imperfections of the endcap mesh made a more painstaking procedure pointless. Semi-rigid coaxial cables are guided around the outside of the cylinder by Teflon supports and connected to the titanium screws to make electrical contact with each sector.

3.3 Density Measurement

The radial distribution of charge stored in the trap can be measured by reducing the voltage on one of the confining electrodes, causing the trapped electrons or positrons to stream out of the confinement region along the magnetic field lines. The "dumped" charge strikes the set of 11 concentric annular collector plates indicated in Fig. 3.1 and shown in more detail in Fig. 3.6. The charge accumulated by a

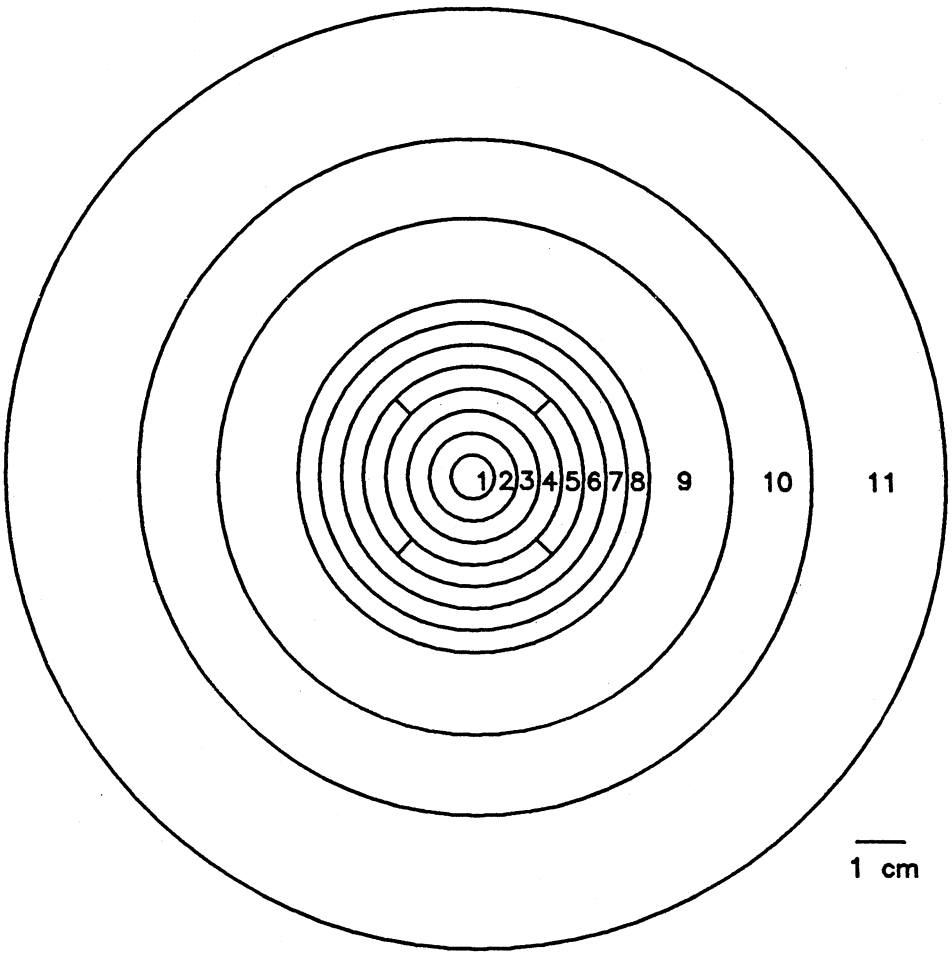

Figure 3.6: Collector plate array.

ring can be measured using a charge-sensitive amplifier, which has a noise level corresponding to about 10^4 electrons. The amplifier is a Canberra Model 2002 preamp (ordinarily used with Germanium gamma-ray detectors), followed by a standard spectroscopy amplifier with a 1-μs shaping time. The amplifier gains are typically adjusted to give an overall sensitivity of 1 volt per 10^6 electrons. A switch box is used to select the collector. The collector array is located outside the main solenoid, so the spreading field lines give a view of the plasma magnified by $\sqrt{B_0/B_c} \simeq 1.76$, where B_c is the magnetic field at the collectors. This results in a spatial resolution at the plasma of 0.27 cm for the inner 8 collectors. Nominally, these are the collectors that map to the hole in the endcap through which the charge is dumped, while collector 9 should be completely obstructed by a central ring structure on the endcap and collectors 10 and 11, which are much larger, receive charge dumped through the endcap mesh. It appears that collector 8 is partly obstructed and collector 9 receives some charge, so that the magnetic field ratio used for the design and field mapping may be slightly in error. Collector 5 is split azimuthally into 4 sectors. The Macor block on which the collector array is mounted can be centered on the magnetic axis of the trap by positioning it so that equal charge is dumped onto each of these sectors. This technique is most accurate if the plasma used has a radius comparable to the average radius mapped by collector 5. The collectors are gold-plated aluminum (the same plating as was used for the hyperboloidal electrodes) machined to overlap so that all charge within the outer radius of the array is collected, avoiding charging of the support block.

Dividing the charge measured on a collector by the area to which it maps gives an estimate of the z-integrated plasma density, q_z, at the average radius to which the collector maps. Figure 3.7 is an example of density measurement data, showing the radial profile of an electron plasma relaxing from an initial peaked dis-

tribution to a more uniform profile. The neutral gas pressure is substantial (about 10^{-6} torr), so some overall expansion occurs as well. To infer plasma density from these z-integrated profiles requires a numerical calculation in which Poisson's equation, $\nabla^2\Phi(\rho,z) = -4\pi qn(\rho,z)$, is solved with the proper electrode geometry and potentials. It is assumed that the plasma is in local thermal equilibrium along each magnetic field line and that there is no azimuthal variation, so that the density at each radius has a Boltzmann distribution

$$n(\rho,z) = q_z(\rho)C(\rho,T)e^{-q\Phi(\rho,z)/k_BT}, \tag{3.1}$$

where Φ is the total potential, including the self-consistent field of the plasma. $C(\rho,T)$ is a normalization constant associated with the Boltzmann factor, and $q_z(\rho)$ is the z-integral of $n(\rho,z)$, the data input to the program. In principle, the plasma temperature, T, could be a function of ρ, as might occur if rapid radial transport leads to Joule heating, but we always assume a uniform temperature, which is usually 300K. The computer program makes a guess of the total potential and distributes the known number of particles at each radius according to this potential using Eq. (3.1). It then solves Poisson's equation to find a new estimate for Φ, and iterates the procedure until adequate convergence is achieved. This algorithm is subject to various convergence problems, but works reasonably well as long as the Debye length of the actual equilibrium is much larger than the grid spacing used in the calculation.

Because the plasmas are nominally spheroidal, an approximate analysis of radial profile data can be made without resorting to the Poisson solver. The central value measured for $q_z(\rho)$ is approximately the product of the plasma length and its central density, $n_{\max}$:

$$q_0 = Ln_{\max}. \tag{3.2}$$

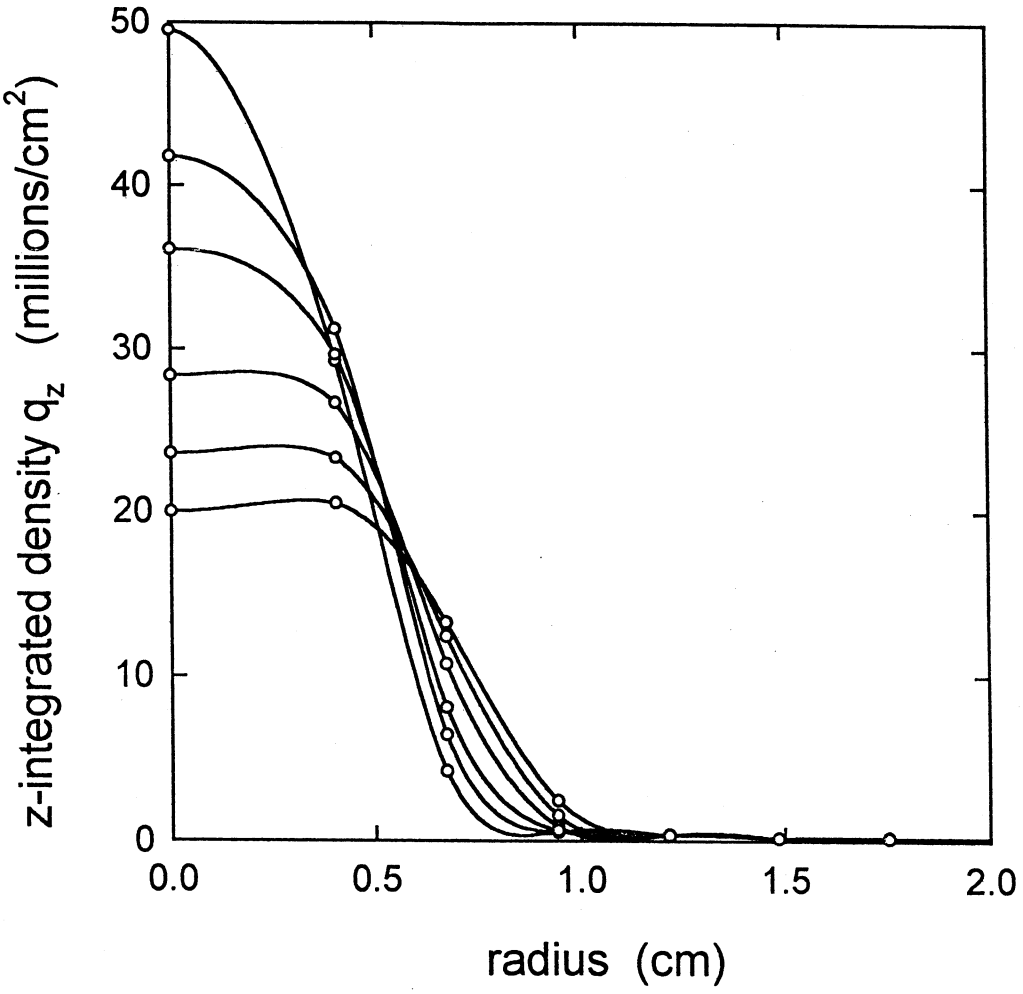

Figure 3.7: Radial density profiles of plasma relaxing toward thermal equilibrium. Data were taken at times 0, 10, 20, 40, 60, and 80 seconds after filling, with early times corresponding to higher central density. The smooth curves are a guide.

N is known from the total charge measured, and assuming a uniform-density spheroid leads to an estimate, $\hat{r}_p$, of the plasma radius:

$$\hat{r}_p = \left(\frac{3N}{2\pi q_0}\right)^{1/2}. \tag{3.3}$$

Using the equilibrium equation, we can find an equation for the aspect ratio in terms of measured quantities:

$$\frac{2\alpha}{A_3(\alpha)} = \frac{q_0}{2\hat{r}_p n_0}, \tag{3.4}$$

where

$$n_0 = \frac{V}{2\pi q z_0^2} \tag{3.5}$$

can be considered as a characteristic particle density associated with the trap field ($\omega_z^2 = 4\pi n_0 q^2/m$). Then L and $n_{\max}$ are easily found from these quantities. Other definitions of the radius of a plasma with a nonuniform density, such as the mean square radius or the radius at which the density is half its maximum value, may be more appropriate for some purposes. This approach compares well with Poisson solutions for the equilibrium parameters.

The density diagnostic is not useful for the ion plasmas we have studied because they have densities near the Brillouin limit. As a result, the ions are effectively unmagnetized in a frame rotating with the plasma, so they do not follow magnetic field lines to the collectors when dumped. An additional problem is the large size of the plasmas studied, many of which extend out to the ring electrode. The techniques developed to determine the ion plasma density are described in Ch. 5.

3.4 Temperature Measurement and Heating

We use the standard "magnetic beach" technique to measure the temperature of the electron and positron plasmas [*Hsu and Hirshfield*, 1976]. A small water-cooled coil is positioned behind the collector array, as shown in Fig. 3.1, and its

current is adjusted to make the total magnetic field at the collectors equal to the field in the confinement region. A series of nominally identical plasmas are formed and dumped with varying potential biases on the collectors, and the total charge received is recorded. In principle, this curve contains information on the velocity distribution of the plasma and can be used to deduce the plasma temperature [*Eggleston et al.*, 1992], but this is complicated by the plasma potential. Instead, the field at the collectors is increased to produce a magnetic mirror, and the data set is retaken. To first order, the effect of the mirror field is to shift the curve, because a lower collector bias is capable of reflecting the particles with the assistance of the mirror. The slopes of the two curves at their midpoints are used to estimate $\partial N/\partial V_b$ and the separation between the curves gives an estimate of $\partial N/\partial R$, where R is the mirror ratio. The temperature is the ratio of these quantities,

$$k_B T = q\frac{\partial N/\partial R}{\partial N/\partial V_b}. \tag{3.6}$$

The data shown in Fig. 3.8 are for two different temperatures: $k_B T = 0.3$ eV (Fig.3.8(a)), and $k_B T = 0.025$ eV (Fig.3.8(b)). The mirror field for these datasets was provided by moving a permanent magnet into the position now occupied by the mirror coil. This earlier technique is less accurate than using the mirror coil because the mirror ratio without the magnet is 0.34 (causing acceleration of particles) and it increases to about 1.3 with the magnet in place. In either case, the mirror field has to make up for the loss in the field of the main solenoid. As a result, the temperature measurements can only be made for $B \simeq 900$ G or less.

Temperature measurements made at varying times after the rapid introduction of a small number of electrons or positrons into the trap allow the cooling of the particles by collisions with the buffer gas to be observed. As shown in Fig 3.9(a), the plasma approaches its final temperature with an exponential cooling time-constant

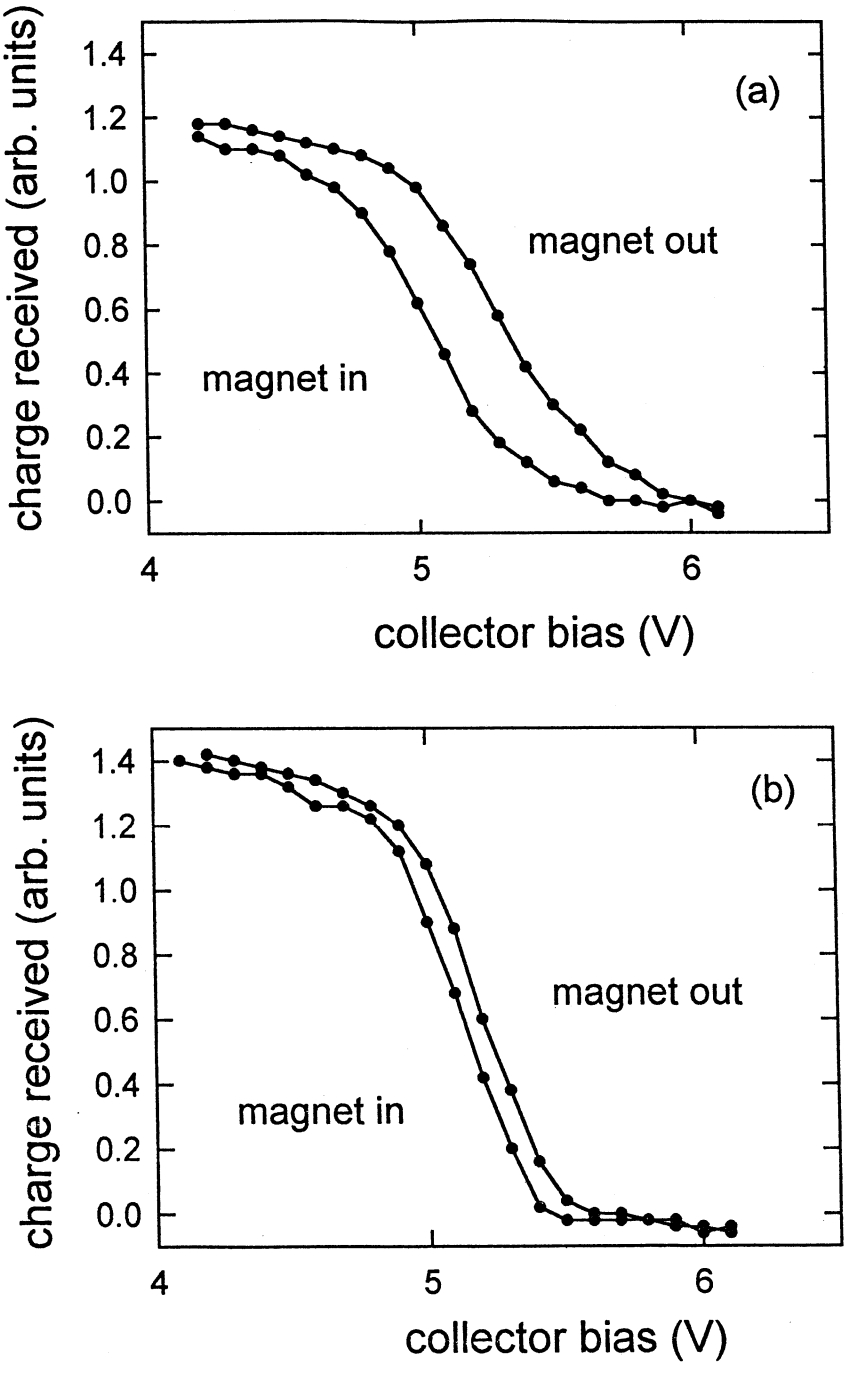

Figure 3.8: Raw data for magnetic beach temperature analyzer for (a): $k_B T = 0.3$ eV, and (b): $k_B T = 0.025$ eV. Mirror field provided by permanent magnet: $R \simeq 1.3$ with magnet in place, $R \simeq 0.34$ with magnet out.

of $\tau_c \simeq 0.6$ s. We have assumed that this final temperature is the temperature of the buffer gas, i.e., 300 K, and used this to calibrate the measurement. The resulting scale factor of 0.85 probably arises from imperfections in the geometry of this magnetic beach, principally the variation in the strength of the mirror field over the surface of the collector array and the location of the collectors outside the main solenoid.

The plasma may be heated to about 0.5 eV by the application of broadband rf noise to one of the electrodes. The noise is produced by an unfiltered pseudo-random noise source with a center frequency of 11 kHz, a peak-to-peak amplitude of typically 50 mV, and frequency components up to about 10 MHz. The plasma temperature rises quickly to a maximum, above which we speculate that an inelastic collision process, such as vibrational excitation of N_2 molecules, provides strong enough cooling to stabilize the temperature. After the heating pulse is shut off, the plasma cools toward room temperature, as shown in Fig. 3.9(b). To study plasmas of a particular temperature in the range $0.025 \leq k_B T < 0.5$ eV, we wait for the appropriate time after the application of a standard heating pulse.

3.5 Mode Excitation and Detection

Normal modes of the plasma are studied by applying sinusoidal signals to one electrode and measuring the signals induced on another. As shown in Figure 3.10(a), the two endcaps are used for the study of modes with no azimuthal variation. To study azimuthal modes, the signals are applied and detected on two or more of the sectors of the ring electrode, as shown in Fig. 5.1. A spectrum analyzer with a tracking generator is used to sweep the excitation frequency to find resonances. Typical mode frequencies are 3 MHz for the axial modes of electron plasmas and 30 kHz for the azimuthal modes of ion plasmas. Consequently, different spectrum

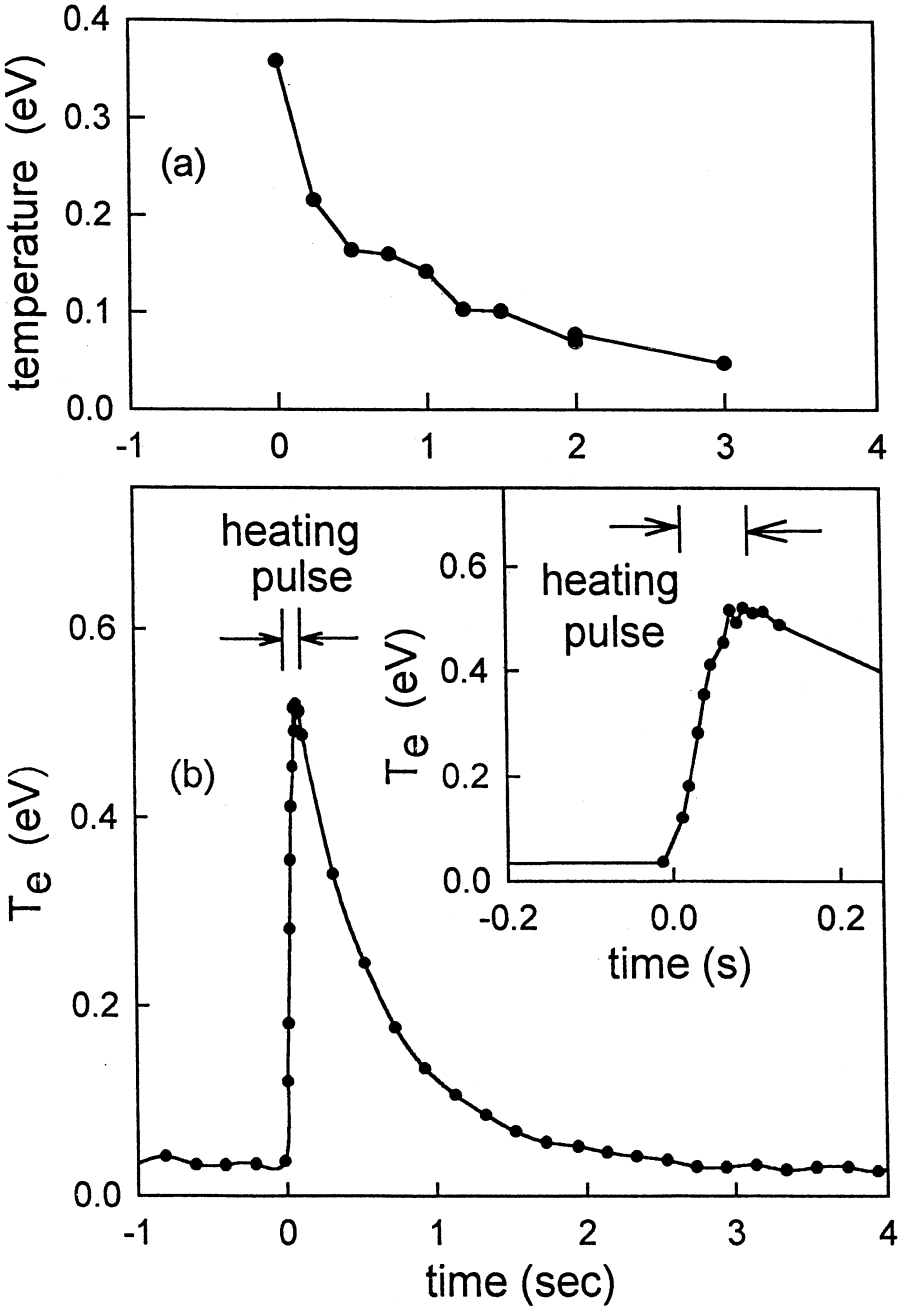

Figure 3.9: (a) Temperature as a function of time after particle trapping. (b) Plasma heating by rf noise, followed by cooling. The inset is a detail of the temperature rise during heating, showing saturation at $k_B T \simeq 0.5$ eV.

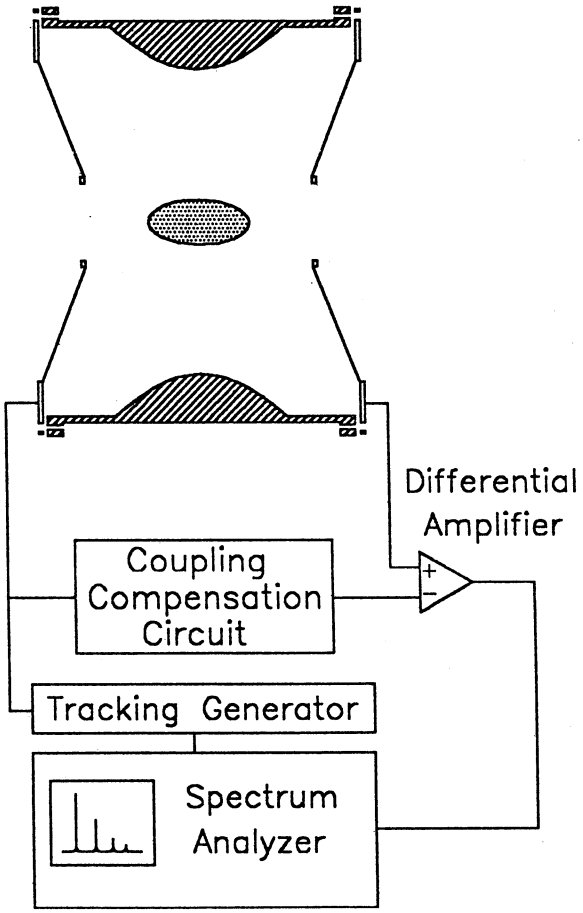

Figure 3.10: Electronics used for mode excitation and detection of axial modes of electron plasmas.

analyzer and tracking generator models are used for the two different experiments.

Chapter 4

Electron Plasmas

Plasma experiments in the positron trap began with the simple goal of remote detection and monitoring of trapped positrons in the original three-stage trap. This turned out to be surprisingly difficult because of the small numbers of positrons then available (3×10^5), various signal coupling problems, and an unexpected physical effect eventually ascribed to the anharmonic nature of the trap potential. In addition, the normal modes of large electron plasmas, though easily excited and detected, could not be accurately compared with theories for either cylindrical or spheroidal plasmas. This led to the design of the hyperboloidal electrode structure described in Sec. 3.2 and a substantial improvement in the data. Small numbers of positrons (about 10^4 or more) could be detected by exciting and detecting an oscillation of their center of mass about the center of the trap. The electron plasma mode frequencies were found to be much more stable, but were still not in quantitative agreement with the cold fluid theory for spheroidal plasmas [Eq. (2.27) and Fig. 2.2]. The discrepancy was discovered to be mainly the result of the finite plasma temperature. This effect has been studied in detail for the lowest order axial plasma mode, the quadrupole mode.

This chapter describes the electron plasma work, which was completed before

the construction of the azimuthally sectored electrodes used for the ion plasma experiments described in Ch. 5. It is anticipated that azimuthal modes in electron and positron plasmas will be of interest and eventual diagnostic use, but they have not yet been studied. In Sec. 4.1, the work in the original cylindrical trap is described. The remaining sections discuss the results obtained in the quadrupole trap (the hyperboloidal electrode structure), including a discussion of their use as diagnostics of plasma parameters and examples of recent data obtained with positron plasmas.

4.1 Cylindrical Trap

4.1.1 Electrostatics

As shown in Fig. 4.1, the electrodes of the third stage of the positron trap consist of three cylinders and a flat disk-shaped electrode with a hole in the center for particle access. The end cylinder is set to a potential V_1, the disk electrode is set to V_2, and the middle two cylinders are grounded. The plasmas studied are contained well within the long cylinder, so that the hole in the disk and the details of the geometry beyond the second short cylinder are not important. As a result, the basic features of the electrostatics of the trap can be determined analytically from the Green's function for a closed cylinder [*Jackson*, 1975] by placing a fictitious disk at the far end of the second short cylinder. Useful results that can be obtained include the location of the potential minimum and the expansion of the potential about the minimum [as in Eq. (2.34)], as functions of the potentials on the disk electrode and the short cylinders with respect to the long cylinder. The results are in good agreement with more laborious numerical solutions to Laplace's equation.

A simpler approach that gives very similar results uses only the dominant terms of the expansion for the trap potential obtained from the Green's function.

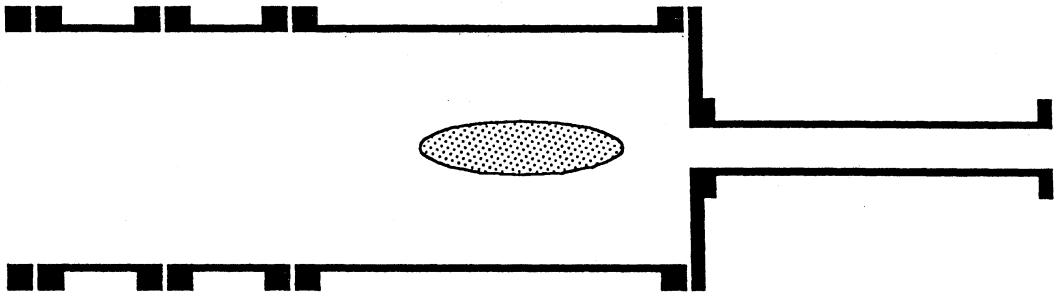

Figure 4.1: Electrodes of the third stage of the positron trap.

This gives the form

$$\Phi(\rho, z) \simeq J_0(x_{01}\rho/r_w)\left(V_1 c_1 e^{-x_{01}z/r_w} + V_2 c_2 e^{x_{01}z/r_w}\right), \tag{4.1}$$

where J_0 is a Bessel function, $x_{01} \simeq 2.4048$ is the first zero of $J_0(x)$, and c_1 and c_2 are constants. The exponentials are approximations to the hyperbolic sine functions present in the Green's function. Considering the potential along the axis ($\rho = 0$), we can easily find the position of the minimum,

$$z_c \simeq \frac{x_{01} r_w}{2} \ln(c_1 V_1 / c_2 V_2), \tag{4.2}$$

and the power series expansion of $\Phi(0, z)$ about the minimum, which is recognized as a hyperbolic cosine function, giving the result

$$\Phi(\rho, z) \simeq (c_1 c_2 V_1 V_2)^{1/2} J_0(x_{01}\rho/r_w) \cosh\left(\frac{x_{01} z}{r_w}\right). \tag{4.3}$$

The frequency of small oscillations about z_c is found to be

$$\omega_z(\rho) \simeq [J_0(x_{01}\rho/r_w)]^{1/2} \left(\frac{4q^2}{m^2 r_w^2 x_{01}^4} c_1 c_2 V_1 V_2\right)^{1/4}. \tag{4.4}$$

Equation (4.3) is a generic form for the potential near a minimum inside a long cylinder. Different geometries of the end electrodes, different cylinder lengths, and different choices for the location of $z = 0$ affect only the coefficients c_1 and c_2, as long as V_1 and V_2 are not so different that the potential minimum is close to one end of the cylinder. The insensitivity of z_c to V_1 and V_2 indicated by Eq. (4.2) is a problem if a center-of-mass oscillation is to be excited by oscillating V_1 and detected by signals induced on V_2. A more physical explanation is that external fields die out exponentially with distance inside a conducting cylinder, which is the essence of Eq. (4.1). The anharmonicity of the potential is easily found from the power series for the hyperbolic cosine. A distance scale must be chosen (for example, in

Eq. (2.34), coordinates are scaled by z_0), and the natural choice in this geometry is the radius of the cylinder wall, r_w. This results in

$$C_4 = x_{01}^2/12, \tag{4.5}$$

i.e., $C_4 \simeq 0.482$, for any long cylindrical trap. The positive sign of C_4 indicates that the potential well "stiffens" with increasing distance from the minimum.

4.1.2 Center-of-Mass Mode

For clouds of particles in which space charge effects are minor, the particles will collect about the axial potential minimum, with the radial distribution with which they are trapped. If their radial distribution is narrow and their temperature is low enough that they stay close to the minimum, the potential is approximately quadrupole, leading to small-amplitude harmonic oscillations at the frequency, $\omega_z(0)$, given in Eq. (4.4). A coherent excitation of all the particles produced by a sinusoidal signal applied to one of the short cylinders should result in the oscillation of their center of mass at the frequency $\omega_{\rm CM} = \omega_z$, which will produce a signal proportional to N on the disk electrode.

This simple result was never observed with the cylindrical electrodes. Instead, it was found that unexpectedly large numbers of particles were required to produce a detectable signal ($N \sim 10^7$), that this signal occurred at a frequency $\omega_{\rm CM} > \omega_z$, and that the amplitude of the signal was a very nonlinear function of N and of other uncontrolled variables. Figure 4.2 shows a typical dataset. Such large collections of particles are plasmas and elongate considerably due to their space charge, so it is reasonable that the signal coupling will improve and that the frequency may rise as the longer plasmas feel the trap anharmonicity more strongly.

What is surprising is that there is a threshold behavior to the response, such

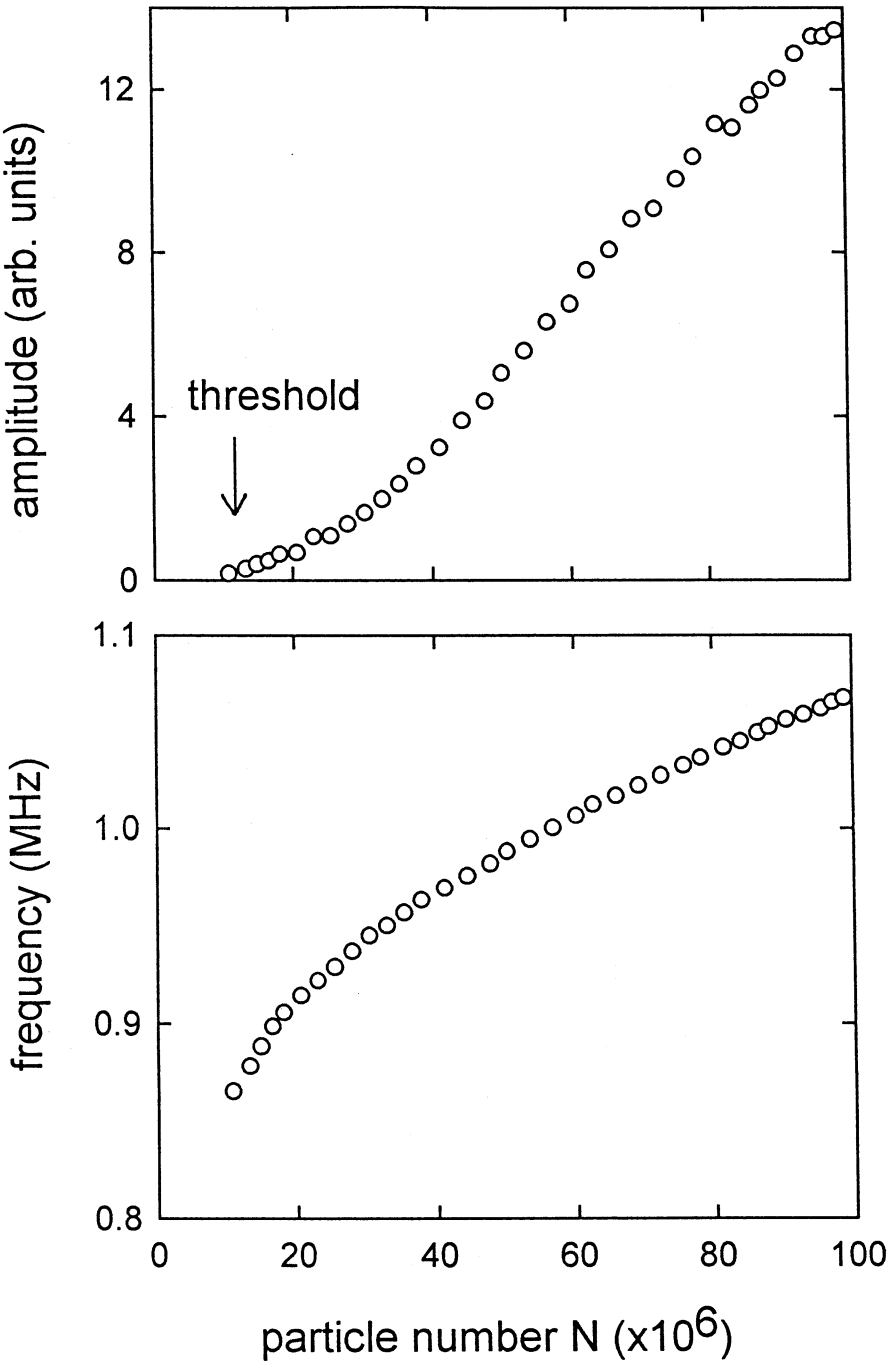

Figure 4.2: Dependence of (a) amplitude and (b) frequency of the axial center-of-mass oscillation on the number of particles in the cylindrical trap.

that the response detected for ($N \sim 10^7$) is relatively strong, but a 20% reduction in N below this results in a very small signal. A more telling result is that this threshold may also be crossed by varying the temperature, as demonstrated in Fig. 4.3, where the response spectrum of 10^7 electrons is monitored as the plasma cools after a rapid fill. The response as a function of temperature for this dataset is shown in Fig. 4.4, which also shows the results for a plasma with half as many particles.

Because such an effect cannot easily be explained in a pure quadrupole potential, the trap anharmonicity appears to be a contributing factor. The dependences on T and N (which implies a dependence on n) could both be explained by the existence of a threshold value of the Debye length. It may be that the typical radial particle distribution, which is approximately Gaussian with an rms radius of about 1 cm, is wide enough to cause substantial phase-mixing of the signals from particles at different radii because of the radial variation in ω_z indicated in Eq. (4.4) and in Fig. 3.5(a). Even particles at the same radius will have a distribution of bounce periods due to anharmonicity and the thermal distribution of amplitudes of oscillation, as shown in Fig. 3.5(b). A charge cloud with sufficient plasma character (i.e., one with $\lambda_D < \lambda_{\text{threshold}}$) would tend to move collectively and might avoid these damping mechanisms.

4.1.3 Plasmas

In spite of the difficulty of detecting small numbers of particles in the cylindrical trap, there is no trouble exciting and detecting various normal modes of large plasmas. A typical response spectrum, shown in Fig. 4.5, presents a family of resonances of increasing frequency excited by a sinusoidal signal applied to one of the confining electrodes (see Fig. 3.10). Density profiles of the plasmas, obtained by applying the Poisson solution program to charge collector data (as described in

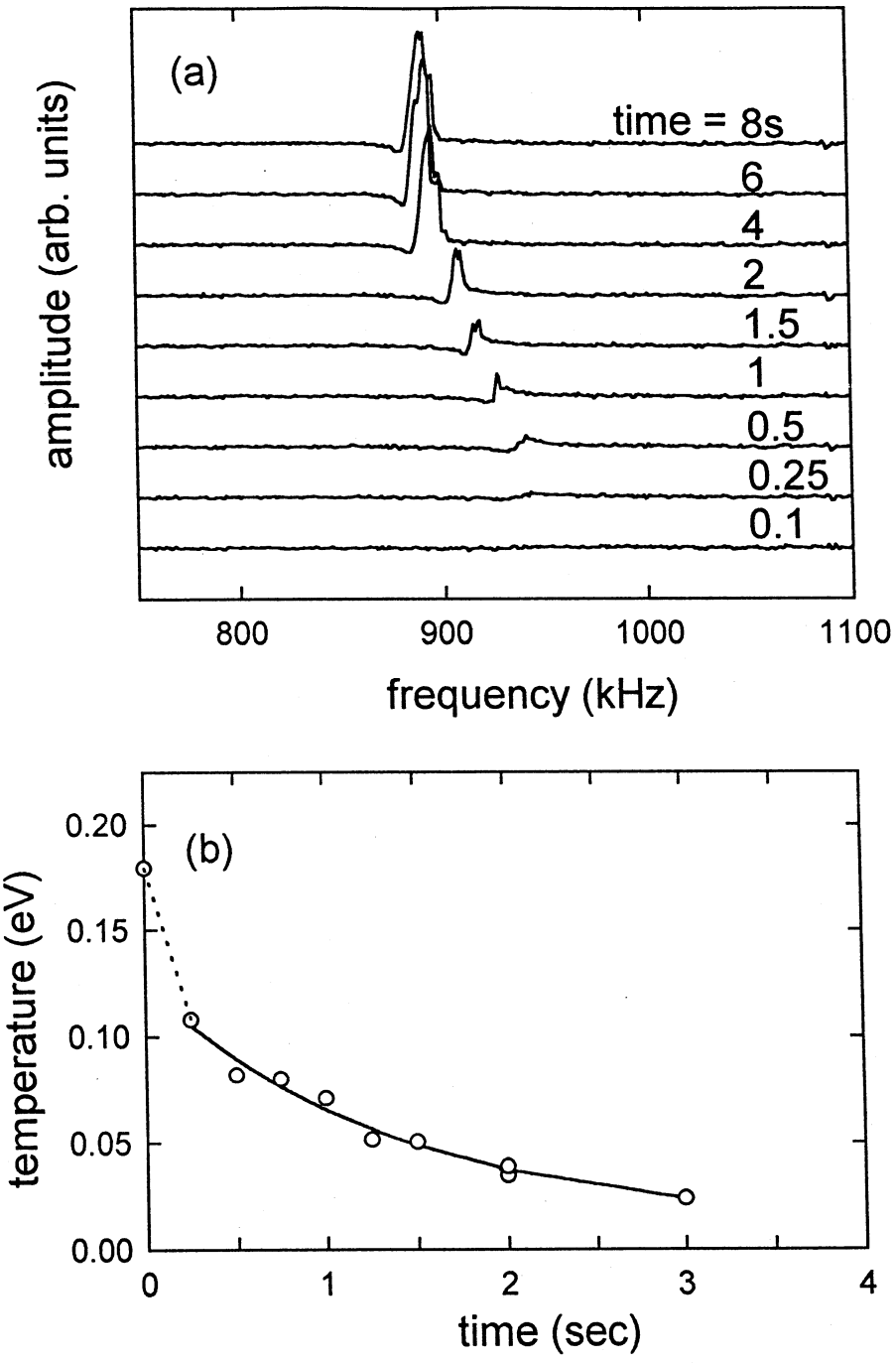

Figure 4.3: (a) Center-of-mass response spectra of about 10^7 electrons in the cylindrical trap at varying times after a rapid fill, offset vertically for clarity. (b) Cooling curve measured under the same conditions.

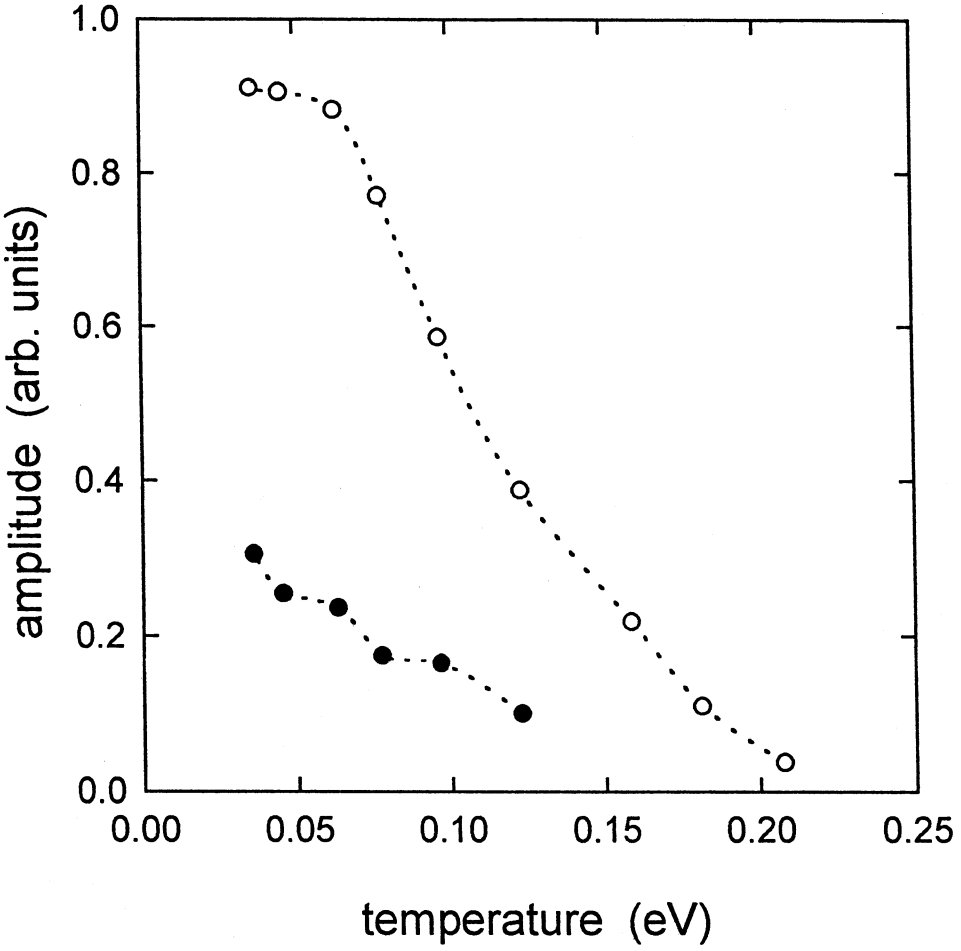

Figure 4.4: Amplitude of center-of-mass response vs. temperature. (o): for the data in Fig. 4.3, and (•): for half as many particles.

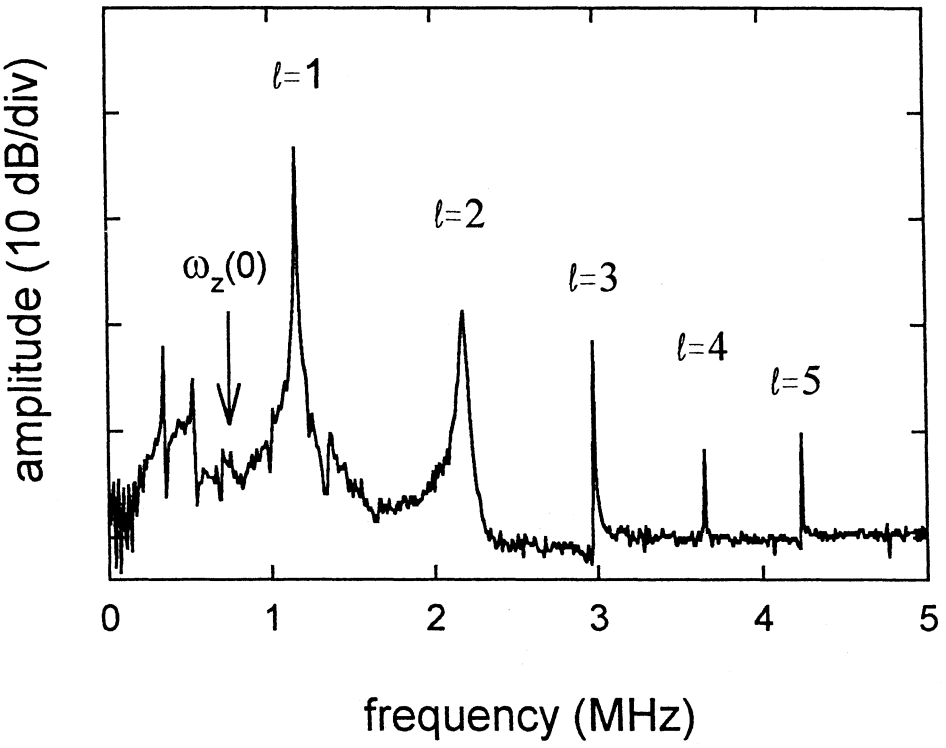

Figure 4.5: Spectrum of a plasma of about 2×10^8 electrons in the cylindrical trap. Values of l refer to the mode theory for spheroids (Eq. (2.27)). $\omega_z(0) \simeq 750$ kHz.

Sec. 3.3), appear roughly spheroidal, so an attempt was made to analyze the data using the spheroidal mode theory [Eq. (2.27) and Fig. 2.2]. A strong response was expected at the value of $\omega_z(0)$ predicted by Eq. (4.4). As mentioned in the preceding section, the strongest response consistently occurred at a substantially higher frequency, but by decreasing N it was possible to track the mode frequency close enough to $\omega_z(0)$ to be confident of its identification as the $(l = 1)$ center-of-mass oscillation. The higher-frequency series of modes were thus suspected to be the $l = 2, 3, 4, ...$ axial modes predicted by the theory. Somewhat less confidently, the two weaker resonances seen at frequencies below $\omega_z(0)$ were suspected to be the $l = 3$ and $l = 4$ modes with radial structure indicated in Fig. 2.2 and Fig. 2.3.

To test the dependence of the mode frequencies on aspect ratio, two similar plasmas with different aspect ratios were obtained by filling them under identical conditions and then reducing B in one case to expand the plasma radially. The frequencies of the most prominent modes observed in each case are plotted in Fig. 4.6. The value of ω_{CM} was different for the two plasmas and was not close to $\omega_z(0)$ in either case, so the mode theory will clearly not be satisfied to any degree of precision. It was hoped that by scaling the frequencies by the measured values of ω_{CM} rather than by $\omega_z(0)$, we might roughly account for these differences. Frequencies predicted by the theory for four different aspect ratios are also shown in Fig. 4.6, connected by lines to distinguish them from the data points. Neither plasma shows a dependence of mode frequency on mode number, l, that accurately matches the theory for its measured α. Still, the general appearance seems qualitatively correct.

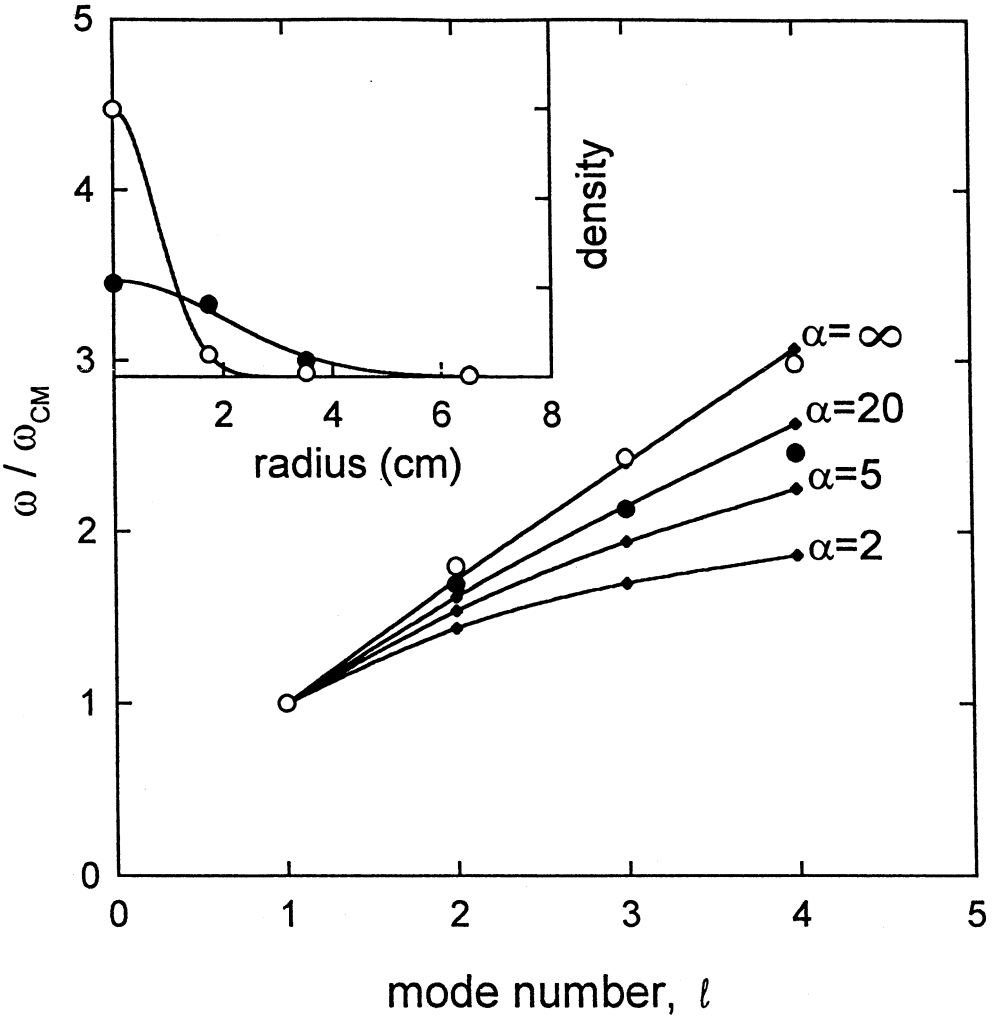

Figure 4.6: Comparison of the frequencies of 4 modes observed in the cylindrical trap with spheroidal mode theory. Two plasmas with different aspect ratios were studied: (o): $\alpha \sim 20$, and (•): $\alpha \sim 5$. Inset: radial density profiles of the plasmas.

4.2 Quadrupole Trap

4.2.1 Center-of-Mass Mode

In the quadrupole trap, the nonlinear behavior of the axial center-of-mass mode seen in the cylindrical trap is absent. When the data from Fig. 4.3 is retaken in the quadrupole trap, the amplitude and frequency of oscillation appear to be independent of the plasma temperature, as shown in Fig. 4.7, in strong contrast to Fig. 4.3. Because of the increased sensitivity, it is possible to track the amplitude of the response across the range of N over which the transition to a plasma should occur. As shown in Fig. 4.8, the response is proportional to N for $N < 6 \times 10^6$ and no threshold is seen.

The dependence of ω_{CM} on N can be adjusted to some extent by varying the quadrupole trap potentials relative to the rest of the trap. With the quadrupole electrodes located inside the (grounded) dewar, as shown in Fig. 3.1, this involves adding a fixed potential to the voltage on each electrode. If the quadrupole trap is placed inside the cylindrical trap, as originally intended, the potentials of the cylindrical trap may be varied to tune the anharmonicity. Data taken in the latter fashion are shown in Fig. 4.9, in which curves of $\omega_{CM}(N)$ are taken for various values of the external potentials. The most obvious features are that it is possible to tune the anharmonicity to make ω_{CM} independent of N for $N < 10^7$, but that for much higher N, ω_{CM} rises regardless of the anharmonicity.

The remainder of the data in this chapter were taken with the anharmonicity adjusted to minimize the variation of ω_{CM} with N, even though this did not occur at the expected values of the external potentials. We now believe that rather than nulling C_4, this procedure adjusted it to balance the initial effect of the increasing image charge.

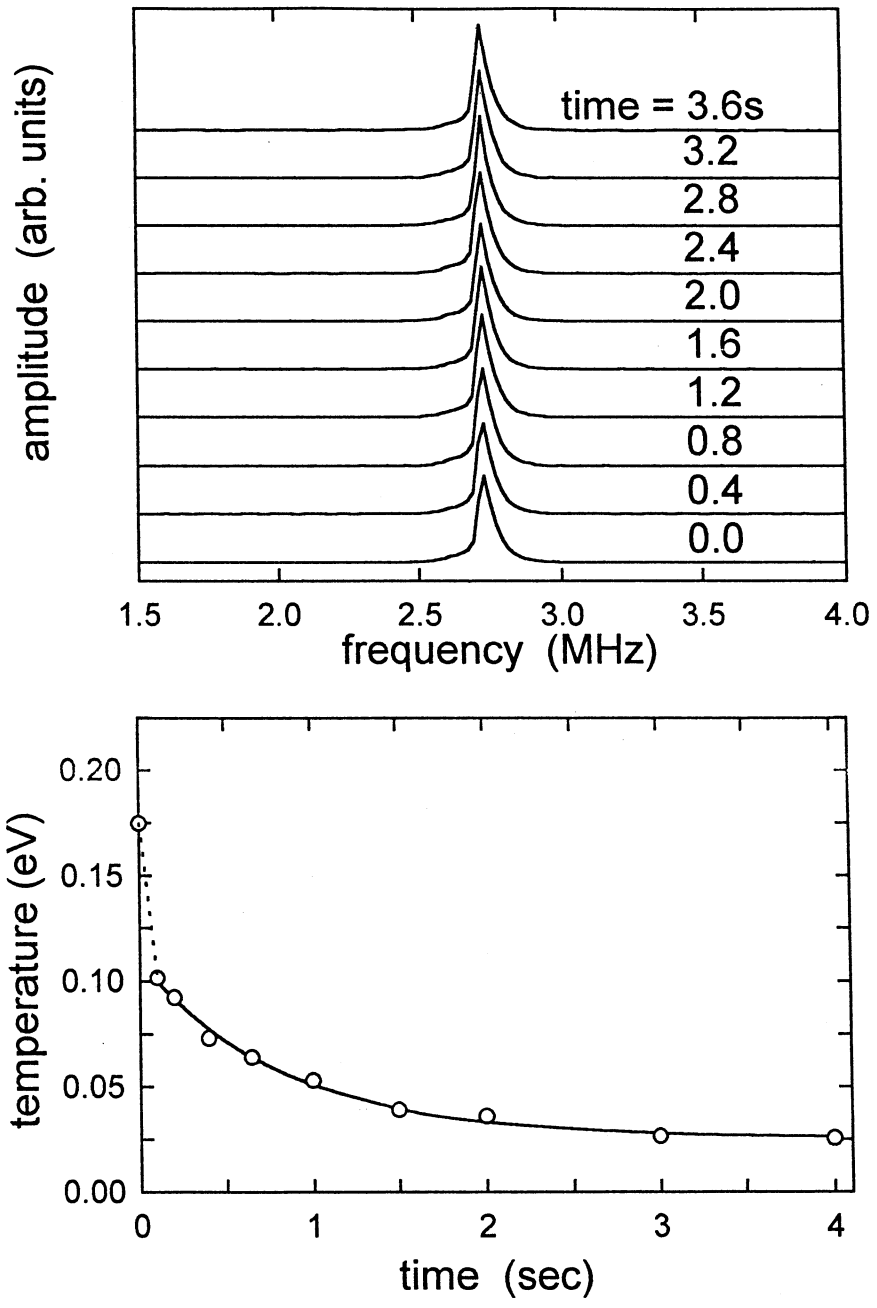

Figure 4.7: (a) Center-of-mass response spectra of about 10^7 electrons in the quadrupole trap at varying times after a rapid fill, offset vertically for clarity. (b) Cooling curve measured under the same conditions.

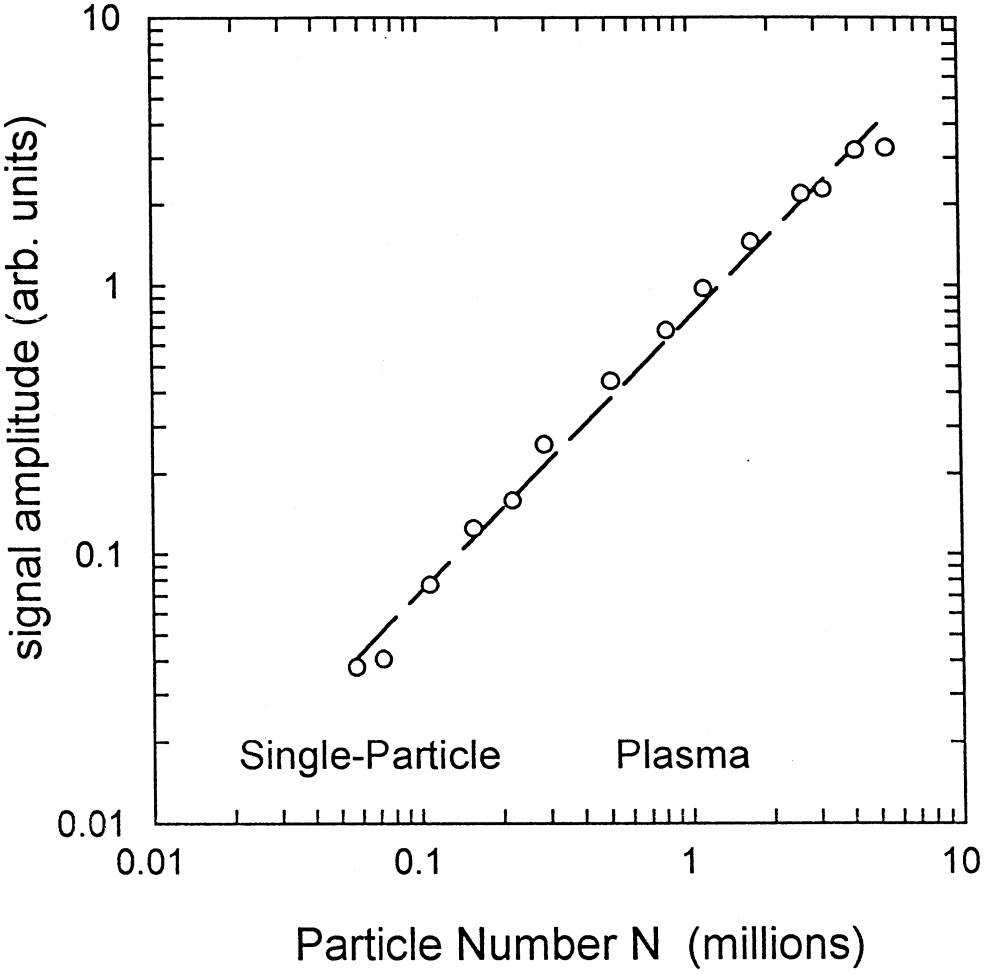

Figure 4.8: Amplitude of center-of-mass response in quadrupole trap as a function of N.

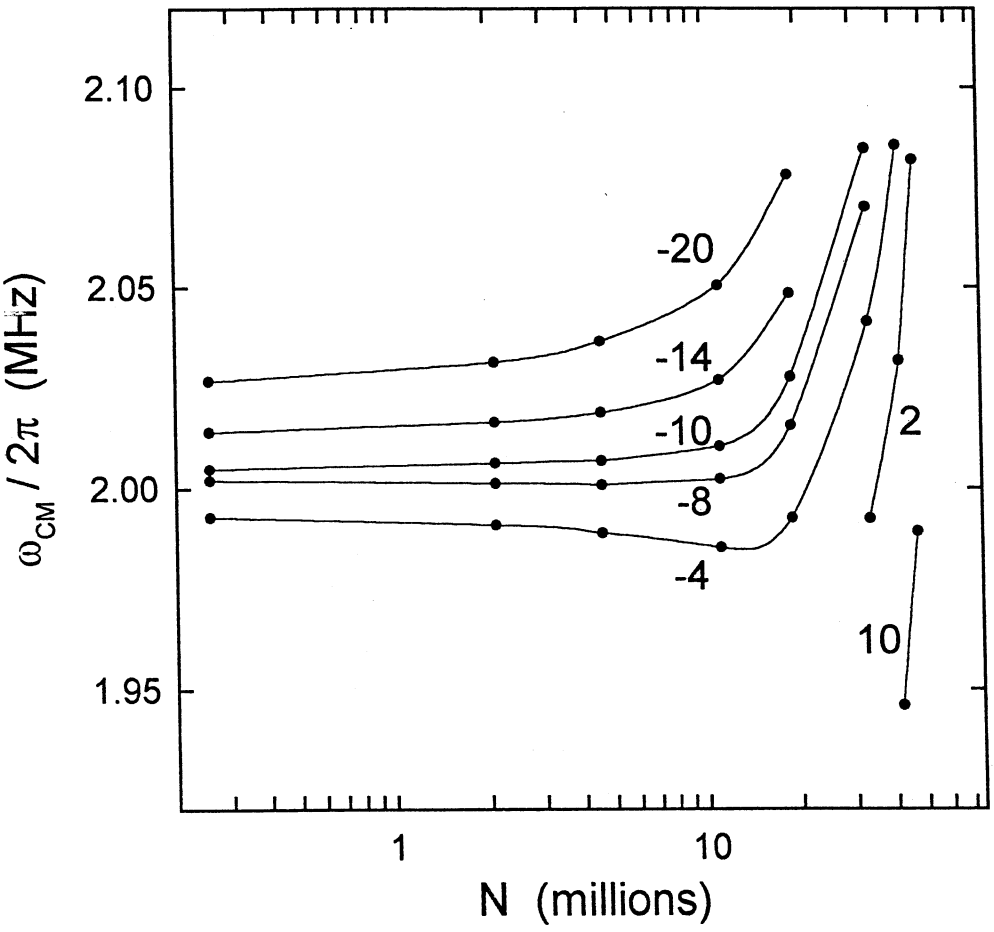

Figure 4.9: Dependence of center-of-mass frequency on N in the quadrupole trap for $V_{\text{ring}} = 3.2$ volts, $V_{\text{endcaps}} = 0$ volts and the various external potentials indicated on the figure.

4.2.2 Plasmas

Axial plasma modes are easily excited and detected in the quadrupole trap. A typical spectrum has strong $l = 1$ and $l = 2$ peaks and sometimes either a weak $l = 3$ peak or one or two weak low-frequency modes. The spectrum shown in Fig. 4.10 is atypical, having been obtained with a large, wide plasma, and it shows two prominent low-frequency modes. Even the more typical spectra taken in the quadrupole trap have significant qualitative differences from the spectra (such as Fig. 4.5) obtained in the cylindrical trap. The signal-to-noise ratio is greatly improved by the superior signal coupling, but fewer of the purely axial modes are detected, probably because of the different plasma shapes studied in the two traps. The geometry of the hyperboloidal trap enforces the restriction $L < 2z_0$ on the plasma length. Because of the condition $\lambda_D \ll \lambda$ for undamped plasma modes, discussed in Sec. 2.3, fewer axial modes are expected for a short plasma. This is the only disadvantage that we have found to using the quadrupole trap.

4.3 Temperature Dependence of Quadrupole Mode

With the most obvious problems of the cylindrical trap eliminated, it was found that the mode frequencies still did not match the cold fluid theory. The technique described previously of reducing B to obtain similar plasmas with different aspect ratios was used to measure the dependence of the quadrupole ($l = 2$) mode frequency on α. In Fig. 4.11, the results are compared with the theoretical curves for the $l = 2$ and $l = 3$ modes. It is no longer necessary to divide by a value of ω_{CM} that is significantly different from ω_z, but with this excuse removed, the remaining disagreement is substantial.

Much of this difference is caused by the nonzero temperature of the plasma.

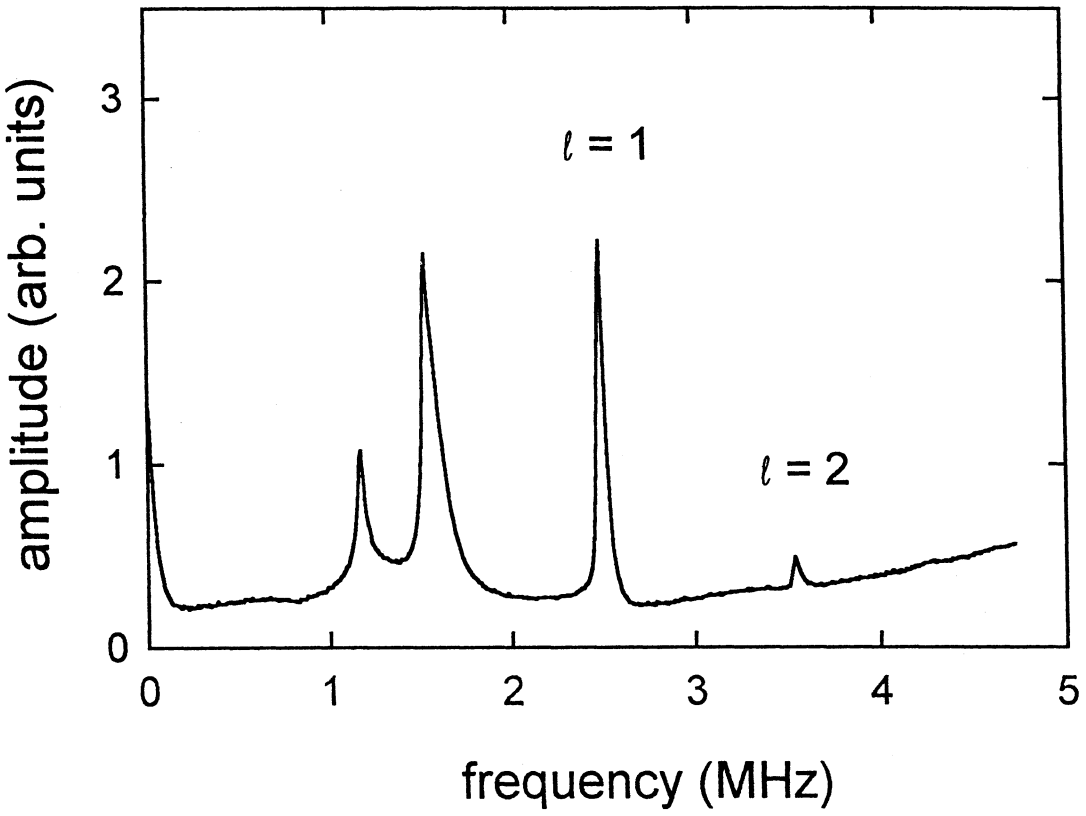

Figure 4.10: Spectrum of a wide electron plasma with $N \sim 10^8$ in the quadrupole trap.

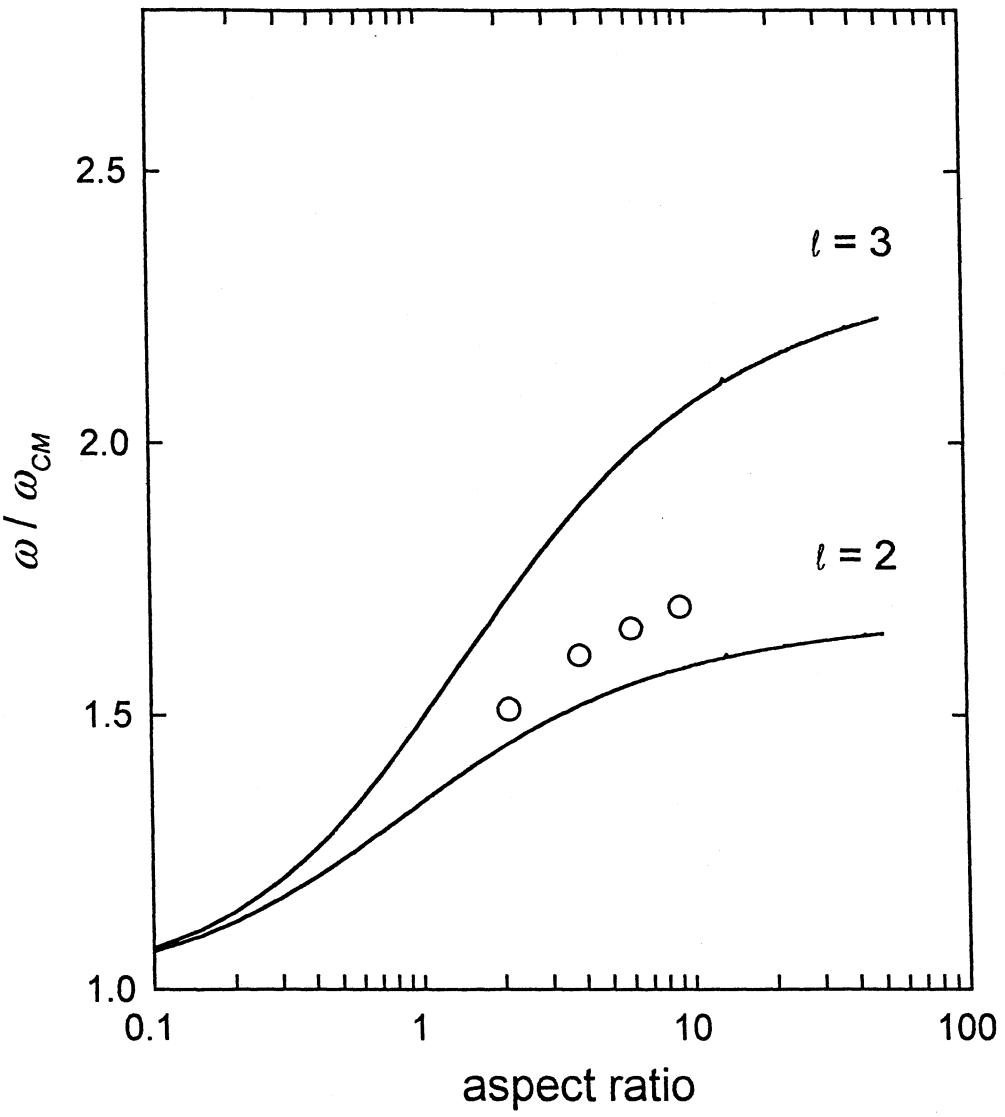

Figure 4.11: Comparison of measured frequency (o) of the quadrupole mode ($l = 2$) in the quadrupole (hyperboloidal) trap with the cold fluid theory (solid curves) for $l = 2$ and $l = 3$.

Figure 4.12(b) plots the frequency of the quadrupole mode measured at various times during a cycle of rf heating and cooling, with the plasma temperature shown in Fig.4.12(a). Figure 4.13 shows the quadrupole mode frequency as a function of temperature for three plasmas with different aspect ratios. The radial profiles are shown in the inset. When the data are extrapolated to $T = 0$, frequencies within about 1% of the cold fluid predictions for the quadrupole mode are obtained, confirming our identification of the mode.

The cold fluid theory assumes a cold plasma of uniform density in an exactly quadratic potential imposed by distant electrodes. To model effects not included in the cold fluid theory, R. L. Spencer and G. W. Mason of Brigham Young University performed numerical simulations of the plasmas. The electrode voltages and z-integrated density profiles of experimentally measured plasmas were used as input to a Poisson-Boltzman equilibrium code. The resulting equilibria, from which the plasma aspect ratios were obtained, were constrained to match the experimental density profiles and the total particle number. The computations were done assuming axisymmetry and used a 120 by 240 grid for the coordinates ρ and z.

The computed equilibria were then used to create initial distributions for particle-in-cell simulations which used the same spatial grid and electrode representation as the equilibrium computation. The center-of-mass and quadrupole modes were excited by displacing all of the particles by a small amount in the same direction in z and also by stretching the plasma along the z axis. The position of the center of mass, $z_{\rm cm}$, and the density-average of the square of the position of the plasma relative to the center of mass, $\langle (z - z_{\rm cm})^2 \rangle$, were then tracked in time and Fourier-analyzed to yield the frequencies of the center-of-mass and quadrupole modes, respectively. The plasma was represented by 50,000 particles, which were advanced through 16,384 time steps of 4×10^{-9} s each.

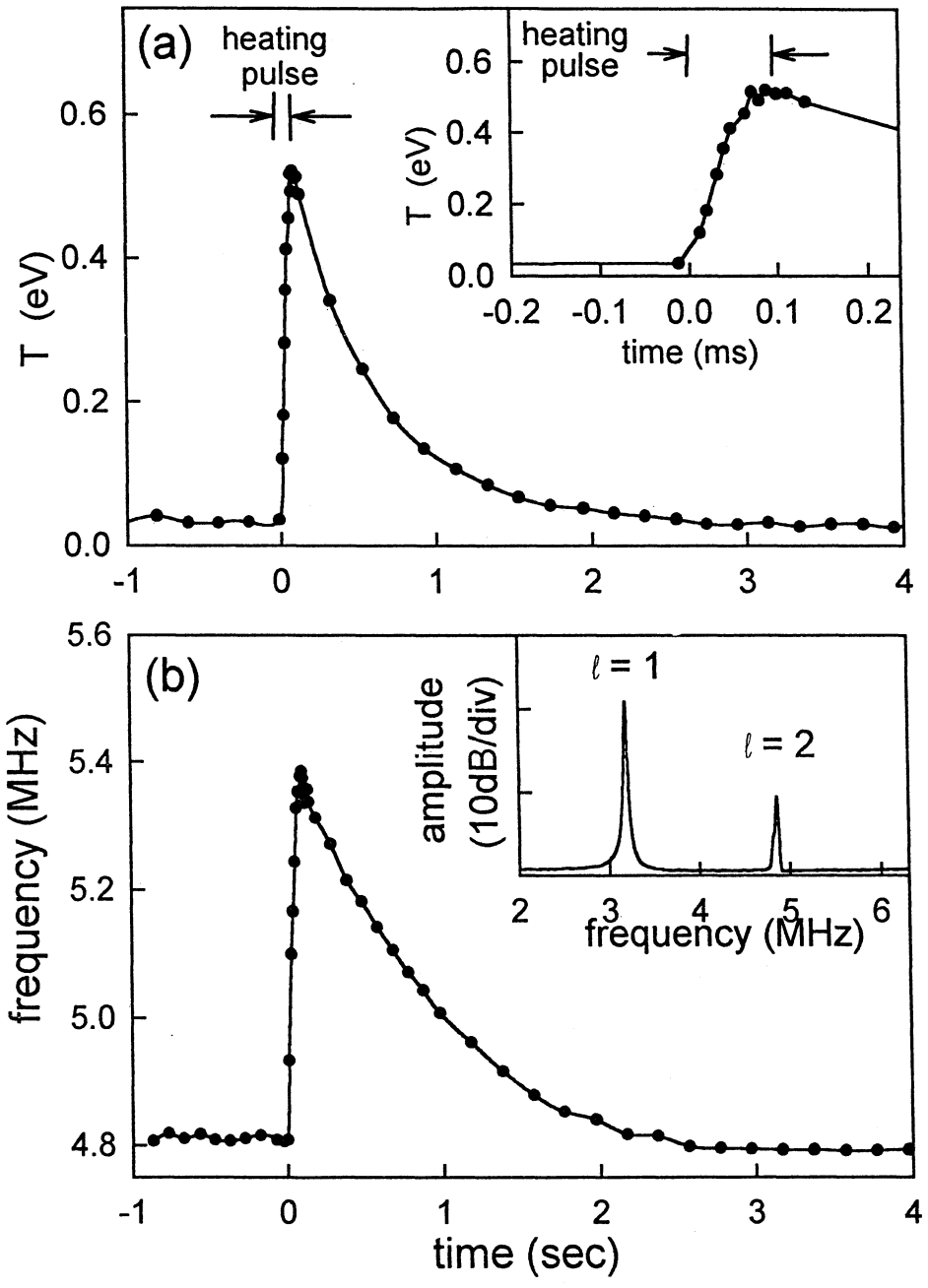

Figure 4.12: (a) Temperature during a cycle of heating and cooling. (b) Variation of quadrupole mode frequency. Inset: spectrum of unheated plasma.

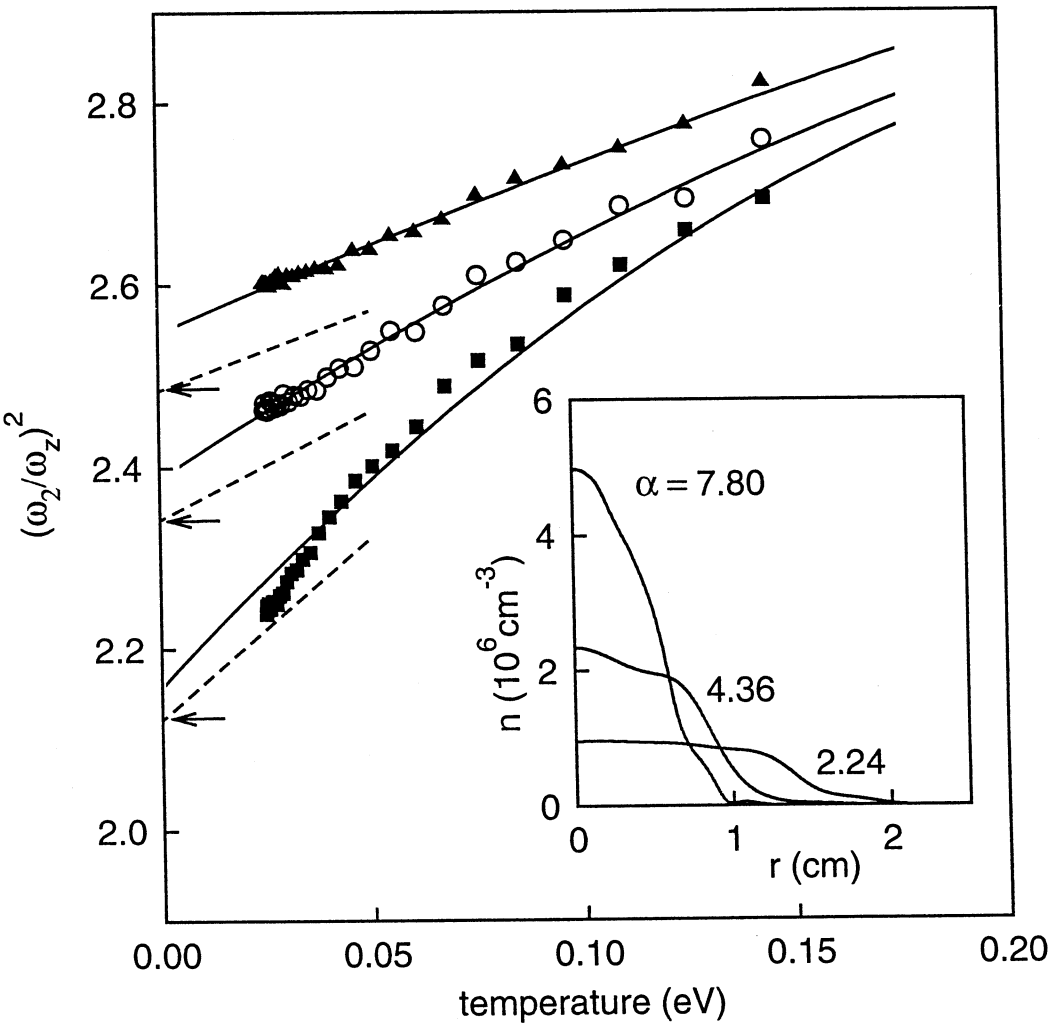

Figure 4.13: Temperature dependence of the quadrupole mode frequency for plasmas with different shapes: (□), $\alpha = 2.24$, $L = 6.20$ cm; (○), $\alpha = 4.38$, $L = 7.52$ cm; and (△), $\alpha = 7.80$, $L = 8.32$ cm. Solid lines are the results of numerical simulations of the plasmas. Arrows on the vertical axis show the cold fluid theory predictions; dashed lines are from Eq. (4.6). Inset: radial profiles of the plasmas.

The experimentally measured plasmas shown in Fig. 4.13 were studied using these simulation techniques. From the Poisson-Boltzmann code, the aspect ratios were found to be 7.80, 4.38 and 2.24. For each aspect ratio, simulations were made for ten temperatures in the range 0.001 - 0.176 eV. The frequency ratio between the quadrupole and center-of-mass modes shown by the solid lines in Fig. 4.13 is in excellent agreement with the data. The simulation frequencies at the lowest temperatures agree well with the predictions of Dubin's cold fluid theory, which are marked with arrows on the ordinate of Fig. 4.13. This is interesting in view of the fact that the density profiles shown in the inset to Fig. 4.13 differ substantially from the nearly uniform density expected for a plasma in global thermal equilibrium (and assumed by the cold fluid theory). The insensitivity of the mode frequencies to the plasma profile simplifies their use as diagnostics, as discussed in Sec.4.4.

An approximate analytical treatment of temperature effects on the quadrupole mode frequency was proposed recently by Dubin [1993]. This model leads to a prediction of a shift in the quadrupole mode frequency from the cold fluid result ω_2^c to ω_2 [*Dubin*, 1994]:

$$(\omega_2)^2 = (\omega_2^c)^2 + 20\,[\gamma - g(\alpha)]\,\frac{k_B T}{mL^2}, \tag{4.6}$$

with

$$g(\alpha) = \frac{\alpha^2}{2}\frac{\omega_p^2}{(\omega_2^c)^2}\frac{\partial^2 A_3}{\partial \alpha^2}, \tag{4.7}$$

where $A_3(\alpha)$ is defined in Eq. (2.11) and $\gamma = 3$ is the ratio of specific heats for one-dimensional expansions. All quantities on the right-hand sides of Eq. (4.6) and Eq. (4.7) are evaluated in the cold fluid limit. The function $g(\alpha)$ describes the frequency shift from the temperature-dependence of the plasma shape. If this term is neglected, one obtains a result similar to the Bohm-Gross dispersion relation for a warm neutral plasma, $\omega^2 = \omega_p^2 + \gamma k_z^2 k_B T/m$, with $k_z \simeq \pi(l-1)/L$. The two results

agree reasonably well for the temperature-dependent frequency shift, but the cold plasma limits are very different because the Bohm-Gross formula does not account for the finite plasma geometry.

The data shown in Fig. 4.13 indicate that $(\omega_2)^2$ is linear in T for the longer plasmas studied, but deviates from linearity for the shortest plasma, for which the temperature-dependence is strongest. For the same value of T and the same mode, the effect of temperature is stronger for shorter plasmas because the wavelength of the mode is smaller, making the effective temperature higher. The slopes of the curves at low temperatures agree reasonably well with the predictions of Eq. (4.6), which are plotted as dashed lines in Fig. 4.13.

4.4 Diagnostic Applications

For positron and positron-electron plasmas, non-destructive diagnostics are essential, and the measurement of the frequencies of plasma modes is an attractive way of accomplishing this, because frequencies can be measured with great precision. The modes studied are global, and thus they provide information on global plasma parameters. For the purposes of mode studies, the spatial distribution is adequately parametrized by the length, L, and aspect ratio, α, since the mode frequencies are relatively insensitive to details of the radial density profile. Therefore, the cold fluid equilibrium theory for a uniform-density spheroid [Eq. (2.10)] may be used to relate the parameters N, α, and L:

$$L^3 = \frac{12e^2}{m\omega_z^2}\alpha^2 A_3(\alpha)N. \tag{4.8}$$

Thus, a measurement of N fixes a relationship between L and α. Measurement of two plasma modes combined with the results of simulations or warm fluid theory would provide the additional relationships to uniquely determine L, α, and T, and

hence also the plasma radius and density. If the temperature is known, as it is in the presence of a buffer gas, then with N determined from the amplitude of the center-of-mass response, Eq. (4.6) and Eq. (4.8) may be used to determine L and α from the quadrupole mode frequency. Once the plasma parameters are established, whether by these techniques or by other diagnostics, subsequent changes in either temperature or shape may be deduced from additional shifts in a single mode frequency, as in the data for ω_2 during a heating pulse, shown in Fig. 4.12(a). Alternatively, if the temperature can be controlled, the plasma length and aspect ratio may be found from the slope and intercept of data for $(\omega_2)^2$ vs. T. Applying this technique to the data in Fig. 4.13, we obtain lengths of 8.5 cm, 7.3 cm, and 5.3 cm for the three plasmas, while the experimental values are 8.3 cm, 7.5 cm, and 6.2 cm, respectively.

The use of data from modes other than the quadrupole mode would benefit greatly from a complete theory of finite-temperature spheroidal plasmas. Modes with azimuthal structure, such as the $l = 2$, $m = 2$, diocotron mode have frequencies that depend on aspect ratio [*Dubin*, 1991; *Dubin and Schiffer*, 1994] and could provide the data needed for complete determination of the bulk plasma parameters, if their temperature-dependence were understood.

4.5 Positrons

All of the preceding data were obtained using electrons. At the time of the early work in the cylindrical trap, the largest positron plasmas consisted of about 10^6 positrons, and due to the anomalous damping and the poor sensitivity of the cylindrical trap, even their center-of-mass motion could not be detected. With the construction of the quadrupole trap, the sensitivity improved and the anomalous damping vanished, permitting the detection of the center-of-mass motion

of as few as 10^4 positrons, but no plasma modes were seen. The development of a diagnostic based on plasma modes proceeded with electron plasmas, in the hope that comparable positron plasmas would eventually be achieved.

Improvements in positron trapping efficiency and the recent upgrade to a more efficient positron moderator have now produced plasmas of 10^8 positrons, larger than many of the electron plasmas used for the mode studies described above. Figure 4.14 is a mode spectrum obtained for such a positron plasma. Strong signals are seen for the center-of-mass oscillation and for the $l = 2$ and $l = 3$ axial plasma modes. A small peak at higher frequency may represent the $l = 4$ mode, or may be noise. This spectrum was obtained for a plasma confined in the cylindrical trap, where the positron trapping efficiency is highest. As with the electron plasmas, fewer modes are observed in the quadrupole trap, but the quadrupole mode is seen.

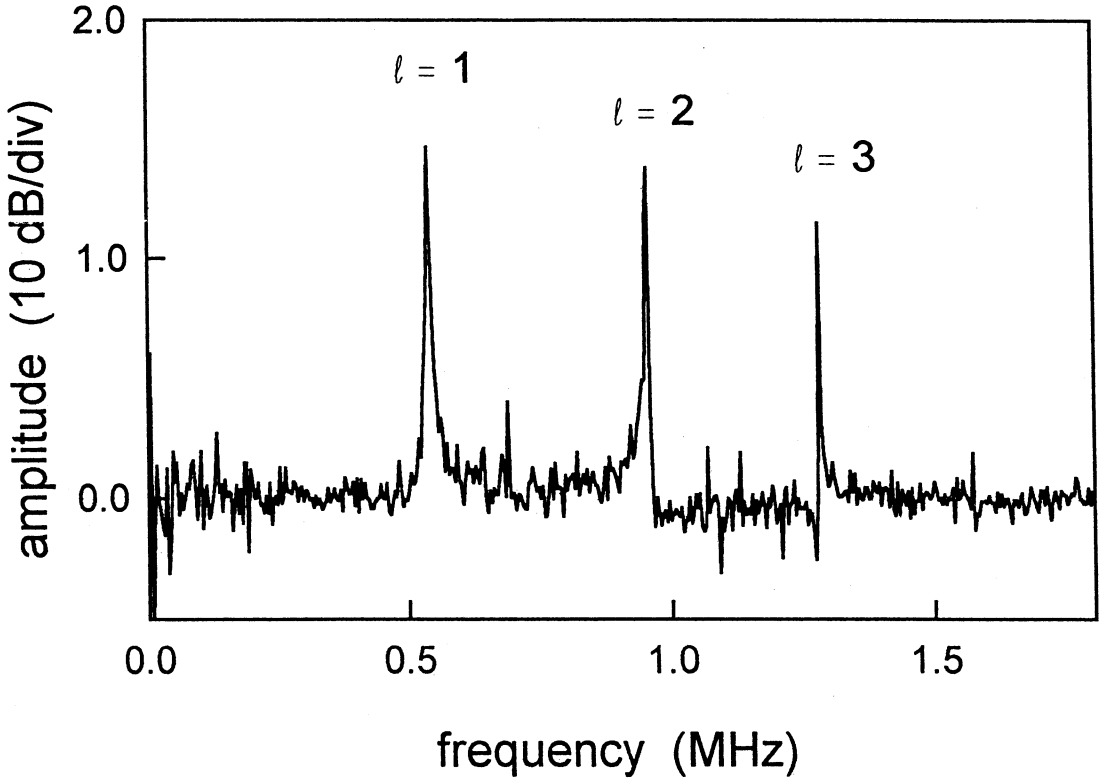

Figure 4.14: Spectrum of a positron plasma in the cylindrical trap. $N = 6 \times 10^7$.

Chapter 5

Ion Plasmas

One of the motivations for constructing a ring electrode split into azimuthal sectors was to determine the masses of the ions produced by positron annihilation [*Passner et al.*, 1989; *Glish et al.*, 1994] by measuring their cyclotron frequency, the method used in some commercial mass spectrometers. To test the technique, ions of a known species were produced by ionizing atoms of a low-pressure gas using an electron beam. It was quickly discovered that under typical conditions enough ions were produced to form a plasma, a circumstance assiduously avoided in spectrometry because of the variety of collective effects that result. In fact, in the approximately 1-kG magnetic field of this trap, the plasmas often reach the Brillouin limit, the maximum possible density.

This chapter describes the conditions under which this maximum density is attained and presents a simple model for the plasmas produced by continuous ion production. Because of the unmagnetized nature of Brillouin-density plasma, the standard diagnostics used for electron plasmas are less useful, and two different techniques are employed to verify that spheroidal ion plasmas at the maximal density are produced. Finally, azimuthal modes of the plasmas are studied over a range of plasma aspect ratios. The frequencies of the various cyclotron and diocotron

modes seen are found to agree quantitatively with the cold fluid mode theory of D. H. E. Dubin [1991].

5.1 Ion Production

Ions are formed by passing an electron beam along the axis of the trap, as shown schematically in Fig. 5.1. The rate at which ions are formed inside the trap is approximately

$$\frac{dN_{\rm ion}}{dt} \simeq 2z_0 n_n \sigma_i I_{\rm beam}/e, \tag{5.1}$$

where σ_i is the ionization cross-section, n_n is the density of neutral gas atoms, $I_{\rm beam}$ is the beam current, and $2z_0$ is the distance between the endcaps along the trap axis. This ignores the variation of the beam energy inside the trap, which could be included by using an averaged value of σ_i. Ionization cross-sections typically rise rapidly as the beam energy is increased above the first ionization threshold, $E_{\rm I}$, and reach a maximum value, $\sigma_{\rm max}$, at a beam energy on the order of 100 eV. For argon, $E_{\rm I} = 15.8$ eV and $\sigma_{\rm max} \simeq 4 \times 10^{-16}$ cm^2 occurs at a beam energy of 90 eV. The maximum is rather broad, so that a typical ion production rate for argon is obtained by assuming $\sigma_i \simeq \sigma_{\rm max}$:

$$\frac{dN_{\rm Ar^+}}{dt} \simeq 1.1 \times 10^9 {\rm s}^{-1} \cdot p I_{\rm beam}, \tag{5.2}$$

where the beam current is expressed in microamps and the gas pressure, p, is in microtorr.

The electron beam is emitted from the circular oxide-coated cathode of an electron gun with radius $r_g = 0.7$ cm in a magnetic field $B_g = 150$ G. Its radius as it passes through the trap will depend on the trap magnetic field:

$$r_{\rm beam} = r_g \sqrt{B_g/B}. \tag{5.3}$$

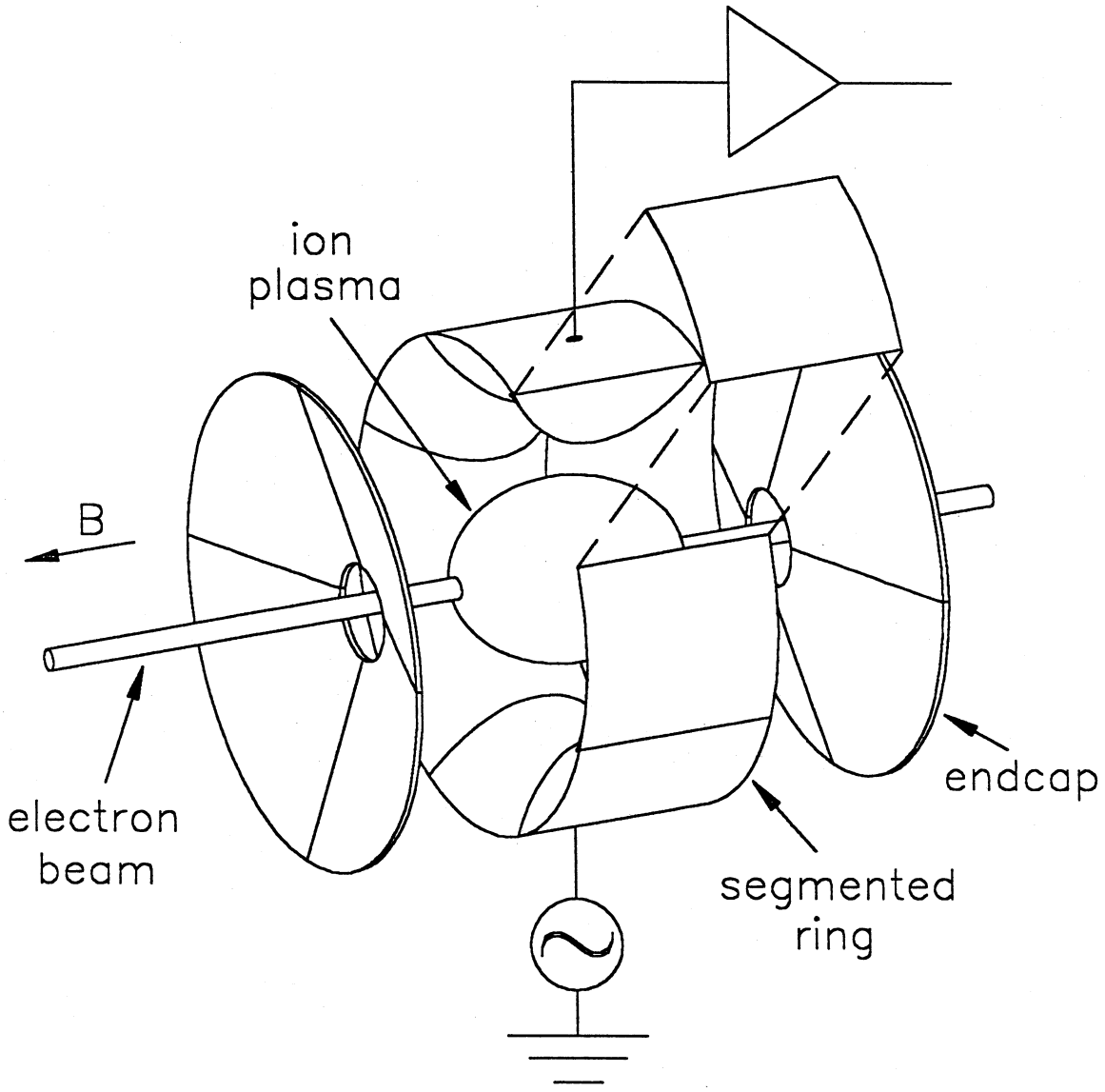

Figure 5.1: Exploded schematic of the ion plasma experiment, showing the electron beam, the spheroidal ion plasma, and the electronics used for mode excitation and detection.

Thus the density of ion production is

$$\frac{dn}{dt} \simeq \frac{dN_{\rm ion}}{dt}\frac{B}{2\pi r_g^2 z_0 B_g}, \tag{5.4}$$

or about 3.8×10^8 cm^{-3}s^{-1} for a one microamp beam passing through 10^{-6} torr of argon in a magnetic field of one kiloGauss.

As with other sources of pure ion plasmas, production of doubly ionized particles is a concern. Again taking the example of argon, above the second ionization threshold energy, $E_{\rm II} = 43.4$ eV, Ar^{++} ions are formed from gas atoms with a cross-section that reaches its maximum value, 3×10^{-17} cm^2, at an energy of 120 eV. If the beam energy is less than $E_{\rm II}$ throughout the trap, production of Ar^{++} ions will be avoided. If this precaution is not taken, a small amount of the doubly charged species will be produced. This is common in mass spectrometers, as for example in Residual Gas Analyzers, which typically produce ions using a 70 eV electron beam, and is not important for some experiments. In some work with pure ion plasmas [*Sarid et al.*, 1993; *Sarid et al.*, 1994], however, the impurity species produces significant complications. By dumping steady-state plasmas and measuring the time-of-flight spectrum, we have found that if the beam energy is substantially higher than $E_{\rm II}$ and $V > V_t$, the plasma consists predominantly of doubly ionized particles, which are preferentially confined. If $V < V_t$, the plasma is mostly singly charged particles. This change in character can easily be confused with another interesting phenomenon, which will be described below. To avoid these complications, the beam energy is kept below $E_{\rm II}$.

The temperature of the ions is difficult to establish experimentally, due to the failure of the charge-dumping procedure (see Sec. 5.3) upon which the magnetic beach temperature analyzer depends. The energy imparted to a gas atom during an ionizing collision with an electron is small, so that the initial ion energy distribution

will range from 0 to qV, due to the quadrupole trap potential. Once significant space charge has accumulated and flattened the potential well, ions will be formed with a narrower range of energies. Collisions of ions with neutrals are expected to be mostly charge-exchange collisions, in which the ion removes an electron from a neutral with very little exchange of kinetic energy. The original ions are thus replaced by ions with the room-temperature energy distribution of the neutral gas. This strong cooling mechanism may be one reason that the frequencies of the azimuthal modes described in Sec. 5.5 are in good agreement with the cold fluid theory. The mean free path for charge-exchange of 10-eV Ar^+ ions in 1 μtorr of Ar is $\sim 7 \times 10^3$ cm [*Brown*, 1959], so that the mean time between collisions is of the order of 10 ms. This is fast compared to the confinement time for a single particle, but it is not clear how it compares to the confinement time of particles in the unusual plasmas described in the following section.

5.2 Steady-state Plasma Model

The Brillouin density [Eq. (2.12)] for argon ions in a magnetic field of 1 kG is $n_B = 6.63 \times 10^5$ cm^{-3}. Small numbers of ions have a confinement time of the order of 1 s at a neutral gas pressure of 10^{-6} torr, so that with ions being formed in the path of the beam at a rate greater than 10^8 cm^{-3}s^{-1}, the density will approach the Brillouin limit in a matter of milliseconds, unless space charge is sufficient to allow ions to escape through the endcaps. This latter possibility will occur for low confining potentials. We can estimate the minimum value of V required to prevent such a loss by considering a spheroidal equilibrium plasma with the diameter of the electron beam, the length of the trap, and the Brillouin density. The value of V for

which this equilibrium is obtained is found from Eq. (2.10), which may be written

$$2\pi z_0^2 q \frac{n}{V} = \frac{\alpha^2 - 1}{Q_1^0 [\alpha(\alpha^2 - 1)^{-1/2}]}, \tag{5.5}$$

by setting $n = n_B$ and $\alpha = z_0/r_{beam}$. For argon ions in a magnetic field of 1 kG, the result is $V_{min} = 0.45$ volts. By contrast, for an electron plasma of the same diameter as the electron beam to have the Brillouin density would require a confinement voltage greater than 30 kV.

For the ion plasmas we have studied, $V > V_{min}$, so charge is not expected to escape along the trap axis before the Brillouin density is reached. Radial transport due to gas scattering will be minor on the millisecond time-scale, but once the Brillouin density is reached, the addition of more ions will cause immediate expansion due to the loss of radial force balance. The ion distribution that evolves as ions are continually added is probably not a true thermal equilibrium, but because of the nearly unmagnetized nature of the interior of these high density plasmas, it may be reasonable to assume that the force balance achieved in equilibrium is approximately attained by these plasmas. The data presented in Sections 5.3 and 5.4 support the contention that the plasmas formed in steady state may be adequately described as Brillouin-density spheroids with aspect ratios determined by the cold fluid equilibrium [Eq. (5.5)].

With the aspect ratio determined by the Brillouin density and the confining voltage V according to Eq. (5.5), the remaining ingredient of the model is the plasma size. With ions being continually produced, the plasma will grow in size (maintaining a fixed aspect ratio) until it contacts one of the electrodes, after which additional ions formed will flow to that electrode, and a steady state will be established. For a fixed value of B, the aspect ratio varies with V, with increasing values of V leading to increasingly oblate spheroids. A plasma with an aspect ratio of $\alpha = 1/\sqrt{2}$ has

the right shape to touch both the endcaps and the ring electrode, giving it a volume of about 2×10^3 cm^3, the largest spheroidal plasma that may be confined in this trap. The confinement voltage, V_t, that produces this plasma shape may be found from Eq. (5.5), and can be shown to be a constant multiple of the critical voltage, V_c, above which confinement is lost:

$$V_t = (2 - \pi/2)V_c. \tag{5.6}$$

For $V < V_t$, the plasma length is fixed at $L = 2z_0$, and excess ions leave through the endcaps. Due to collisions, some particles will be transported radially out of the Brillouin-density core and will diffuse to the ring electrode. Our inference is that they form a tenuous halo plasma surrounding the core. For $V > V_t$, the plasma radius is fixed at $r_p = \rho_0$, and there is no halo plasma. The plasmas described by this model for various values of V are shown schematically in Fig. 5.2.

5.3 Total Charge Measurement

It would be desirable to measure the plasma profiles directly by dumping the plasma onto the collector plates. There are two difficulties with this approach. The most fundamental problem is that if the plasmas are indeed near the Brillouin density, then the particles are not following magnetic field lines in the tight helices familiar from low-density electron plasmas. It is possible that during the dump the particles may become sufficiently magnetized to give some information. A problem specific to this experiment is that these large plasmas must be dumped through the moderate-sized hole in one of the endcaps. One might still hope to obtain data on the central portion of the plasma, but instead a sort of universal profile, shown in Fig. 5.3, is obtained for all but the narrowest plasmas. Although the total charge received varies, the distribution is always strongly peaked in the center. This is

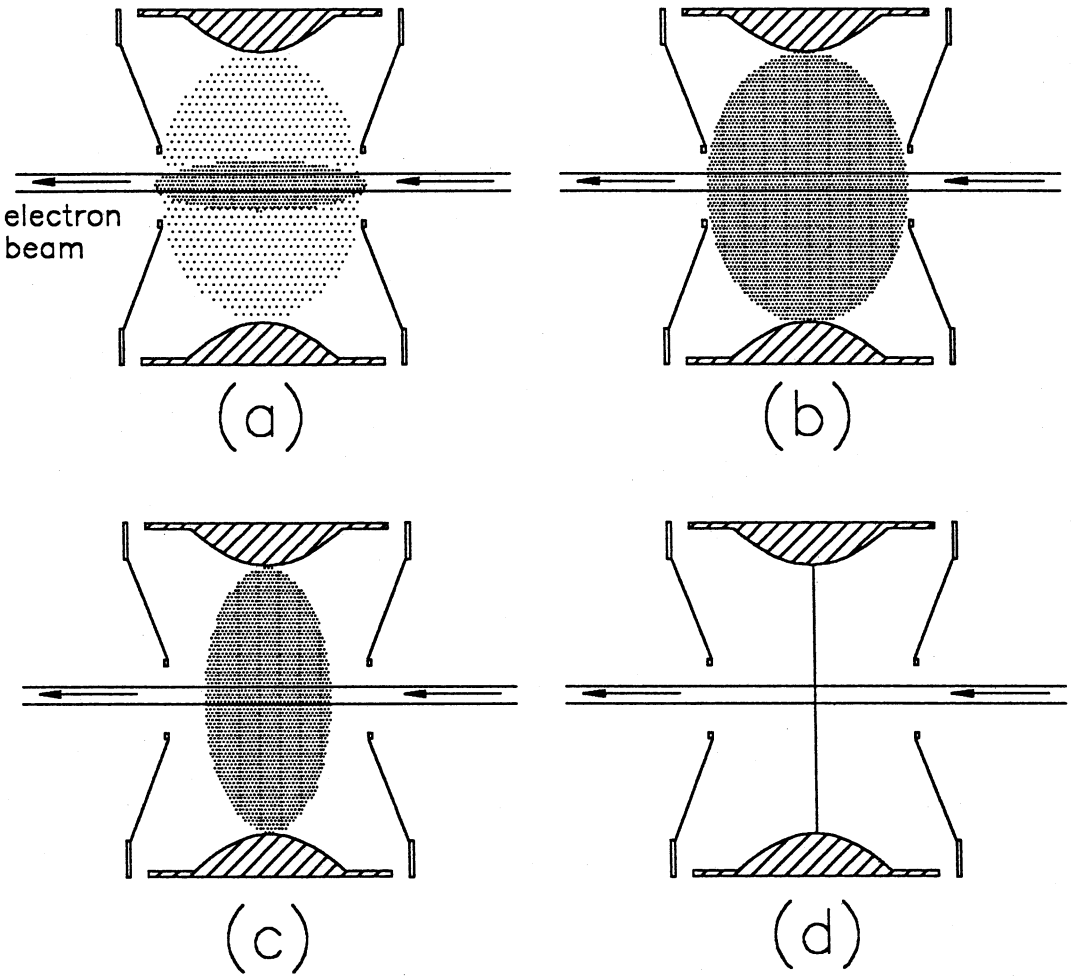

Figure 5.2: Model of the steady-state ion plasma for (a): $V_{\min} < V < V_t$, endcap-limited plasma with halo, $\alpha > 1/\sqrt{2}$, (b): $V = V_t$, transition plasma, $\alpha = 1/\sqrt{2}$, (c): $V_t < V < V_c$, ring-limited plasma, $\alpha < 1/\sqrt{2}$ and (d): $V = V_c$, disk plasma, $\alpha = 0$. For $V > V_c$, there is no plasma.

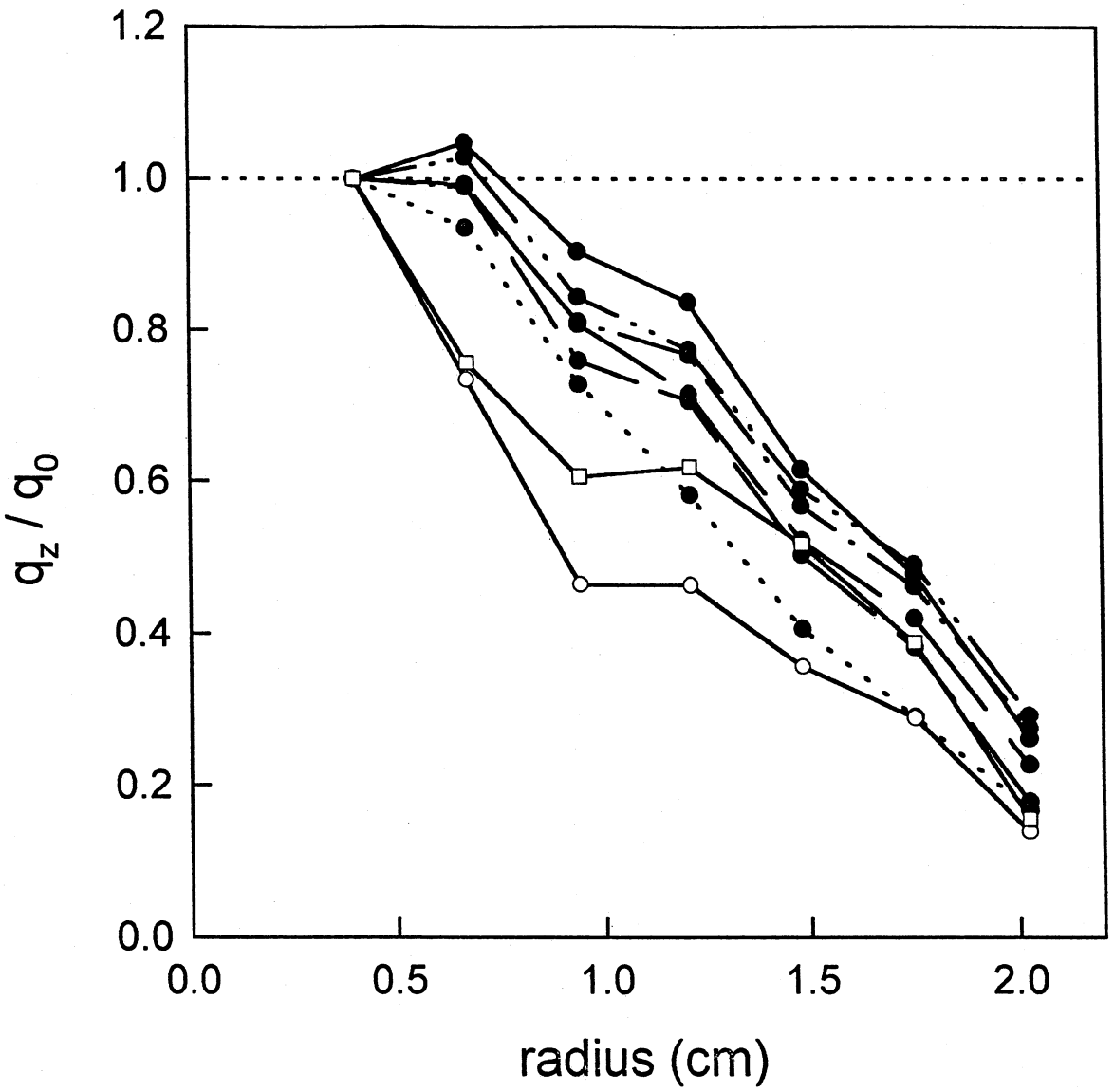

Figure 5.3: Radial profile data for argon ion plasmas with V spanning the range $V_{\min} < V < V_c$, each scaled by its central value, showing failure of the density diagnostic.

consistent with a particle orbit radius comparable to or larger than the hole in the endcap, as is expected from the model. The difficulties with charge dumping also prevent us from measuring the plasma temperature.

We have no replacement for the incapacitated profile measurement, but under some conditions, a measurement of the total plasma charge can be obtained by measuring the image charge flowing onto the confining electrodes as the trap fills. Because the filling is rapid (about 100 ms), a current spike is produced on the ring electrode when the electron beam is first switched on. For $V < V_t$, this spike is clearly distinguishable from the dc current which is established once the trap has been filled. Typical current traces, obtained using an electrometer, are shown in Fig. 5.4. The total charge is obtained by integrating the current spikes from all electrodes and correcting for the contribution from the image charge of the beam, which causes the small negative current spike seen at $t = 0$. The measurement is unambiguous for small values of V, but as V approaches V_t, the current traces become more complicated, as shown in Fig. 5.4(b), making it difficult to decide when to stop the integration. The reason for these complicated features is not understood, but may be involved with the formation of a plasma sheath at either the endcaps or the ring electrode. For $V > V_t$, there is no clear separation between image charge current and the arrival of the steady state current, and the technique is not applicable.

Figure 5.5 shows how the measured stored charge increases as V is increased. The error bars represent the uncertainty introduced by transient features of the sort shown in Fig. 5.4(b). The solid symbols represent the most plausible analysis. Using the model described in Sec. 5.2, the total charge in the Brillouin core is given by

$$Q = 4\pi r_p^3 \alpha n_B/3, \tag{5.7}$$

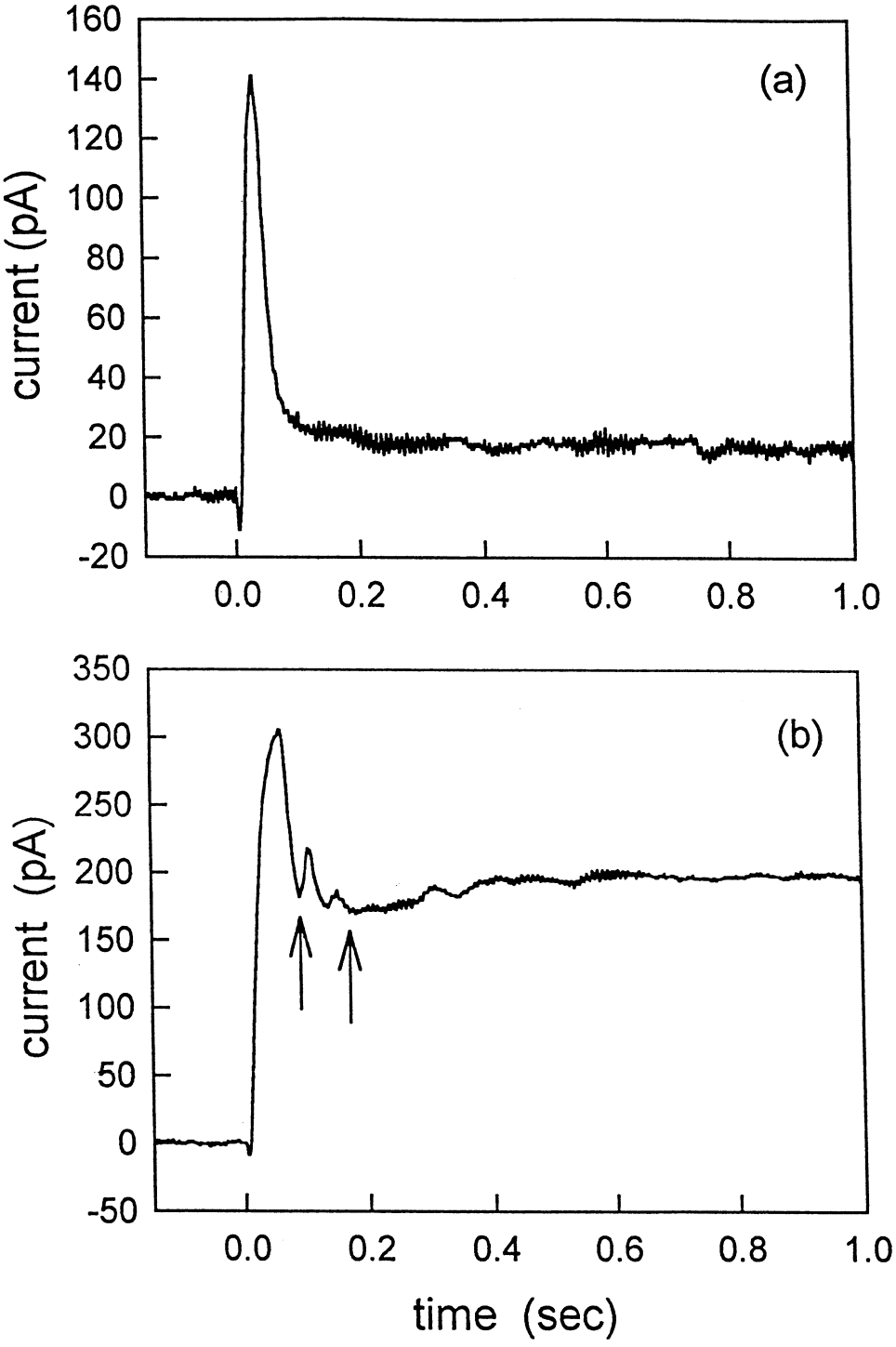

Figure 5.4: Current transient to the ring electrode when electron beam is switched on at $t = 0$, for an argon plasma with $B = 1.31$ kG and (a): $V = 5$ volts; (b): $V = 12.5$ volts. The arrows indicate the integration endpoints corresponding to the bounds of the error bars in Fig. 5.5.

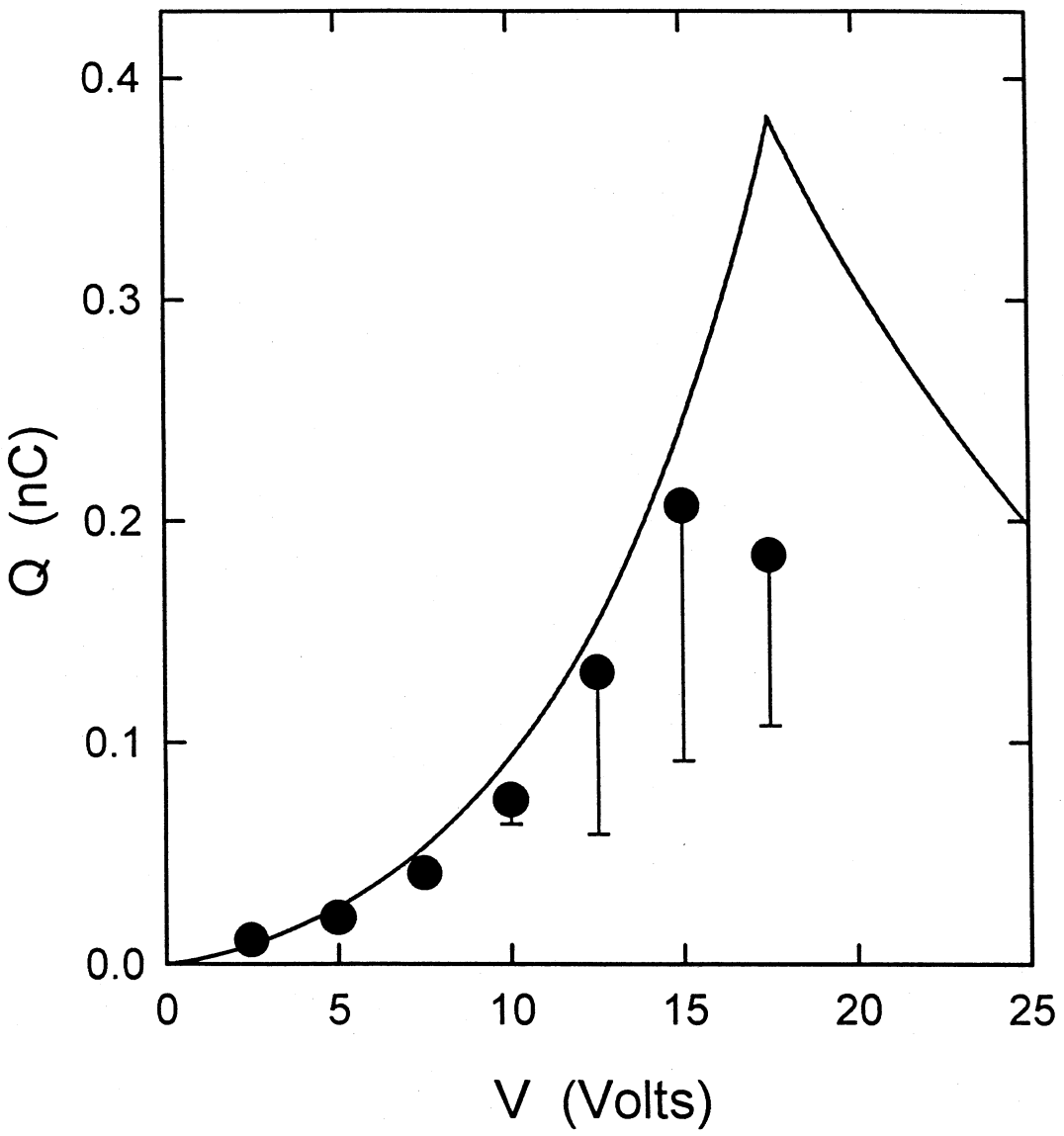

Figure 5.5: Total charge of argon ion plasma with $B = 1.31$ kG and various values of V. The solid line is from the steady-state model.

which is shown by the solid line in Fig. 5.5. The agreement between the data and the model is reasonably good, and at least verifies that the total charge is within about a factor of two of the model for $V < V_t$. This analysis ignores the halo of particles believed to surround the Brillouin spheroid. The mode frequency data described in Sec. 5.5 suggests that this halo is not insubstantial, but we have no other information regarding it.

5.4 Transition in Ring Current

Less direct, but more convincing, evidence for the Brillouin spheroid model can be obtained by monitoring the steady state current to the ring electrode. As may be seen in the transient current traces shown in Fig. 5.4, the steady state current depends on V. It also depends on B, on the electron beam current, I_{beam}, and on the gas pressure, and all of the observed dependences are consistent with the model. In Fig. 5.6, the steady-state current to the ring is plotted as a function of V for various values of B and I_{beam}. In each case, the ring current is small for low values of V, corresponding in the model to the condition [Fig. 5.2(a)] in which the core plasma is not in contact with the ring, and most excess ions leave via the endcaps. The current increases with V until an abrupt increase occurs, presumably when $V \simeq V_t$ and the plasma contacts the ring [Fig. 5.2(b)]. The transition often shows substantial hysteresis, in which case the value obtained by approaching from lower values of V is recorded, since it matches the result obtained by dumping the plasma and refilling. The hysteresis may be associated with the formation of a plasma sheath when the ring is contacted. Further increases in V result in only slight increases in the ring current, which should now be the entire ion formation current. Comparing the different cases, we note that the value of B affects the value of V_t, but not the current for $V > V_t$. The beam current affects the current for

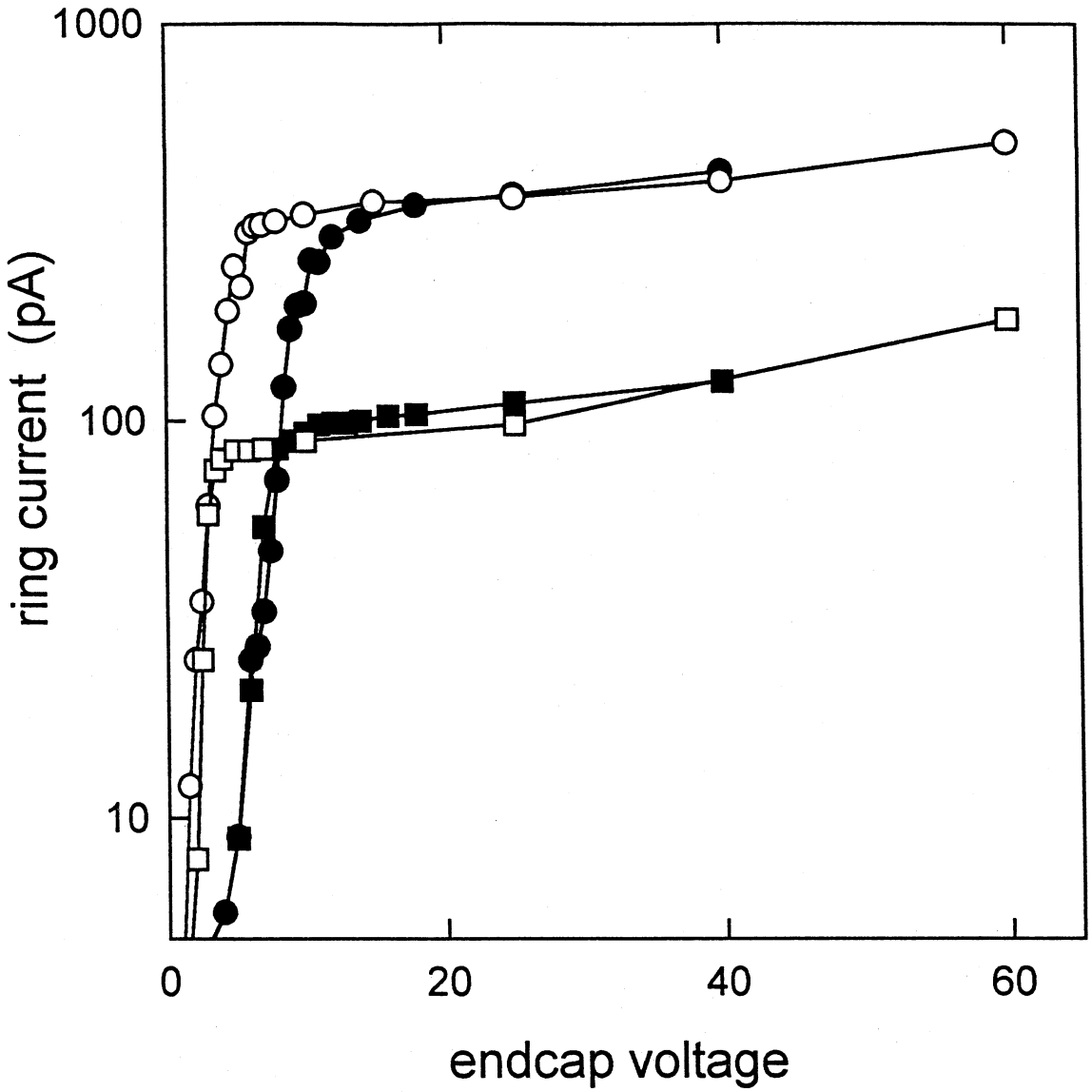

Figure 5.6: Steady-state current to the ring electrode as a function of V for an argon plasma at a pressure of 2.4×10^{-8} torr and with (□): $B = 290$ G, $I_{\text{beam}} = 10\mu$A; (○): $B = 290$ G, $I_{\text{beam}} = 40\mu$A; (□): $B = 580$ G, $I_{\text{beam}} = 10\mu$A; (○): $B = 580$ G, $I_{\text{beam}} = 40\mu$A.

$V > V_t$, as expected, but not for $V < V_t$. This is consistent with gas-scattering-induced radial current from the Brillouin core. As long as the ion formation rate is sufficient to keep the core filled, additional ions will leave through the endcaps, having no effect on the current to the ring. Finally, it is found that the ring current is approximately proportional to the gas pressure for all values of V. For $V > V_t$, this simply represents another way to get extra ion formation, which should add to the ring current. For $V < V_t$, the extra ions have no effect, but the rate at which ions scatter out of the core and migrate toward the ring is increased.

Because of the large hole in each endcap, most of the ion current that would flow to them for $V < V_t$ passes through the hole. The maximum endcap current is collected for $V \simeq V_t$, as expected, since these wide plasmas might be expected to make some contact with the endcaps.

Figure 5.7 shows the measured value of the transition voltage as a function of magnetic field for four ion species. Also shown in this figure are the expected dependences, $V_t = (2 - \pi/2)V_c$, based on the model described in Sec. 5.2. No fitted parameters are used.

The excellent agreement between the model and the experiment, both for the total charge and for the ring current threshold, supports the contention that most of the charge is contained in a plasma core at a density near n_B, with a diffuse halo plasma.

5.5 Azimuthal Modes

Plasma modes are excited by applying a signal to one of the sectors of the ring electrode and detecting the plasma response on the opposite sector, as shown in Fig. 5.1. Frequency spectra are measured using a spectrum analyzer and a tracking

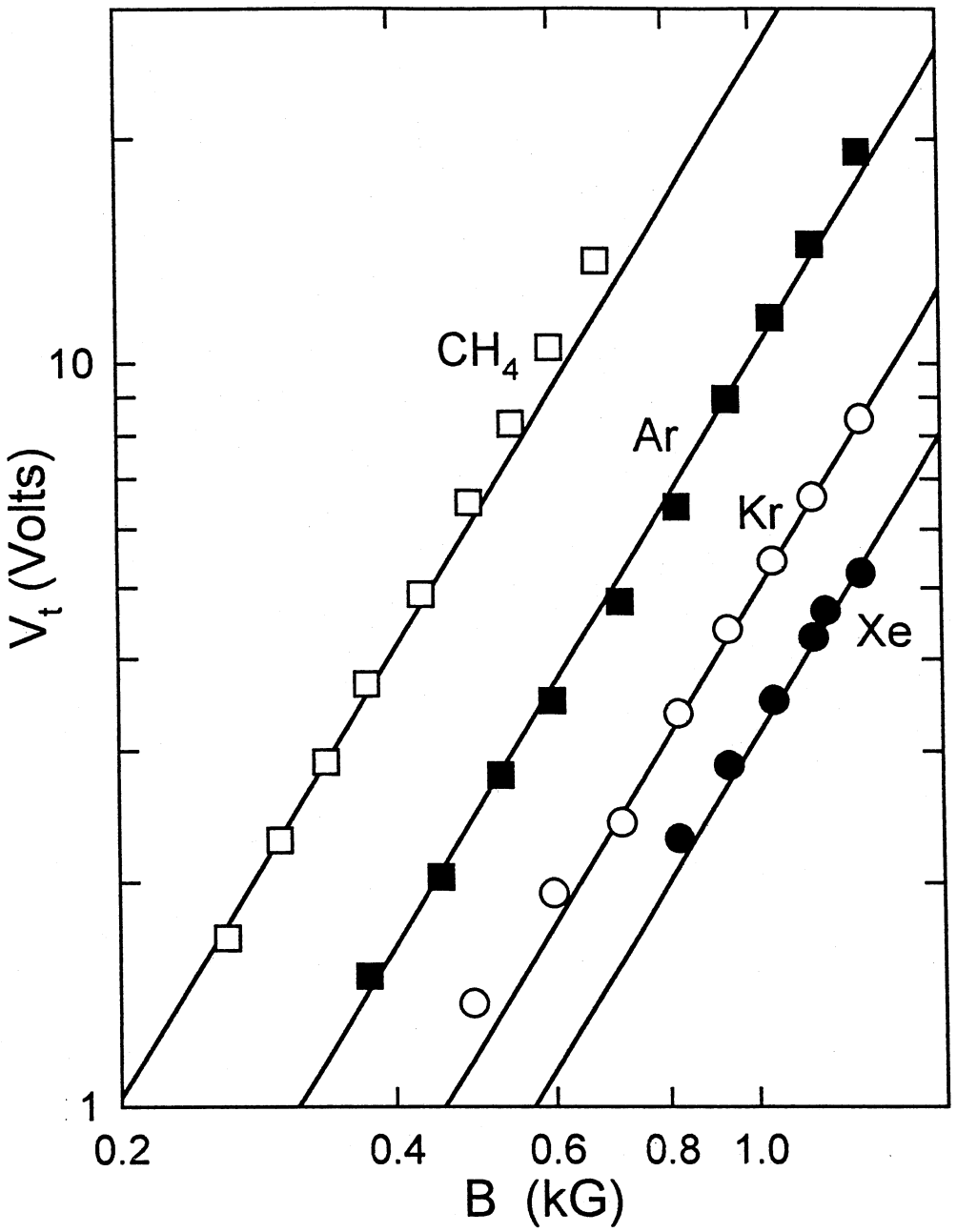

Figure 5.7: Measured transition voltage as a function of B for four different ion species. Solid lines are from the model.

generator. A typical spectrum is shown in Fig. 5.8, and two families of modes are discernible. One family has frequencies near Ω_c and has some similarity to the cyclotron modes studied by Gould and LaPointe [1991,1992] in electron plasmas. The lower-frequency family are the diocotron modes [*Davidson*, 1990]. A series of spectra like that shown in Fig. 5.8 were taken for steady-state argon plasmas for various values of V in the range $V_{\min} < V \leq V_c$. Figure 5.9 displays the frequencies of the resonances observed as functions of V. A striking feature of the data is the wide variation seen in the frequencies as V is varied over the range of values providing confinement. It is also evident that the character of the modes changes near $V = V_t$.

The plasma modes that should be most strongly excited by this technique are the purely azimuthal modes of the form $\delta\Phi \sim e^{i(m\phi-\omega t)}$ discussed in Sec. 2.2. The indicated values of m were determined experimentally by the phase differences between the signals detected on different sectors. Because pairs of cyclotron and diocotron modes with the same values of m are detected, the rotation frequency may be deduced using Eq. (2.30). The open circles in Fig. 5.9 are the values of ω_r obtained by applying this procedure to the observed mode frequencies, using $m = 2$, $m = 3$, and $m = 4$ modes for $V < V_t$ and the $m = 2$ modes for $V > V_t$.

Consider now the modes for $V < V_t$. As shown in Fig. 5.9, the inferred rotation frequency (shown by open circles) is close to $2\Omega_{\rm M}$, rather than $\Omega_c/2$, which would characterize the Brillouin core. We interpret this to mean that the observed modes are supported in the halo plasma, which effectively shields the core. Using these inferred rotation frequencies, we find that the frequency data may be fit to Eq. (2.28) by assuming $\omega_p^2 G_m = K_m \omega_z^2$, where $K_1 = 0.69$ and $K_m = 1.24$ for $m > 1$. These fit curves are the solid lines plotted for $V < V_t$ in Fig. 5.9. Also shown, for the whole range of V, are $\Omega_{\rm M}$ and Ω_c', which should not depend on plasma parameters.

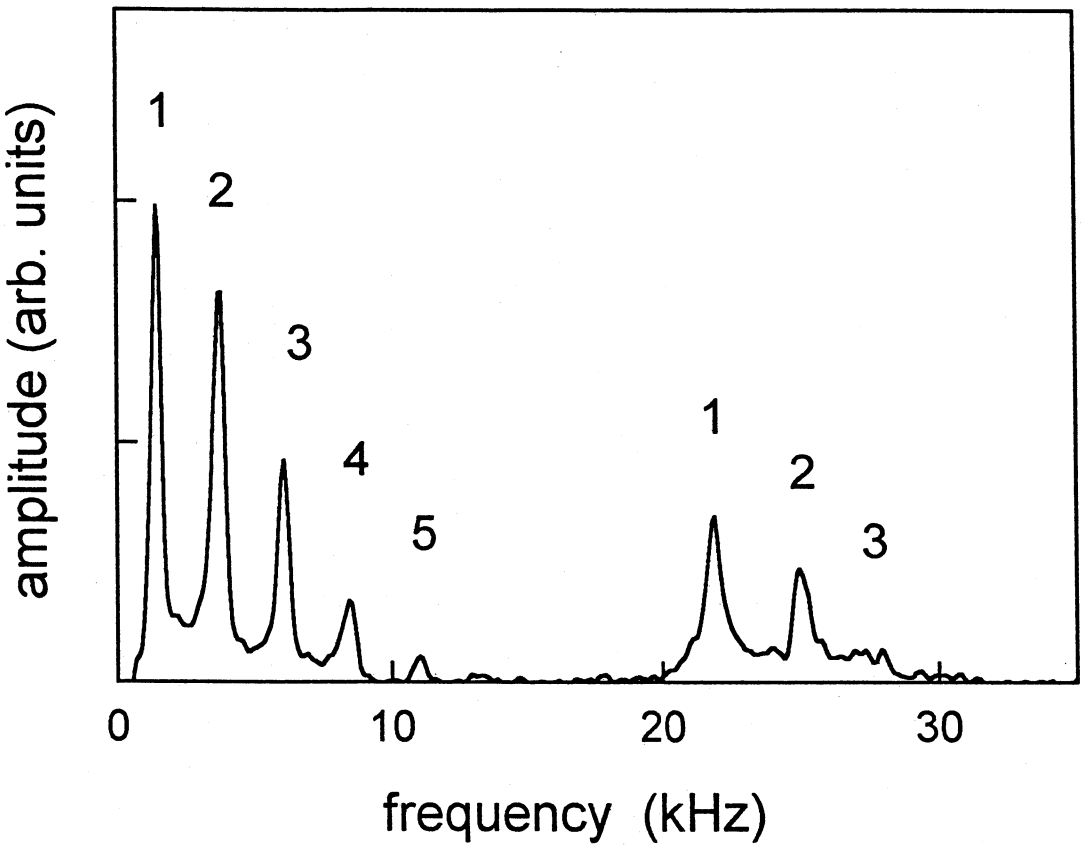

Figure 5.8: Spectrum of azimuthal modes of an argon plasma, showing diocotron modes (0 to 10 kHz) and cyclotron modes (20 to 30 kHz). The numbers indicate experimentally determined values of m.

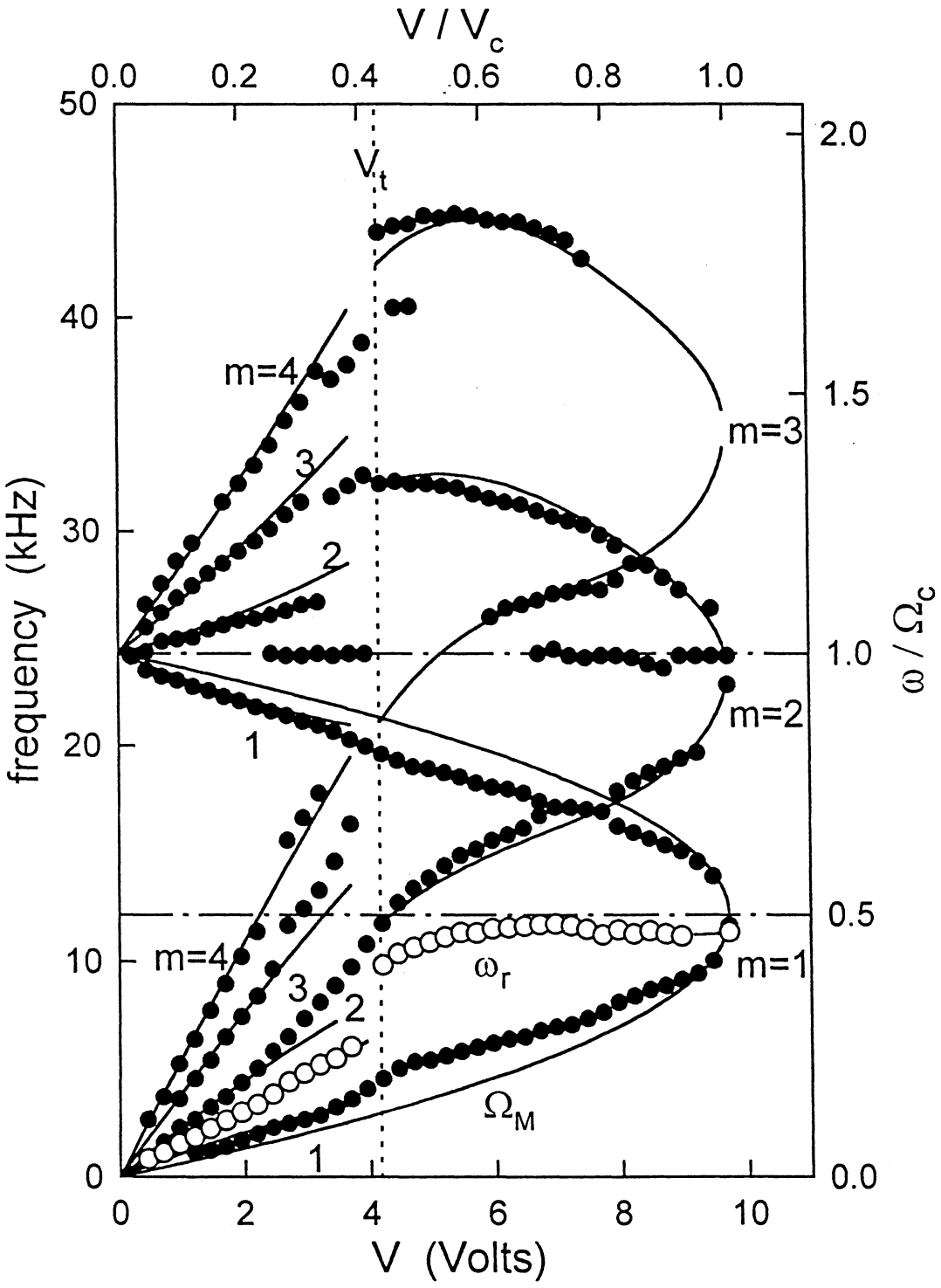

Figure 5.9: Azimuthal mode frequencies of argon plasmas with $B = 640$ G as functions of V. Values of m determined experimentally. ω_r calculated from mode frequencies using Eq. (2.30). Solid lines are described in the text.

The implications of this fit and of the observation that $\omega_r \simeq 2\Omega_M$ for the nature of the halo plasma are not understood at present.

For $V > V_t$, the ring current data lead us to believe that the entire plasma can be described as a uniform-density spheroid with $n \simeq n_B$. Using Eq. (2.8) to determine ω_p^2 (and thus n) from the measured values of ω_r shown in Fig. 5.9, we find that n varies from $0.96n_B$ to greater than $0.99n_B$ for all values of V above V_t. After using Eq. (2.10) to calculate α from ω_p^2, we can use Eq. (2.28) to find the mode frequencies predicted by the cold fluid theory. The results are displayed in Fig. 5.9 as the solid lines shown for $V > V_t$. These calculations are in good agreement with the data, without using any fitted parameters, except for the $m = 1$ modes. This discrepancy could result from the effects of image charge, which are not included in the model and which are expected to be most pronounced for modes with the lowest m-numbers. We note, however, that the sum of the frequencies of the $m = 1$ modes is quite close to Ω_c, which could account for the excitation of the weak mode observed near Ω_c, via a nonlinear coupling. We note also that a mode coupling occurs between the $m = 1$ cyclotron mode and the $m = 2$ diocotron mode near $V = 0.75V_c$.

The remarkable simplicity of the steady state of these plasmas, the surprising degree to which the spheroidal mode theory is satisfied, and the apparently rich variety of phenomena that may be observed suggest that further experiments with similar systems are warranted. A pulsed beam could produce similar plasmas which do not touch the walls, and other variations are also possible. It appears that creating and studying plasmas at the Brillouin limit is both interesting and relatively straightforward.

Chapter 6

Conclusions

The original goal of this work, the development of a technique to monitor trapped positrons, has been achieved. The small number of positrons initially available and the relatively low temperature to which they cool led to the consideration of plasmas in quadrupole potentials, the approximate form near the minimum of any potential well. In this sense, the apparently exotic spheroidal geometry is perhaps the most natural one for single-component plasmas.

Much of the work of this thesis may be considered as experimental verification of various aspects of Dubin's comprehensive normal mode theory. As such, it complements the work at NIST [*Heinzen et al.*, 1991; *Bollinger et al.*, 1993], in which excellent agreement with the theory has been obtained for the frequencies of the quadrupole mode and the $l = 2$, $m = 1$ mode of cold ion microplasmas. Under the proper conditions, confidence in the theory is sufficient to justify its use as a measurement tool, as in the studies by Weimer [1993] of cryogenic electron plasmas.

Because some of the conditions of our experiments are set by considerations other than the production of small, cold, precisely spheroidal plasmas, we have had to consider the effects of various perturbations. Important effects of which we are aware include those due to image charges (the plasma is not small enough),

nonuniform density profile (the plasma is not in global thermal equilibrium), trap anharmonicity, and plasma temperature. At this point, some progress has been made in understanding the frequency shifts caused by finite temperature, which can now be used to measure this important quantity. By varying N, varying the trap anharmonicity, and allowing electron plasmas time to reach equilibrium after pumping out the buffer gas, it may be possible to unravel the separate effects of the remaining perturbations, and such experiments are planned. The success of the numerical simulations by Spencer and Mason in matching the quadrupole mode data suggests that such calculations could be of great use in this endeavor. That all these complications may be treated as small perturbations to the cold fluid theory, even for the rather extreme case of the large ion plasmas discussed in Ch. 5, suggests that the theory will continue to be of great utility.

The very simple technique described in Ch. 5 for generating ion plasmas may prove to be of use in other single-component plasma traps. Electron plasma machines usually have rather low magnetic fields by the standards of ion plasma experiments, but this makes the Brillouin limit easily accessible, and their very nice electron beam hardware is ready to use. A puff of gas could be introduced by a valve and used to form a plasma, after which the remaining gas would quickly pump away. The plasmas need not reach the Brillouin density nor touch the wall, and some interesting studies might be made of transport in plasmas that follow guiding-center dynamics to varying degrees. Even in ion plasma machines, which are typically designed to use laser-induced fluorescence diagnostics and are thus restricted to ion species with favorable atomic properties, the ability to form plasmas of predominantly the singly ionized species might be of occasional use. In one ion plasma trap [*Sarid et al.*, 1994], some difficulties have been ascribed to the injection of plasma from a low-field source region into the high-field center of the trap. The formation of ions inside

the confinement region might be of use in the study of such phenomena, though this technique cannot produce the Mg ions required for that experiment.

Quadrupole traps and spheroidal plasmas offer the chance to approach some of the unsolved problems of nonneutral plasmas from a new perspective. If a phenomenon has been tentatively identified as a "3D" effect in cylindrical plasmas, it might be interesting to repeat the experiment with spheroidal plasmas, in which the 3D nature is under experimental control and is perhaps better understood. The features that make quadrupole traps appealing to atomic physicists, the exactly soluble simple harmonic motions of single particles and their long confinement time, may make for an interesting test of field-error transport, since resonances with field errors could be very strong (the harmonic frequencies do not shift off resonance as the amplitude of motion grows) and would be shared by all particles, if space charge is negligible. Because good confinement does not require the strong self-field of a well-developed plasma, it may also be possible to learn about the nature of marginal plasmas and of the transition, seen in one guise in Fig. 4.3(a), from independent particle motions to the collective behavior of a plasma.

The experimental study of spheroidal plasmas has not yet advanced to the degree of maturity achieved in the study of cylindrical plasmas. I hope that the work presented in this thesis will persuade other researchers of the many interesting plasma experiments waiting to be done in quadrupole traps.

Appendix A

Associated Legendre Functions of the Second Kind

The associated Legendre functions of the first kind (P_l^m) and the Legendre polynomials, $P_l \equiv P_l^0$, are frequently encountered in theoretical physics. The associated Legendre functions of the second kind (Q_l^m), however, are less familiar. The lowest-order functions are presented here for convenience.

A possible source of confusion is the presence in the literature of two different definitions of these functions associated with different choices for the required branch cut. The argument of these functions as used in the spheroidal equilibrium [Eq. (2.10)] and the dispersion relation [Eq. (2.26)] is $k_2 = \alpha(\alpha^2 - 1)^{-1/2}$, which varies over the range $1 \leq k_2 < \infty$ for plasma aspect ratios in the range $1 \leq \alpha < \infty$. Thus, a common definition of the Q_l^m's which places branch cuts along the real axis from $-\infty < \Re(z) < -1$ and from $1 < \Re(z) < \infty$, is not useful. Instead, a single branch cut is placed along the real axis from $-\infty < \Re(z) < 1$. This choice of branch cut may be enforced when performing calculations with the symbolic math program Mathematica by the declaration "LegendreType $\rightarrow$ Complex" in the function call.

Some of the functions relevant to the axial plasma modes are

$$Q_1^0(x) = -1 + \tfrac{x}{2} \ln\left(\tfrac{x+1}{x-1}\right)$$

$$Q_2^0(x) = -\tfrac{3}{2}x + \tfrac{3x^2-1}{4}\ln\left(\tfrac{x+1}{x-1}\right)$$
$$Q_3^0(x) = -\tfrac{5}{2}x^2 + \tfrac{2}{3} + \tfrac{5x^3-3x}{4}\ln\left(\tfrac{x+1}{x-1}\right)$$
$$Q_4^0(x) = -\tfrac{35}{8}x^3 + \tfrac{55}{24}x + \tfrac{35x^4-30x^2+3}{16}\ln\left(\tfrac{x+1}{x-1}\right)$$
$$Q_5^0(x) = -\tfrac{63}{8}x^4 + \tfrac{49}{8}x^2 - \tfrac{8}{15} + \tfrac{63x^5-70x^3+15x}{16}\ln\left(\tfrac{x+1}{x-1}\right).$$

Functions appearing in the azimuthal mode theory include

$$Q_1^1(x) = \left[-2x + (x^2-1)\ln\left(\tfrac{x+1}{x-1}\right)\right]/2\sqrt{1-x^2}$$
$$Q_2^2(x) = \left[-6x^3 + 10x + (3x^4 - 6x^2 + 3)\ln\left(\tfrac{x+1}{x-1}\right)\right]/2(1-x^2)$$
$$Q_3^3(x) = \left[-30x^5 + 80x^3 - 66x + (15x^6 - 45x^4 + 45x^2 - 15)\ln\left(\tfrac{x+1}{x-1}\right)\right]\tfrac{(1-x^2)^{-3/2}}{-2x^6+6x^4-6x^2+2}.$$

A few other functions may be of use in future experiments:

$$Q_2^1(x) = \left[-6x^2 + 4 + (3x^3 - 3x)\ln\left(\tfrac{x+1}{x-1}\right)\right]/2\sqrt{1-x^2}$$
$$Q_3^1(x) = \left[-30x^3 + 26x + (15x^4 - 18x^2 + 3)\ln\left(\tfrac{x+1}{x-1}\right)\right]4\sqrt{1-x^2}$$
$$Q_3^2(x) = \left[-30x^4 + 50x^2 - 16 + (15x^5 - 30x^3 - 15x)\ln\left(\tfrac{x+1}{x-1}\right)\right]/2(1-x^2).$$

Appendix B

Analytical Formulae for Spheroidal Plasmas

An explicit form for the spheroidal equilibrium, expressed in terms of Q_1^0 in Eq. (2.10), is

$$\frac{\omega_p^2}{\omega_z^2} = \begin{cases} (1-\alpha^2)^{3/2}\left[\sqrt{1-\alpha^2} - \alpha \arcsin\sqrt{1-\alpha^2}\right]^{-1}, & \text{for } \alpha < 1 \\ (\alpha^2-1)^{3/2}\left[\frac{\alpha}{2}\ln\left(\frac{\alpha+\sqrt{\alpha^2-1}}{\alpha-\sqrt{\alpha^2-1}}\right) - \sqrt{\alpha^2-1}\right]^{-1}, & \text{for } \alpha > 1. \end{cases} \tag{2.1}$$

This corresponds to $1/B(\alpha)$, in the notation of Heinzen [1991].

The frequency of the quadrupole mode of a cold, strongly magnetized spheroidal plasma has the somewhat ungainly form

$$\left(\frac{\omega_2^{\mathrm{CF}}}{\omega_z}\right)^2 = 1 + \frac{\alpha^2}{\alpha^2-1}\frac{(\alpha^2+\frac{1}{2})\ln\left(\frac{\alpha+\sqrt{\alpha^2-1}}{\alpha-\sqrt{\alpha^2-1}}\right) - 3\alpha\sqrt{\alpha^2-1}}{\frac{\alpha^2}{2}\ln\left(\frac{\alpha+\sqrt{\alpha^2-1}}{\alpha-\sqrt{\alpha^2-1}}\right) - \alpha\sqrt{\alpha^2-1}}, \tag{2.2}$$

for $\alpha > 1$, the case typical of our electron plasmas.

Finally, a few notes on the roots of the dispersion relation of axial modes for the strongly magnetized case. The dispersion relation, Eq. (2.27), may be written in the form

$$(k_1^2-1)P_l'(k_1) = w_l(\alpha)k_1 P_l(k_1), \tag{2.3}$$

where $k_1 = \alpha(\alpha^2 - 1 + \omega_p^2/\omega^2)^{-1/2}$ and

$$w_l(\alpha) = \frac{1}{\alpha\sqrt{\alpha^2-1}}\frac{Q_l^{0\,\prime}(\frac{\alpha}{\sqrt{\alpha^2-1}})}{Q_l^0(\frac{\alpha}{\sqrt{\alpha^2-1}})}. \tag{2.4}$$

Equation (2.3) is a polynomial in k_1 of order $l+1$, with coefficients that depend on α. For even values of l, a factor of k_1 divides out. For any l, the result is a polynomial in k_1^2 of order $[(l+1)/2]$, where "[]" denotes the maximum integer. Thus, there is one root for $l = 1$ or $l = 2$, and there are two roots for $l = 3$ or $l = 4$, etc. Each solution for k_1^2 at a particular value of α translates into the value of ω for the normal mode, scaled by ω_p. The different eigenvalues of ω obtained for the same values of l and m correspond to normal modes with different radial structure. The modes with purely axial structure have the highest frequencies.

References

Beck, B. R., J. Fajans, and J. H. Malmberg, Measurement of collisional anisotropic temperature relaxation in a strongly magnetized pure electron plasma, *Physical Review Letters*, **68**, 317–20, 1992.

Bollinger, J. J., J. D. Prestage, W. M. Itano, and D. J. Wineland, Laser-cooled-atomic frequency standard, *Physical Review Letters*, **54**, 1000–1003, 1985.

Bollinger, J. J., D. J. Heinzen, F. L. Moore, W. M. Itano, D. J. Wineland, and D. H. E. Dubin, Electrostatic modes of ion-trap plasmas, *Physical Review A*, **48**, 525–545, 1993.

Bollinger, J. J., D. J. Wineland, and D. H. E. Dubin, Non-neutral ion plasmas and crystals, laser cooling, and atomic clocks, *Physics of Plasmas*, **1**, 1403–1414, 1994.

Brillouin, L., A theorem of Larmor and its importance for electrons in magnetic fields, *Physical Review*, **67**, 260–266, 1945.

Brown, L. S., and G. Gabrielse, Geonium theory: physics of a single electron or ion in a Penning trap, *Reviews of Modern Physics*, **58**, 233–313, 1986.

Brown, S. C., *Basic Data of Plasma Physics.* John Wiley and Sons, New York, 1959.

Davidson, R. C., *Physics of Nonneutral Plasmas.* Addison-Wesley, Redwood City, California, 1990.

de Grassie, J. S., and J. H. Malmberg, Wave-induced transport in the pure electron plasma, *Physical Review Letters*, **39**, 1077–80, 1977.

Dehmelt, H., Experiments with isolated subatomic particles at rest, *Reviews of Modern Physics*, **62**, 525, 1990.

Driscoll, C. F., and K. S. Fine, Experiments on vortex dynamics in pure electron plasmas, *Physics of Fluids B*, **2**, 1359–1366, 1990.

Driscoll, C. F., and J. H. Malmberg, Hollow electron column from an equipotential cathode, *Physics of Fluids*, **19**, 760–761, 1976.

Driscoll, C. F., and J. H. Malmberg, Length-dependent containment of a pure electron-plasma column, *Physical Review Letters*, **50**, 167–170, 1983.

Dubin, D. H. E., Theory of electrostatic fluid modes in a cold spheroidal non-neutral plasma, *Physical Review Letters*, **66**, 2076–2079, 1991.

Dubin, D. H. E., Equilibrium and dynamics of uniform density ellipsoidal non-neutral

plasmas, *Physics of Fluids B*, **5**, 295–324, 1993.

Dubin, D. H. E., private communication, 1994.

Dubin, D. H. E., and J. P. Schiffer, Normal modes of a strongly correlated nonneutral plasma in a harmonic trap, to be published, 1994.

Eggleston, D. L., C. F. Driscoll, B. R. Beck, A. W. Hyatt, and J. H. Malmberg, Parallel energy analyzer for pure electron plasma devices, *Physics of Fluids B*, **4**, 3432–3439, 1992.

Fine, K. S., C. F. Driscoll, J. H. Malmberg, and T. B. Mitchell, Measurements of symmetric vortex merger, *Physical Review Letters*, **67**, 588–591, 1991.

Fine, K. S., C. F. Driscoll, and X. P. Huang, Observations of two-dimensional turbulence with a one-shot density diagnostic, *Bulletin of the American Physical Society*, **38**, 1971, 1993.

Gabrielse, G., X. Fei, K. Helmerson, S. L. Rolston, and others;, First capture of antiprotons in a Penning trap: a kiloelectronvolt source, *Physical Review Letters*, **57**, 2504–2507, 1986.

Gabrielse, G., S. L. Rolston, L. Haarsma, and W. Kells, Antihydrogen production using trapped plasmas, *Physics Letters A*, **129**, 38–42, 1988.

Gabrielse, G., L. Haarsma, and S. L. Rolston, Open-endcap Penning traps for high precision experiments, *International Journal of Mass Spectrometry and Ion Processes*, **88**, 319–332, 1989.

Gabrielse, G., X. Fei, L. A. Orozco, R. L. Tjoelker, J. Haas, H. Kalinowsky, T. A. Trainor, and W. Kells, Thousandfold improvement in the measured antiproton mass, *Physical Review Letters*, **65**, 1317–1320, 1990.

Glinsky, M. E., and T. M. O'Neil, Guiding center atoms: Three-body recombination in a strongly magnetized plasma, *Physics of Fluids B*, **3**, 1279–1293, 1991.

Glish, G. L., R. G. Greaves, S. A. McLucky, L. D. Hulett, C. M. Surko, J. Xu, and D. L. Donohue, Ion production by positron-molecule resonances, *Physical Review A*, **49**, 2389–2393, 1994.

Gould, R. W., and M. A. LaPointe, Cyclotron resonance in a pure electron plasma column, *Physical Review Letters*, **67**, 3685–3688, 1991.

Gould, R. W., and M. A. LaPointe, Cyclotron resonance phenomena in a pure electron plasma, *Physics of Fluids B*, **4**, 2038–2043, 1992.

Gramsch, E., J. Throwe, and K. G. Lynn, Development of transmission positron moderators, *Applied Physics Letters*, **51**, 1862–1864, 1987.

Greaves, R. G., M. D. Tinkle, and C. M. Surko, Creation and uses of positron plasmas, *Physics of Plasmas*, **1**, 1439–1446, 1994.

Heinzen, D. J., J. J. Bollinger, F. L. Moore, W. M. Itano, and D. J. Wineland, Rotational equilibria and low-order modes of a non-neutral ion plasma, *Physical Review Letters*, **66**, 2080–2083, 1991.

Holzscheiter, M. H., Trapping of antiprotons - a first step on the way to antihydrogen, *Hyperfine Interactions*, **81**, 71–85, 1993.

Hsu, T., and J. L. Hirshfield, Electrostatic energy analyzer using a nonuniform axial magnetic field, *Review of Scientific Instrumentation*, **47**, 236–238, 1976.

Huang, X.-P., and C. F. Driscoll, Relaxation of 2d turbulence to a metaequilibrium near the minimum enstrophy state, *Physical Review Letters*, **72**, 2187–2190, 1994.

Iwata, K., R. G. Greaves, and C. M. Surko, Annihilation rates of positrons on aromatic molecules, to be published in *Hyperfine Interactions*, 1993.

Iwata, K., R. G. Greaves, T. J. Murphy, M. D. Tinkle, and C. M. Surko, Measurements of positron annihilation rates on molecules, submitted to *Physical Review A*, 1994.

Jackson, J. D., *Classical Electrodynamics, Second Edition.* John Wiley and Sons, New York, 1975.

Khatri, R., M. Charlton, P. Sferlazzo, K. G. Lynn, A. P. Mills, Jr., and L. O. Roellig, *Applied Physics Letters*, **57**, 2374, 1990.

Malmberg, J. H., and J. S. de Grassie, Properties of nonneutral plasma, *Physical Review Letters*, **35**, 577–80, 1975.

Malmberg, J. H., and T. M. O'Neil, Pure electron plasma, liquid and crystal, *Physical Review Letters*, **39**, 1333–1336, 1977.

Mills, Jr., A. P., and E. M. Gullikson, Solid neon moderator for producing slow positrons, *Applied Physics Letters*, **49**, 1121–1123, 1986.

Mitchell, T. B., C. F. Driscoll, and K. S. Fine, Experiments on stability of equilibria of two vortices in a cylindrical trap, *Physical Review Letters*, **71**, 1371–1374, 1993.

Murphy, T. J., Positron deposition in plasmas by positronium beam ionization and trans-

port of positrons in tokamak plasmas, *Plasma Physics and Controlled Fusion*, **29**, 549–563, 1987.

Murphy, T. J., and C. M. Surko, Annihilation of positrons on organic molecules, *Physical Review Letters*, **67**, 2954–2957, 1991.

Murphy, T. J., and C. M. Surko, Positron trapping in an electrostatic well by inelastic collisions with nitrogen molecules, *Physical Review A*, **46**, 5696–5705, 1992.

O'Neil, T. M., A confinement theorem for nonneutral plasmas, *Physics of Fluids*, **23**, 2216–2218, 1980.

O'Neil, T. M., and C. F. Driscoll, Transport to thermal equilibrium of a pure electron plasma, *Physics of Fluids*, **22**, 266–277, 1979.

Passner, A., C. M. Surko, M. Leventhal, and A. P. Mills, Jr., Ion production by positron-molecule resonances, *Physical Review A*, **39**, 3706–3709, 1989.

Penning, F. M., Die glimmentladung bei niedrigem druck zwischen koaxialen zylindern in einem axialen magnetfeld, *Physica*, **3**, 873, 1936.

Peurrung, A. J., and J. Fajans, A pulsed microchannel-plate-based non-neutral plasma imaging system, *Review of Scientific Instruments*, **64**, 52–55, 1993.

Sarid, E., F. Anderegg, and C. F. Driscoll, Cyclotron modes of a pure ion plasma, *Bulletin of the American Physical Society*, **38**, 1971, 1993.

Sarid, E., F. Anderegg, and C. F. Driscoll, Cyclotron resonance phenomena in a multi-species non-neutral ion plasma, to be published, 1994.

Spencer, R. L., private communication, 1994.

Surko, C. M., and R. G. Greaves, Physics with trapped positron gases and plasmas, in *Condensed Matter and Plasmas in Physics and Astronomy*, edited by S. Ichimaru, and S. Ogata. to be published by Addison Wesley, 1994.

Surko, C. M., and T. J. Murphy, Use of the positron as a plasma particle, *Physics of Fluids B*, **2**, 1372–1375, 1990.

Surko, C. M., M. Leventhal, W. S. Crane, A. Passner, F. J. Wysocki, T. J. Murphy, J. Strachan, and W. L. Rowan, Use of positrons to study transport in tokamak plasmas, *Review of Scientific Instrumentation*, **57**, 1862–1867, 1986.

Surko, C. M., A. Passner, M. Leventhal, and F. J. Wysocki, Bound states of positrons and large molecules, *Physical Review Letters*, **61**, 1831–1834, 1988.

Surko, C. M., M. Leventhal, and A. Passner, Positron plasma in the laboratory, *Physical Review Letters*, **62**, 901–904, 1989.

Surko, C. M., R. G. Greaves, and M. Leventhal, Use of traps to study positron annihilation in astrophysically relevant media, *Hyperfine Interactions*, **81**, 239–252, 1993.

Tang, S., M. D. Tinkle, R. G. Greaves, and C. M. Surko, Annihilation gamma-ray spectra from positron-molecule interactions, *Physical Review Letters*, **68**, 3793–3796, 1992.

Tinkle, M. D., R. G. Greaves, C. M. Surko, R. L. Spencer, and G. W. Mason, Low-order modes as diagnostics of spheroidal nonneutral plasmas, *Physical Review Letters*, **72**, 352–355, 1994.

Turner, L., Collective effects on equilibria of trapped charged plasmas, *Physics of Fluids*, **30**, 3196–3203, 1987.

Weimer, C. S., F. L. Moore, and D. J. Wineland, High-order multipole excitation of a bound electron, *Physical Review Letters*, **70**, 2553–2556, 1993.

Wilkins, C. L., A. K. Chowdhury, L. M. Nuwaysir, and M. L. Coates, Fourier transform mass spectrometry: Current status, *Mass Spectrometry Reviews*, **8**, 67–92, 1989.

Wysocki, F. J., M. Leventhal, A. Passner, and C. M. Surko, Accumulation and storage of low energy positrons, *Hyperfine Interactions*, **44**, 185–200, 1988.

Zafar, N., J. Chevallier, F. M. Jacobsen, M. Charlton, and G. Laricchia, Experimentation with thin single crystal W foils as slow positron transmission mode moderators, *Applied Physics A*, **47**, 409–412, 1988.